

PERFORMANCE DEGRADATION OF PROTON-CONDUCTING
CERAMIC ELECTROLYZERS FOR HIGH-TEMPERATURE
WATER SPLITTING

by

Marcos Hernandez Rodriguez

A thesis submitted to the Faculty and the Board of Trustees of the Colorado School of Mines in partial fulfillment of the requirements for the degree of Master of Science (Mechanical Engineering).

Golden, Colorado

Date _____

Signed: _____

Marcos Hernandez Rodriguez

Signed: _____

Neal P. Sullivan
Thesis Advisor

Golden, Colorado

Date _____

Signed: _____

John Berger
Professor and Department Head
Department of Mechanical Engineering

ABSTRACT

The purpose of this thesis is to identify, quantify, and mitigate sources of degradation in proton-conducting ceramic electrochemical devices. The growing research in proton-conducting ceramics is allowing advances in electrochemical technology that are being harnessed to address societal challenges in electricity generation, energy storage, and fuel synthesis. Current electrochemical technology such as solid oxides have expensive material components and performance degradation issues, which is preventing the success of commercial kW-scale assemblies. The compatibility and stability of integration of novel perovskite materials with traditional-solid-oxide, chromium-based ferritic metals in operation of over 1000 hours is unclear. In addition, the operating conditions of proton-conductors are substantially different compared to oxygen-ion conductors, such as high-vapor content at the electrodes and an operating temperature that is less than that of solid oxide electrochemical devices. While operating at lower-temperatures should be beneficial, significant investigation of material stability is required for acceptable commercialization.

Due to the complexity of multiple factors that could cause degradation, this thesis focuses on symmetric-supported proton-conducting ceramic electrochemical devices. The two electrolyte materials are $\text{BaCe}_{0.7}\text{Zr}_{0.1}\text{Y}_{0.1}\text{Yb}_{0.1}\text{O}_{3-d}$ (BCZYYb7111) and $\text{BaCe}_{0.4}\text{Zr}_{0.4}\text{Y}_{0.1}\text{Yb}_{0.1}\text{O}_{3-d}$ (BCZYYb4411), and the steam electrode material is $\text{BaCo}_{0.4}\text{Fe}_{0.4}\text{Zr}_{0.1}\text{Y}_{0.1}\text{O}_{3-\delta}$ (BCFZY). The interconnect metals are Ce/Co coated Sandvik 441 and uncoated Sandvik 441. The environmental conditions are 10% steam + air (shop air or, 21% O_2 and 79% N_2) and dry oxygen. The operating conditions are 100 SCCM mass flow rate and 550°C. In order to collect accurate and repeatable measurements of degradation, a next-generation test stand with a ceramic coupon apparatus was built, validated, calibrated, and commissioned. Degradation rates

were captured and recorded through continuous and long-term Electrochemical Impedance Spectroscopy (EIS) measurements. Specifically, large volumes of EIS data is used to extract DC resistance and polarization resistance through a circle-tracing program written in RStudio, in order to determine area specific resistance (ASR), conductivities and degradation rates.

Results showed drastic degradation of BCFZY steam electrode at 50% steam + air and acceptable stability at 10% steam + air. Electrolyte perovskite material BCZYYb4411 shows slightly higher stability compared to BCZYYb7111 in 10% steam + air. Additionally, a dry oxygen-rich environment shows high stability of BCZYYb4411|BCFZY. Ce/Co coated, untreated Sandvik 441 interconnects show a lower degradation rate compared to uncoated, untreated Sandvik 441 interconnects; however, significant degradation rates are still present for both the electrode and electrolyte. EDX analysis on interconnects showed an insulation layer of hematite formation. In conclusion, proton-conducting perovskite materials and integration of traditional-solid-oxide, Cr-based ferritic metals degrade in high-water vapor environments. An increase of stability can be improved through a change of perovskite material ratio composition, and an oxygen-rich environment shows lower degradation rates.

TABLE OF CONTENTS

ABSTRACT.....	iii
LIST OF FIGURES AND TABLES.....	ix
LIST OF ABBREVIATIONS.....	xii
ACKNOWLEDGEMENTS.....	xiii
DEDICATION.....	xiv
CHAPTER 1 INTRODUCTION	1
1.1 General Introduction.....	1
1.2 Thesis Outline.....	2
CHAPTER 2 BACKGROUND	5
2.1 Working Principle of Fuel Cells.....	5
2.2 Background on Degradation in Solid Oxide Fuel Cells.....	8
2.3 Background on Proton-conducting Ceramic Fuel Cells.....	16
2.4 Motivation.....	19
2.5 Objective.....	21
CHAPTER 3 MATERIALS AND METHODS.....	22
3.1 Degradation Test Stand Physical Description.....	22
3.1.1 Symmetric Cell Architecture	22
3.1.2 Ceramic Coupon Assembly	23

3.1.3	Test Stand Design	24
3.2	YSZ LSM Symmetric Cell Experimental Information	26
3.2.1	Material Fabrication of YSZ LSM Symmetric Cells	26
3.2.2	Testing Setup	27
3.3	FuelCell Energy Proprietary Contact Paste Study Experimental Information	29
3.3.1	Material Fabrication.....	29
3.3.2	Testing Setup	29
3.4	BCZYYb BCFZY Symmetric Cell Experimental Information	30
3.4.1	Material Fabrication.....	31
3.4.2	Testing Setup	33
	3.4.2.1 Stability in Humidity.....	33
	3.4.2.2 Electrolyte Material Stability	34
	3.4.2.3 Stability in Oxygen	34
3.5	Interconnect Experimental Information	34
3.5.1	Material Preparation.....	34
3.5.2	Testing Setup	37
3.6	Testing Method	38
3.7	Method of Calculations.....	40
3.7.1	Sample Calculation	41

CHAPTER 4	RESULTS AND DISCUSSION	42
4.1	Validation of Degradation Test Stand with YSZ LSM Symmetric Cells	42
4.2	Performance Characterization of FuelCell Energy’s Proprietary Contact Paste at Intermediate Temperatures	47
4.3	Humidity Stability with BCZYYb7111: 10% Steam and 50% Steam	51
4.4	Electrolyte Stability: BCZYYb7111 and BCZYYb4411	52
4.5	Oxygen-rich Environment Performance on BCZYYb4411	56
4.6	Degradation From Interconnects: Uncoated Untreated and Ce/Co Coated Untreated Interconnects	56
4.7	Supplementary Results: NiOBCZYYb BCZYYb7111 Anode Degradation	59
4.7.1	NiBCZYYb BCZYYb7111 Anode Symmetric Cell Degradation in Ammonia Environment.....	60
4.7.2	NiBCZYYb BCZYYb7111 Anode Symmetric Cell Degradation and Recovering from H2 to NH3 to H2.....	61
CHAPTER 5	CONCLUSIONS AND FUTURE WORK	63
5.1	Validation of Degradation Test Stand with YSZ LSM Symmetric Cells	63
5.2	Performance Characterization of FuelCell Energy’s Proprietary Contact Paste at Intermediate Temperatures	64
5.3	Humidity Stability with BCZYYb7111: 10% Steam and 50% Steam	64
5.4	Electrolyte Stability: BCZYYb7111 and BCZYYb4411	64
5.5	BCZYYb4411 Performance in Pure Oxygen	65
5.6	Degradation from Interconnects	65

5.7	Future Work	65
	REFERENCES CITED.....	67
	APPENDIX SUPPLEMENTAL INFORMATION	82
A.1	RStudio Circle Tracing Program	82
A.2	CAD Drawings of Degradation Test Stand Ceramic Coupon Assembly	86

LIST OF FIGURES AND TABLES

FIGURE 2.1	Fuel cell operation (unpublished image courtesy to Professor Robert Kee), oxide-ion conducting fuel cell (left), proton-conducting fuel cell (right).....	7
FIGURE 2.2	Degradation of a fuel cell stack with different interconnects (courtesy of PhD candidate Long Le, accessed 08/19/2019, longlequoc1988@gmail.com).....	20
FIGURE 3.1	Degradation Test Stand and BCZYYb/BCFZY/BCZYYb cell architecture (image not to scale).....	23
FIGURE 3.2	Degradation Test Stand, on the left side is the setup without the quartz reactor, on the right is the ceramic coupon assembly held by the alumina rod, and a stationed thermocouple.....	24
FIGURE 3.3	Degradation Test Stand physical diagram	25
FIGURE 3.4	Symmetric cell layer structure for FCE proprietary contact paste experiments (not to scale), a) Pt contact paste, b) FCE contact paste	30
FIGURE 3.5	Cell fabrication process & experimental readiness.....	32
FIGURE 3.6	Interconnect structure, (a) top view, (b) side view	35
FIGURE 3.7	Pre-oxidized Ce/Co coated Sandvik 441 (unpublished image courtesy to Carolina Herradon Hernandez) a) interconnect X3,500 resolution, b) interconnect/scale interface composition.....	36
FIGURE 3.8	Cell with interconnect architecture (not to scale)	38
FIGURE 3.9	Extraction of fuel cell resistance values from Nyquist (EIS) plot	39
FIGURE 4.1	Repeatability validation of test stand through ASR, (a) DC ASR, (b) Polarization ASR.....	43
FIGURE 4.2	Accuracy validation of test stand through electrical conductivity properties (a) Resistivity, (b) Conductivity	45
FIGURE 4.3	YSZ/LSM supplementary validation experiments and effects of contact paste	46

FIGURE 4.4	Area specific resistance characterization of FCE proprietary contact paste with Pt contact paste	47
FIGURE 4.5	Characterization of FCE proprietary contact paste, (a) conductivity of BCZYYb7111, (b) Arrhenius plots of BCZYYb7111	49
FIGURE 4.6	Degradation of BCZYYb7111/BCFZY in different steam content	51
FIGURE 4.7	Comparison of BCZYYb7111 & BCZYYb4411 in 10% steam & air, (a) DC & polarization ASR, (b) Polarization ASR	53
FIGURE 4.8	Electrolyte performance in dry O ₂ and 10% steam & air, (a) DC & polarization ASR, (b) Polarization ASR.....	55
FIGURE 4.9	Performance comparison of Ce/Co coated and uncoated interconnect	57
FIGURE 4.10	EDX analysis of interconnect cross section (unpublished image courtesy to Carolina Herradon Hernandez)	58
FIGURE 4.11	NiBCZYYb BCZYYb7111 symmetric cell in 0.5NH ₃ + 0.5N ₂ gas environment at 550°C over 1000 hr.....	60
FIGURE 4.12	NiBCZYYb BCZYYb7111 symmetric cell in alternating fuel type between ammonia and hydrogen.....	61
FIGURE A.1	CAD drawing of DTS support component	81
FIGURE A.2	CAD drawing of DTS isolation ring component	82
FIGURE A.3	CAD drawing of DTS waffle component	83
FIGURE A.4	CAD drawing of DTS collar component	84
FIGURE A.5	CAD drawing of DTS small plunger component	85
FIGURE A.6	CAD drawing of DTS medium plunger component.....	86
FIGURE A.7	CAD drawing of DTS large plunger component	87

TABLE 2.1	Electrochemical device component material composition	9
TABLE 3.1	Chemical composition of Sandvik 441, given in wt. % [12].....	37
TABLE 4.1	Conductivity and resistivity values of YSZ, conductivity is in S/cm and resistivity is in (Ω cm)	44
TABLE 4.2	Conductivity values of BCZYYb7111 with Pt contact paste or FCE contact paste compared to literature values, conductivity is in S/cm (ln(S/cm)).....	50

LIST OF ABBREVIATIONS

Solid oxide fuel cell	SOFC
Solid oxide electrochemical cell	SOEC
Proton-conducting fuel cell.....	PCFC
Proton-conducting electrochemical cell.....	PCEC
Electrochemical impedance spectroscopy	EIS
Area specific resistance.....	ASR
Yttria Stabilized Zirconia.....	YSZ
$\text{BaCe}_{0.7}\text{Zr}_{0.1}\text{Y}_{0.1}\text{Yb}_{0.1}\text{O}_{3-\delta}$	BCZYYb7111
$\text{BaCe}_{0.4}\text{Zr}_{0.4}\text{Y}_{0.1}\text{Yb}_{0.1}\text{O}_{3-\delta}$	BCZYYb441
$\text{BaCo}_{0.4}\text{Fe}_{0.4}\text{Zr}_{0.1}\text{Y}_{0.1}\text{O}_{3-\delta}$	BCFZY
$(\text{La}_{0.85}\text{Sr}_{0.15})_{0.98}\text{Mn Oxide}$	LSM
DC resistance	R_{DC}
Polarization resistance	R_P
Degradation Test Stand.....	DTS
Standard cubic centimeter per minute.....	SCCM
Standard-state liter per minute	SLM

ACKNOWLEDGEMENTS

First and foremost, I would like to thank my advisor Professor Neal P. Sullivan for his mentorship, patience, and wisdom throughout my journey in my undergraduate and graduate years. I extend my thanks to the rest of my committee: Professor Sandrine Ricote and Professor Gregory Jackson for their comments, suggestions, and knowledge. I would like to thank Professor Robert Kee for his thoughts and insight.

Funding for this research was provided by the U.S. Department of Energy, Office of Energy Efficiency and Renewable Energy (EERE), through the “Proton-conducting ceramic electrolyzes for high-temperature water splitting” Award #DE-EE008376. Additionally, I would like to show my gratitude to Jahi Simbai and Andrea Salazar Morgan for providing funding in the early years and for constant, encouraging support.

My journey would have been a lot more difficult if it weren't for my Colorado Fuel Cell Center research colleges: Long Le, Zehua Pan, Liangzhu Zhu, Duc Nguyen, Max Pisciotta, and Carolina Herradon Hernandez. Thank you to my colleges for your research support, comradery, and insight. I would like to further thank Carolina Herradon Hernandez for her research support in microscopy analysis.

The beginning of my journey was only possible through the emotional and mental support from my family and friends. Special thanks to my friend Alber R. Lima Flores for his encouragement, enthusiasm, and advice. A huge thanks to Andrea Golden-Lasher for her love and immense support as my best friend and partner. My deepest gratitude goes to my parents and siblings, Enrique, Alonso, and Perla, for their unconditional love, support, and patience throughout all my years. Thank you everyone for one more milestone, and yet more to come.

For my parents, Ernesto Hernandez Luna and Carmen Rodriguez Vega,
who nurtured, inspired, and embolden me to reach for my dreams and beyond.

CHAPTER 1

INTRODUCTION

The purpose of this thesis is to research degradation of new materials in proton-conducting ceramics and in different operating conditions. The studies presented in this thesis investigate the performance degradation of symmetric electrolyte-supported proton-conducting ceramic electrochemical devices. A unique apparatus was built, validated, calibrated, and operated, to execute repeatable and accurate measurements on continuous long-term experiments.

This chapter provides an introduction to fuel cell technology and proton-conducting ceramic fuel cells, followed by an outline of this thesis.

1.1 General Introduction

Solid oxide fuel cell (SOFC) technology offers advantages over traditional combustion technology, such as,

- high electrical efficiency
- environmentally friendly
- scalability
- high fuel flexibility, including hydrocarbons, alcohols, and ammonia
- reversible operation for mid-to-long term energy storage
- heat generators [1-10]

SOFC's have demonstrated successful and stable performance at high temperatures (800-1000°C) [11]. An issue for SOFC commercialization is the high cost of component materials, such as the cell packaging component—the electronically conductive ceramic interconnects. With improvement in material development and production methods, a reduction of operating

temperatures has allowed a decrease in the necessity of material robustness and the integration of less expensive components and manufacturing methods [1,2,6,7,11,12].

Introduced in the early 1980s by Iwahara et al. [13], recent proton-conducting ceramic electrochemical devices have attracted much attention in research. Due to advances in proton-conducting ceramic materials, proton-conducting ceramic fuel cells (PCFC) and proton-conducting ceramic electrochemical cells (PCEC) have the potential to accelerate commercialization of fuel cell technology, as opposed to traditional solid oxide fuel cells. PCFCs and PCECs have a higher degree of reduction in operating temperatures in the range of 400-600°C, in comparison to 600-1000°C for SOFCs[4]. This technology could offer environmental-friendly energy and a continuous source of electrical power, so long as fuel and oxidant gas is provided. Sectors that can benefit from this technology are in stationary power generation, portable power generation, and power for transportation [14].

1.2 Thesis Outline

This thesis consists of five chapters:

- Chapter 1: Introduction
- Chapter 2: Background
- Chapter 3: Materials and Methods
- Chapter 4: Results and Discussion
- Chapter 5: Conclusions and Future Works

Chapter 2 provides background on the PCFC and fuel cell technology and the motivation for this investigation. This chapter introduces each fuel cell component, the chemical functionality of the cell, the importance of interconnect material, and the motivation and objective of these studies.

Chapter 3 describes the operation and architecture of the test stand used for cell experimentation. Experimental procedures and setup descriptions are described in this chapter, followed by the calculation and data analysis of each measurement. Chapter 4 provides results and discussion of the following studies:

- Validation of the Degradation Test Stand (DTS): the DTS is validated for accuracy and repeatability due to the unique method of investigating performance of electrochemical devices used with this apparatus.
- Performance Characterization of FuelCell Energy's Contact Paste at Intermediate Temperatures: for this study, FuelCell Energy (FCE) requested characterization of their proprietary contact paste at PCFC operating temperatures by using the Degradation Test Stand. A supplementary experiment of the effects of contact paste on area specific resistance (ASR) values is investigated, as well as further DTS validation experiments.
- Humidity stability: humidity is known to cause corrosion of steam electrodes made of oxide-ion conducting materials. Therefore, investigation is required to determine if humidity corrosion appears on steam electrodes composed of proton-conducting materials. Device performance at high and low steam levels is tested to understand the effects of humidity.
- Electrolyte material stability: performance results of proton-conducting devices using electrolyte material $\text{BaCe}_{0.4}\text{Zr}_{0.4}\text{Y}_{0.1}\text{Yb}_{0.1}\text{O}_{3-\delta}$ (BCZYYb4411) show higher stability than $\text{BaCe}_{0.7}\text{Zr}_{0.1}\text{Y}_{0.1}\text{Yb}_{0.1}\text{O}_{3-\delta}$ (BCZYYb7111). This study seeks to confirm and compare the performance of these two electrolyte materials at a stable gas environment.
- Oxygen-rich gas environment stability: Operation under pure O_2 was believed to accelerate degradation of a SOFC or PCFC stack due to corrosion/oxidation. However,

experiments have shown that operation under pure O₂ of a cell stack contributes to lower degradation as opposed to the use of humidified air. This study focuses on the effects of a pure oxygen gas environment on the PCFC steam electrode.

- Interconnect degradation: ferritic interconnect components are known to degrade electrochemical devices through Cr poisoning, although coated interconnects have been shown to help reduce Cr vaporization at traditional SOFC operating conditions. These ferritic interconnect materials, namely uncoated untreated Sandvik 441 and Ce/Co coated untreated Sandvik 441, are integrated with proton-conducting materials to test the performance degradation of electrochemical devices that operate at PCFC conditions.

Chapter 5 finalizes this thesis with conclusions of each study and future work.

CHAPTER 2

BACKGROUND

The study presented in this thesis investigates the performance degradation of proton-conducting ceramic electrochemical devices. Compared to oxygen-ion conductors, there has been limited research done in the area of proton-conducting ceramics due to the discovery of new materials and fabrication processes [3]. This chapter contains background information on the working principle of fuel cells, background on degradation of solid oxide fuel cells, and background on degradation of proton-conducting ceramic fuel cells, followed by the motivation and objective for these studies.

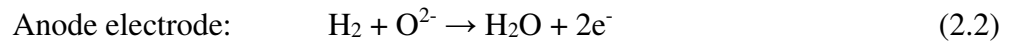
2.1 Working Principle of Fuel Cells

Fuel cells are devices that directly convert chemical energy to electrical energy and heat. Oxidant and fuel gas pass through the electrodes where half-cell reactions occur; these reactions cause the transport of active charge carrier species through the cell, while electrons are released into an external circuit [14]. There are several types of fuel cells which are characterized by the functionality of the electrolyte material: polymer electrolyte membrane, molten carbonate fuel cell, solid acid fuel cell, phosphoric acid fuel cell, alkaline fuel cell, solid oxide fuel cell, and proton conducting fuel cell [14].

For SOFCs, fluorite materials are used for the electrolyte material, while for PCFCs, perovskite materials are used. Perovskites have an ABO_3 ideal structure, where on a face centered cubic lattice the A-site atoms are located at the corners, while the O atoms are located in the faces, and the B-site atom is positioned in the center.

Solid oxide fuel cells and proton-conducting fuel cells are similar in structure but convert chemical energy to electrical energy differently due to different materials. Figure 2.1 illustrates the functionality of both types of fuel cells: on the left is an oxide-ion conducting fuel cell and on the right is a proton-conducting fuel cell. As depicted, both fuel cells have an electrolyte, a cathode electrode, an anode electrode, an air channel, a fuel channel, and interconnects.

Solid oxide fuel cells are defined as having a dense ceramic electrolyte that transports oxygen ions. On the left of Figure 2.1, a SOFC is exposed to methane (CH₄) as the fuel and air as the oxidant. The fuel is fed into the anode channel where methane undergoes internal reforming, producing hydrogen (H₂), carbon monoxide (CO), and carbon dioxide (CO₂). The hydrogen then undergoes oxidation from the anode electrode (eq. 2.1) [15].



At the same time, electrons are released and collected at the anode interconnect, which are then circuited to the cathode side. This flow of electrons produces a direct current (DC). Air flows on the surface of the cathode, where oxygen (O₂) undergoes reduction from the available electrons (eq. 2.2). The porous cathode material permits diffusion of oxygen species, which are then reduced to oxygen ions (O²⁻) and transported through the electrolyte into the anode, where reaction occurs with the fuel. This process leads to water vapor production at the anode side.

In an ideal proton-conducting fuel cell, the electrolyte material only permits the transport of protons (H⁺) [8]. The right side of Figure 2.1 illustrates the functionality of a PCFC operating on methane as the fuel and air as the oxidant. Similar to SOFC, fuel is fed into the anode channel

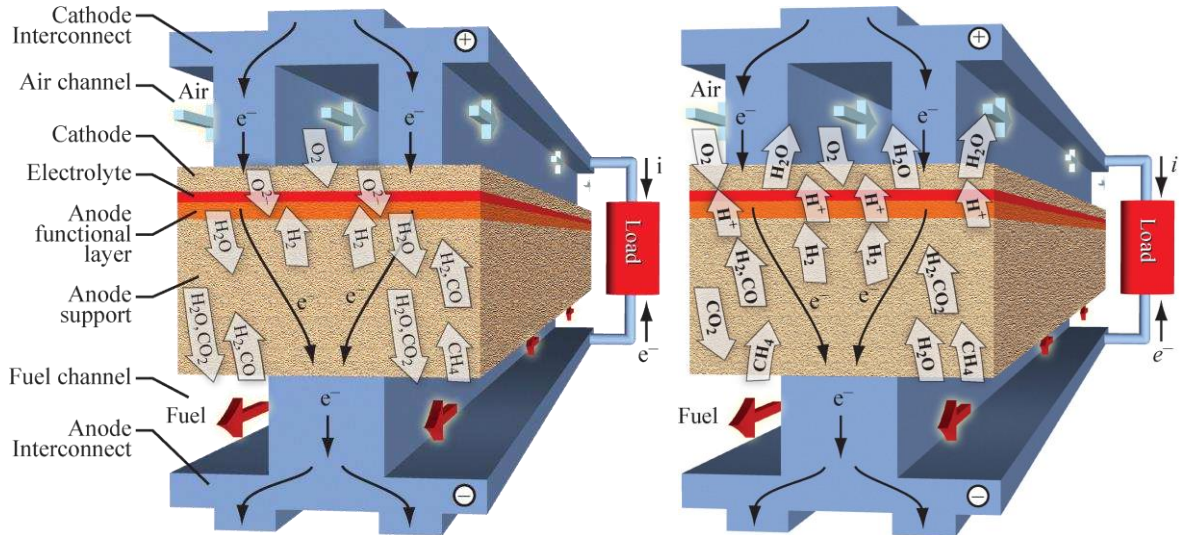
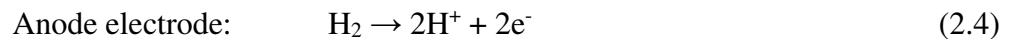
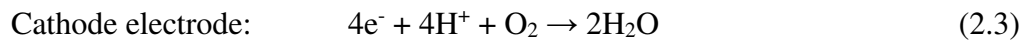


Figure 2.1: Fuel cell operation (unpublished image courtesy to Professor Robert Kee), oxide-ion conducting fuel cell (left), proton-conducting fuel cell (right).

where methane undergoes internal reforming. The hydrogen (H_2) then undergoes an oxidation reaction (eq. 2.4).



Through this reaction, electrons are generated and collected by the anode interconnect, where they are circuited to the cathode side. This flow of electrons produces a direct current (DC). At the same time, this reaction produces protons that permeate through the electrolyte to react with oxygen molecules at the cathode side (eq. 2.3). This reaction leads to the formation of water vapor at the cathode side. The benefit of water production at the cathode side is that fuel dilution is avoided since fuel at the anode side remains pure [14].

Interconnects are essential fuel cell components that help seal each electrode environment from gas leakage and provide stack support and electrical conductivity. Through SOFC research, expensive ceramic interconnects have been replaced with ferritic stainless steel interconnects.

Lower operating temperatures of PCFCs allow for the use of new and inexpensive materials.

Such interconnect materials must provide:

- high conductivity
- mechanical strength
- thermal expansion properties that match that of the cell
- impermeability and chemical stability

As mentioned previously, each interconnect is exposed to different gas environments. The materials used in this thesis are listed in Table 2.1. The electrolyte and electrode materials are high proton-conducting ceramics that are meant to operate at intermediate temperatures. The ferritic Ce/Co coated interconnect material is traditionally designed for high temperature SOFC operation, but its compatibility with PCFC materials and operating conditions will be investigated. Due to intermediate temperature operation, ferritic uncoated interconnect material will be studied for compatibility in order to determine if a coating layer can be avoided to reduce material cost. The electrolyte and electrode materials were made on-site, while the interconnect materials were provided by industrial supplier, Sandvik.

2.2 Background on Degradation in Solid Oxide Fuel Cells

Despite the advantages and promises of fuel cell technology, material and fabrication procedure costs, stacking capabilities and performance degradation are major issues impeding widespread application. Some of these issues have improved through SOFC research and development, but with PCFC advances these complications can be further reduced. Currently, solid-oxide materials and operating conditions have been adapted for use with proton-conducting ceramics. For example, ferritic interconnects for proton-conducting ceramics are the same

material suited for solid-oxide operating conditions: ferritic stainless steel alloys with various coatings [1, 3, 4, 11]. These similarities demand investigation of degradation factors seen in SOFC performance research, but with proton-conducting ceramic materials.

SOFC research has shown that performance degradation can come from cathode poisoning and corrosion, such as CO₂ corrosion, humidity corrosion, Cr poisoning, and Si poisoning. For example, Cr poisoning has been shown to attack the steam electrode through Cr vaporization from ferritic interconnects on oxide-ion conductors; these same metal interconnects are used with proton-conducting materials. Since the steam electrode is exposed to different water vapor contents for electrolysis mode, the proton-conducting electrode and electrolyte materials can face similar humidity corrosion as seen in SOFC materials. The anode electrode degrades from

Table 2.1: Electrochemical device component material composition

Component	Material Composition
Electrolyte	BaCe _{0.7} Zr _{0.1} Y _{0.1} Yb _{0.1} O _{3-δ} (BCZYYb7111)
Electrolyte	BaCe _{0.4} Zr _{0.4} Y _{0.1} Yb _{0.1} O _{3-δ} (BCZYYb4411)
Cathode (Steam) Electrode	BaCo _{0.4} Fe _{0.4} Zr _{0.1} Y _{0.1} O _{3-δ} (BCFZY)
Interconnect	Uncoated, Untreated Sandvik 441 ferritic steel
Interconnect	Ce/Co Coated, Untreated Sandvik 441 ferritic steel

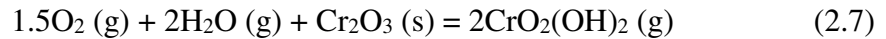
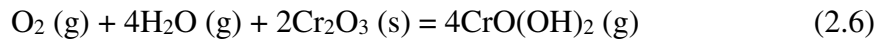
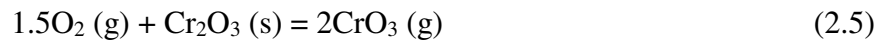
similar poisoning and corrosion mechanisms, such as Ni coarsening, carbon poisoning (Coking), and sulfur poisoning.

Commonly used materials, such as lanthanum, strontium, and barium, in the A-site of ABO_3 -type perovskite structure for cathodes in SOFC have been shown to be affected by CO_2 corrosion. Barium-based cathode materials have received more attention than La and Sr due to high performance at low and intermediate temperatures [16-20]. CO_2 has been found to be easily absorbed on the surface of the electrode and to lead to the formation of barium carbonate ($BaCO_3$) under low-intermediate operating temperatures [5]. Oxygen active sites are occupied by CO_2 , leading to reduction of oxygen reactions. Surface contamination was detected through both an increase in DC resistance and polarization resistance via electrochemical impedance spectroscopy (EIS) [21]. The introduction of Fe or Nb in the B-site in the material can lead to CO_2 corrosion resistance [22-25]. However, CO_2 corrosion degradation can be reversible at some temperatures and duration of exposure [5].

Barium-based perovskite material for the steam electrode on proton-conducting devices is introduced to water vapor generation, which may lead to humidity corrosion. Ba-based cathode materials, specifically, $Ba_{0.9}Co_{0.7}Fe_{0.2}Nb_{0.1}O_{3-\delta}$ (BCFN) has been researched at a temperature range of 650-800°C at different humidity levels: 0%, 1%, 3%, 5%, and 10% [26]. This study showed decreasing electrical conductivity with increasing humidity levels as well as a decrease in polarization resistance with increasing temperatures regardless of water vapor content. EIS results demonstrated performance recovery from humidity corrosion of BCFN electrode. In SOFC operation, Ba-based cathode materials show the possibility of resisting humidity corrosion to an extent, while reversibility of degradation can be achieved at specific temperatures and duration of exposure [5]. An improved electrode|electrolyte interface allows for cell durability

from a humid environment; for example, BCFN|BZCY ($\text{BaZr}_{0.1}\text{Ce}_{0.7}\text{Y}_{0.2}\text{O}_{3-d}$) interface showed oxygen ion transfer enhancement from humidity [27].

A reduction of temperature in SOFC technology has allowed the use of low cost metallic interconnects. However, due to harsh operating gas environments and conditions, ferritic interconnects are prone to oxidation and corrosion. This can lead to increasing DC resistance from oxidation layer on the surface of the metal. In order to overcome the oxidation on the interconnect surface at SOFC high temperatures, Cr containing alloys are favored due to their corrosion resistance. However, under common SOFC operation, Cr^{6+} vaporization leads to cell degradation from electrode poisoning [28]. Some Cr species formations are, [29]



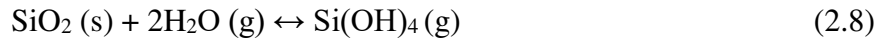
Cr poisoning of BCFN ($\text{Ba}_{1-x}\text{Co}_{1-y}\text{Fe}_y\text{Nb}_{0.1}\text{O}_{3-\delta}$) and BCFN-1%GDC ($\text{Ce}_{0.9}\text{Gd}_{0.1}\text{O}_{2-\delta}$) cathodes have been evaluated at 800°C and 650°C, and 800°C, respectively [5]. Polarization resistance results show that BCFN is able to maintain its oxidation reduction property to an extent, while the addition of GDC provides Cr poisoning tolerance. Through electrochemical reaction models, Cr species deposited on the electrode|electrolyte interface leads to cell performance degradation [30]. Cr poisoning from Cr containing metallic interconnects could lead to PCFC cell degradation, as seen in SOFCs.

As previously mentioned, Cr poisoning from ferritic steel under operating conditions of the cathode SOFC prohibits long-term life of the cell. In order to mitigate Cr vaporization, investigation of various metal alloys, and perovskite or spinel structure protective coating has

been done. Many methods used to coat the metal are physical vapor deposition, thermal spraying and dip coating [59, 60]. Quantification of Cr vaporization is used to determine the effectiveness of the metal and/or coating from poisoning the cell. The standard approach to quantify Cr vaporization in large concentrations of other gases is by the transpiration method. However, this method has posed technical challenges that call for other collection|analysis techniques. Such techniques/analysis are mass loss/mass balance, thermogravimetric analysis with mass spectroscopy (TGA-MS)|TGA-MS, Condensation|inductively coupled plasma-mass spectrometry (ICP-MS), condensation|inductively coupled plasma-atomic emission spectrometry (ICP-AES), quartz wool|ICP-MS, ceramic plate|energy dispersive x-ray spectroscopy (EDS), wafer collector|Rutherford backscattering spectroscopy (RBS), denuder|photospectroscopy, and ionic conductivity method (ICM)|conductivity probe [11]. Through these collection and analysis techniques, several alloy metals and metal coatings have been reported.

Interconnect materials that are of interest and that have been reported are Sanergy HT, Sanergy HT/Co (640nm), and 441 SS. It is shown that Sanergy HT at 850°C, 750°C, and 650°C in air + 3% steam has a vaporization rate of 21-6 ($10^{-10} \text{ kg m}^{-2} \text{ s}^{-1}$), 7-5 ($10^{-10} \text{ kg m}^{-2} \text{ s}^{-1}$), and 3 ($10^{-10} \text{ kg m}^{-2} \text{ s}^{-1}$), respectively [61]. Sanergy HT/Co at 850°C in air + 3% steam has a vaporization rate of 1 ($10^{-10} \text{ kg m}^{-2} \text{ s}^{-1}$) [62], while 441 SS at 850°C in air + 3% steam and 800°C in air to 6.9% steam has a vaporization rate of 8 ($10^{-10} \text{ kg m}^{-2} \text{ s}^{-1}$) and 2.5 ($10^{-10} \text{ kg m}^{-2} \text{ s}^{-1}$), respectively [63, 64]. While these investigations show Cr vaporization rates that can poison the cathode electrode, none have been quantified at PCFC operating temperatures. On a broader scope, this provokes investigation of Cr poisoning degradation effects at PCFC operating conditions that is caused by Cr vaporization.

The introduction of Si through glass-based sealing material and during preparation of SOFCs can lead to performance degradation from electrolyte Si poisoning. It has been shown that Si segregates at the electrolyte material grain boundaries, forming an insulated phase which decreases the oxide-ion conductivity of the cell [5]. Research has shown Si poisoning on Sr-based perovskite materials at SOFC operating temperatures [31-33]. A thin glass film has been observed on LSM|YSZ cathode when exposed to silicate at 750°C [34]. The surface exchange coefficient of LSCF has been shown to decrease at increasing humidity levels at 600°C [35-37]. However, other studies have shown that the incorporation of Si in the cathode perovskite material can lead to cathode conductivity and stability from CO₂ [38, 39]. The addition of Si in the cathode material has been studied on La_{0.6}Sr_{0.4}Co_{0.78}Fe_{0.195}Si_{0.025}O_{3-δ} and Sr_{0.5}Ca_{0.5}Fe_{0.85}Si_{0.15}O_{3-δ}, both of which have shown enhancement in cathode performance. Si poisoning has a similar reaction process as Cr poisoning. Experimental results indicate that humidity is the main cause of Si performance degradation, specifically,



LSCF cathode had no Si mitigation in dry air at 600°C for 1000 hours test [5]. Therefore, dried air is recommended to avoid Si poisoning of oxide-ion conductors, however, this can't be done for proton conductors since there is steam formation on the cathode electrode.

The most common anode metal used for SOFC is Ni, which is paired with electrolyte material to provide a similar expansion coefficient as the electrolyte component and to prevent Ni agglomeration. Additionally, Ni-based cermet (cermets are materials made of ceramic and sintered metal) anodes are preferred for their high electrical conductivity and high activity for the electrocatalytic oxidation of hydrogen [40, 41]. With nickel-yttria stabilized zirconia (Ni-YSZ)

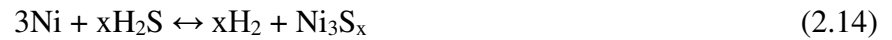
anodes, Ni coarsening has been observed. The mechanism of this phenomenon causes Ni agglomeration and lack of Ni-Ni contact [42-45]. The increase in Ni particle size results in an increase of polarization resistance [42]. Iwata [43] showed a decrease in specific surface area of Ni substrate from 1.285 m²/g to 0.613 m²/g due to Ni sintering while running in air and a gas mixture of 50% H₂ + 50% N₂ at a temperature of ~1000°C and at a load current density of 0.3 A/cm² for 1015 hours. Additionally, this same experiment revealed a Ni-YSZ anode degradation of 14 μV/h determined through impedance analysis, and an increase of Ni particle diameter from 0.1 μm to 10μm using scanning electron microscopy-electron probe microanalysis. This anode degradation mechanism can occur through diffusion/sintering of Ni particles, vacancies, and grain boundaries [42].

In humid atmospheres, performance degradation from Ni coarsening is more severe. This phenomenon is caused by Ni(OH)₂ formation, which is known to evaporate and transport Ni particles, resulting in loss of Ni from the anode and Ni grain growth. As little as 1-2% steam in fuel at 900-1000°C is sufficient to form hydroxide, which leads to Ni(OH)₂ formation [46, 47]. Ni(OH)₂ condenses in the form of Ni in low humidity regions. This evaporation mechanism transports Ni particles and agglomerates them to form large grains. Ni-YSZ anode in humid environments has shown performance deterioration and an increase in both DC and polarization resistance. Through electrode microstructure observation of Ni-YSZ operated at 1000°C in 40% steam + 60% H₂ fuel and at 300 mA/cm² and within 48 hours, Matsui et al. [48] demonstrated a reduction of Ni volume fraction from 25.3% to 23.6%, as well as an increase of average Ni grain size from 1.38μm to 1.75μm. This change in homogeneity in the anode microstructure leads to a decrease in electrical conductivity and cell performance.

The presence of H₂S in fuel mixtures can lead to cell performance deterioration through sulfur poisoning [42]. Studies on Ni-YSZ anode have shown detrimental effects from O²⁻ ion blockage and from sulfur particles settling on active sites, which leads to an increase in polarization resistance [49-53]. Li et al. [49] showed an increase of polarization resistance of Ni-YSZ anode within 30 minutes of 0.2% H₂S exposure through injection, under operating conditions of 0.50 A/cm² at 800°C in 0.5SLM H₂ fuel. The mechanisms of this phenomenon are caused from the following reactions [51, 54],



Additionally, the formation of Ni₃S₂ reduces the Ni content on the anode, and is known to cause permanent damage to the cell [49-52]. These sulfidation behaviors are formed according to the following reactions [51, 56],



The formation of nickel sulfides has shown high H₂S concentrations of <100ppm. Cheng et al. [57] showed that Ni-YSZ anode upon exposure to a fuel containing 100ppm of H₂S at a testing temperature ranging from 500-800°C, underwent significant sulfidation. This effect was only witnessed through in situ Raman microspectroscopy at an experimental cool-down of ~2-

5°C/min. Sulfur poisoning can lead to reduction in performance, irreversible damage to the cell, and delamination of the anode [42].

Carbon formation or coking on porous material such as Ni-YSZ can lead to catalyst deactivation, physical cell damage, and reduction in cell performance. Carbon formation and deposition can occur in different ways. For example, carbon particles can be chemisorbed or physically absorbed which can block the flow of fuel, and they can surround material particles and ultimately, deactivate them (metal dusting). Carbon particles can also build filaments that induce stress on the cell, which leads to material cracking [42]. Lanzini et al. [58] showed the formation of whisker-type carbon filaments in Ni-YSZ anode at 800°C in CH₄:CO₂ 1:1 volume mixture over a period of 250 hours. Electrochemical impedance spectra of this study showed a steady decline in cell voltage and an increase in DC resistance and polarization resistance, ~0.2 Ω cm² and ~1.6 Ω cm², respectively. Coking caused through the use of carbonaceous fuels can be responsible for performance loss through deactivation and passivation mechanism, and cell cracking.

2.3 Background on Proton-conducting Ceramic Fuel Cells

Fuel cell high operating temperatures have shown to lead to poor long-term cell stability, interlayer diffusion, and fabrication and material problems [65, 66]. Therefore, lower operating temperatures are favored in improving cell reliability, enabling a wider choice of materials, and creating possibilities for use of unexploited heat sources from industry for providing electrochemical heat energy. For these reason, proton-conducting ceramics are quite promising for fuel cell applications as opposed to oxygen-ion conductors. Proton conductors have a higher

ionic conductivity at intermediate temperatures, have shown good chemical compatibility with the most used hydrogen electrode, Ni, and sufficient current efficiency [13, 67-69].

Proton conducting ceramics provide advantages to oxygen-ion electrolytes in electrolysis systems. Since proton-conducting electrolytes only allow protons to pass and prohibit transport of oxide ions and gas molecules, pure and dry hydrogen is produced at the hydrogen electrode side [70]. This prevents the need of gas separation. Oxidation of Ni electrode in oxygen-ion electrochemical devices, which is known to cause performance degradation of the cell, is avoided through proton conductors in that the Ni electrode is solely exposed to hydrogen, as opposed to the traditional steam content environment [71-73]. Reversible fuel cell technology is realistically feasible through proton-conducting materials. Such a device is able to produce electricity upon applying potentials lower than the cell open circuit potential (fuel cell mode), and to store electricity in the form of chemical energy upon applying potentials higher than the cell open circuit potential (electrolysis mode) [74]. Electrochemical modeling studies show that a hydrogen electrode supported cell configuration is optimum for both mode systems in proton conductors for achieving high energy conversion efficiency [70].

Previous materials used for PCECs and PCFCs have demonstrated low Faradaic efficiency (FE) and low electrode performance in electrolysis mode. Commonly used proton-conducting perovskite electrolyte materials are yttrium-doped barium zirconates (BZY), barium cerates (BCY), and $\text{BaCe}_{1-x}\text{Zr}_x\text{Y}_y\text{O}_{3-\delta}$ (BCZY). Research has shown that barium cerates are favored based on their high ionic conductivity but are unstable in high CO_2 atmospheres. A solution to the sensitivity of a CO_2 environment is doping with Nd^{3+} or Gd^{3+} , or the substitution of Ce^{4+} by Zr^{4+} [75]. The B-site atom of BCY is replaced with Zr^{4+} , forming yttrium-doped barium zirconates which has a higher CO_2 corrosion tolerance, but lower conductivity. In order to

compensate for instability from CO₂ and low conductivity, both Ce and Zr are included in the electrolyte material, forming BCZY [75]. However, none of these are pure proton conductors, but rather mixed ionic-electronic conductors, which causes low Faradaic efficiency values [8].

Dailly et al. showed degradation rates in electrolysis mode and in fuel cell mode during reversible cycles between each mode. Their cells had BaCe_{0.8}Zr_{0.1}Y_{0.1}O_{3-δ} (BCZY811) as electrolyte, NiO|BCZY811 as hydrogen electrode, BCZY811|BSCF (Ba_{0.5}Sr_{0.5}Co_{0.8}Fe_{0.2}O_{3-δ}) as composite air electrode, and BSCF as air current collector [76]. This experiment yield ~165 mW cm⁻² at 600°C in fuel cell mode and 170 mA cm⁻² at 600°C in electrolysis mode with a potential E=0.7 V. Testing this cell in reversible cycles between each mode over 800 hours revealed performance degradation. An overall degradation rate of 5%/khr was determined in electrolysis mode, and 8%/khr degradation in fuel cell mode [76].

Duan et al. has demonstrated higher Faradaic efficiency values for pure ion-conducting electrolyte material BaCe_{0.7}Zr_{0.1}Y_{0.1}Yb_{0.1}O_{3-δ} (BCZYYb7111) as opposed to BaZr_{0.8}Y_{0.2}O_{3-δ} (BZY20) in both fuel cell mode and electrolysis mode [8]. The cathode used for both cells was BaCo_{0.4}Fe_{0.4}Zr_{0.1}Y_{0.1}O_{3-δ} (BCFZY), which was developed for oxidation reduction reaction in PCFC cathode. The anode used was 40 wt% BaCe_{0.7}Zr_{0.1}Y_{0.1}Yb_{0.1}O_{3-δ}+60wt% NiO+20wt% starch. BCFZY|BCZYYb cells have shown high energy conversion efficiency from conversion of both H₂O and CO₂ [8]. Also, the formation of higher carbon species is favored due to lower operating temperatures (300-600°C), such as methane and syngas. It is worth mentioning that Ni-BCZYYb anode material has shown excellent catalytic activity, high electrical conductivity, and acceptable compatibility with electrolyte material, while having a high sulfur and coking tolerance due to their high water uptake property [40]. Through electrochemical impedance spectroscopy the stability of BCFZY|BCZYYb cells from cycling between fuel cell mode and

electrolysis mode demonstrated no significant signs of degradation, thereby confirming the feasibility of reversibility for these fuel cell protonic materials. However, electrochemical impedance spectroscopy measurements revealed degradation of BCFZY|BCZYYb cells in electrolysis mode: 13% increase in polarization resistance at 600°C and 20% steam after 550 hours; and 18% increase in polarization resistance at 550°C and 10% steam after 955 hours [8].

Figure 2.2 illustrates the performance degradation of the latest unit-cell stacks (courtesy of PhD candidate Long Le). The experiments are executed for 1000 hours and voltage is measured continuously; voltage is in the y-axis and time is on the x-axis. Each experiment was executed at 100mA/cm² at 550°C with 10% steam + hydrogen fuel on the anode channel and dry air on the cathode channel. Two different types of electrolyte material were investigated, each with different Sandvik interconnect materials. BaCe_{0.2}Zr_{0.6}Y_{0.2}O_{3-δ} (BCZY26) cell with uncoated, untreated interconnect has a drastic degradation rate of 65%/khrs, while BCZYYb4411 cell with Ce/Co coated, pre-oxidized interconnect has a degradation rate of 3.5%/khrs. While the application of different interconnect materials and electrolyte materials can increase long-term stability and decrease degradation factors, the lifetime of the cell needs further improvement for commercial adoption.

2.4 Motivation

PCFCs/PCECs operate at different environments compared to SOFC/SOEC; therefore, cell components for proton-conducting ceramics may have different performance degradation mechanisms and rates compared to well-researched solid-oxides. Specifically, interconnects are exposed to different environments at either side of the cell. The benefits of proton-conducting ceramics over oxide-ion conducting materials is the higher ionic conductivity at lower temperatures, which has the potential for higher performance with less expensive interconnects

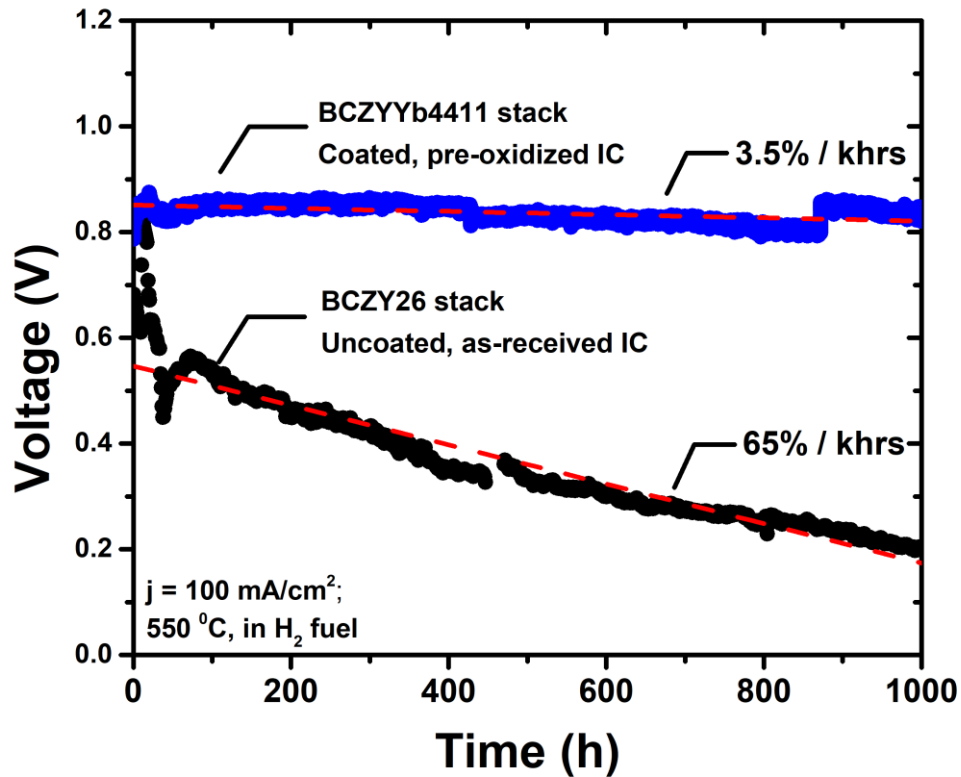


Figure 2.2: Degradation of a fuel cell stack with different interconnects (courtesy of PhD candidate Long Le, accessed 08/19/2019, longlequoc1988@gmail.com)

and balance-of-plant materials; and formation of water on the steam electrode. Additionally, proton-conducting ceramics have a higher methane conversion, higher carbon coking, and sulfur-poisoning resistance, while having the capability of operating as electrolyzers [3, 4, 8]. There is limited study in performance degradation of isolated or simplified cell components at different humidity levels, oxygen-rich environments, solely interconnect reactions, and direct and/or indirect contamination from interconnects onto cell components at these gas environments. Due to new operating temperatures, altered gas environments, and integration of fuel cell component materials, in comparison to solid-oxides, it is important to understand the behavior of traditional solid-oxide materials in integration with proton-conducting ceramics.

2.5 Objective

High degradation rates remain an issue for PCFCs/PCECs in demonstrating stable performance. Degradation behavior from PCFC/PCEC may be similar to those for SOFC/SOEC: humidity corrosion, different gas environment corrosion or poisoning, and ferritic interconnect chromium poisoning [1, 2, 4-7, 11, 12]. Due to the complexity of degradation factors, continuous measurements of performance degradation would have to be accurate and repeatable. For this reason we have designed, built, and commissioned three unique test stands for reliable electrochemical impedance measurements over 1000 hours of continuous experimentation.

In order to reduce the complexity and target the root cause of degradation at the steam electrode, this study focuses on a steam electrode, electrolyte supported symmetric cell. A summary of the component material compositions are provided in Table 1.1 (pg. 9). The steam electrode material for all evaluated experiments is $\text{BaCo}_{0.4}\text{Fe}_{0.4}\text{Zr}_{0.1}\text{Y}_{0.1}\text{O}_{3-\delta}$ (BCFZY). Humidity stability is evaluated at 10% and 50% steam partial pressures on symmetric cells. An investigation of the stability of electrolyte material ($\text{BaCe}_{0.7}\text{Zr}_{0.1}\text{Y}_{0.1}\text{Yb}_{0.1}\text{O}_{3-d}$ [BCZYYb7111] and $\text{BaCe}_{0.4}\text{Zr}_{0.4}\text{Y}_{0.1}\text{Yb}_{0.1}\text{O}_{3-d}$ [BCZYYb4411]) at stabilized humidity level is executed. The stability of oxygen-rich, no steam environment with stable electrolyte material is executed. Additionally, degradation effects of interconnects on the cell are executed by including the metal at stable environmental condition on the symmetric cell. By integrating interconnects on the symmetric cell, effects like Cr vaporization poisoning on the electrolyte, electrode, interconnect, and electrolyte-electrode interface are measurable through electrochemical impedance spectroscopy.

CHAPTER 3

MATERIALS AND METHODS

The first sections of this chapter introduce and describe the operation and architecture of the Degradation Test Stand and the coupon ceramic assembly in which the symmetric cells are mounted. The experimental procedure and preparation for each test is provided in detail, followed by the calculation and data analysis of each measurement.

3.1 Degradation Test Stand Physical Description

The challenges with the degradation test stand are as follows:

- Isolation of electrochemical device from apparatus contamination
- Accurately measure changes in electrochemical impedance over hundreds of hours
- Assembly must provide a repeatable setup
- Isolation from ambient environment

In general, the test stand comprises of two inlets, one to deliver gas mixtures and the other to feed in the electrical connection for EIS measurements. In addition, two outlets exit the test stand: one for gas outtake and the other to insert and station an Omega K-type thermocouple directly next to the cell. Further description of this apparatus is provided in this section.

3.1.1 Symmetric Cell Architecture

Electrolyte supported symmetric cells are used for these studies. Due to the complexity of a complete cell architecture, it is ideal to reduce the number of components to pinpoint degradation mechanisms. The studies in this thesis focus on the degradation of the steam electrode. The architecture of these symmetric cells is illustrated in Figure 3.1, where the electrolyte material, BCZYYb in this case, is sandwiched between two BCFZY steam electrodes. Both sides of the symmetric cell are treated identically by adding electrical contact paste and providing an

electrically conductive mesh for EIS measurements. Gold or silver mesh was used for the study in this thesis. The symmetric cell is then inserted into the ceramic coupon assembly.

3.1.2 Ceramic Coupon Assembly

The Degradation Test Stand has an alumina coupon assembly to ensure the elimination of cell contamination from the holding assembly itself. As shown in Figure 3.1, the ceramic coupon assembly comprises of six components: support, isolation ring, two electrical contacts (waffles), collar, and a plunger. The ceramic coupon assembly was designed by Colorado School of Mines graduate student Max Pisciotta, and fabricated by Aremco, Inc; detailed component parts are provided in appendix section A.2. The plunger provides a constant compressive force; different size plungers can be used for specific delivery of compressive load. For this study, 17.3kPa of a compressive load was used. The collar ensures the stability of the plunger, while the waffles sandwich the cell and additional cell components, such as interconnects and/or electrically conductive mesh for current collection. The isolation ring is used to elevate the cell a distance

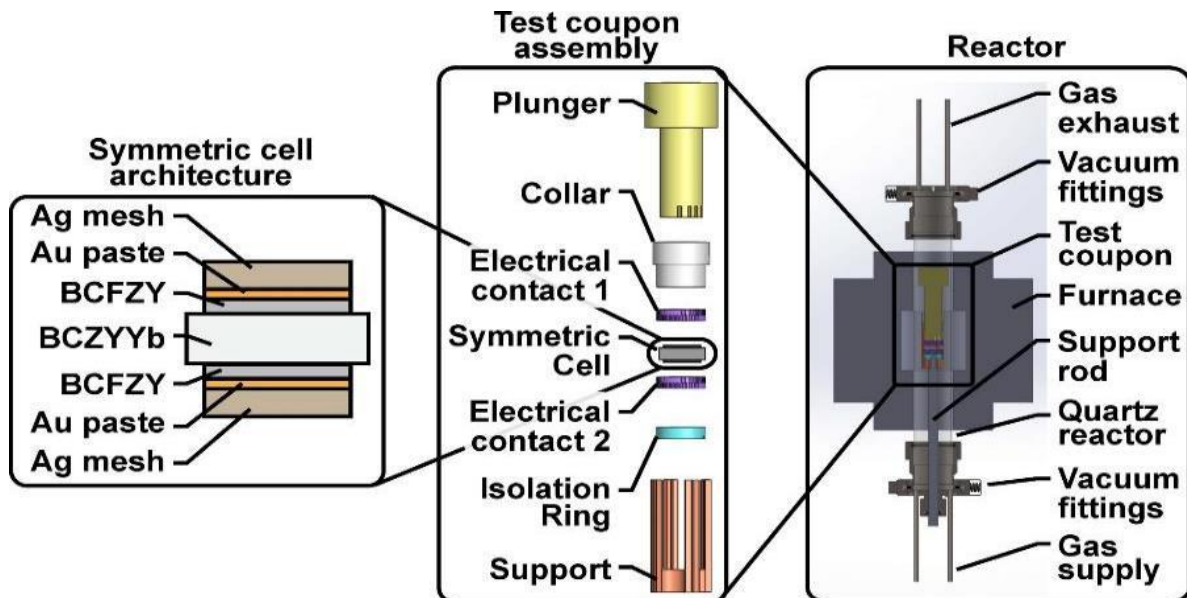


Figure 3.1: Degradation Test Stand and BCZYyb/BCFZY/BCZYyb cell architecture (image not to scale)

from the support component and to electrically isolate any of the electrical wires that connect to the cell for EIS measurements. Lastly, the support component holds all of the other alumina components to ensure stability. The support component also contains a hole on the underside, which is used to mount on a ceramic support rod. The ceramic coupon assembly is then inserted into the reactor.

3.1.3 Test Stand Design

The reactor shown in Figure 3.1 is a quartz tube (Allen Scientific Glass, Inc.), which at operating temperatures, (550-800°C) will not react to poison the cell. The quartz reactor is sealed with vacuum fittings (NW/KF Quick Compression Coupler Components expanded, Pelco), where these fittings contain welded ¼ inch Swagelok piping for the inlets and outlets. Figure 3.2 shows the Degradation Test Stand without the quartz tube, with the furnace opened, and with the

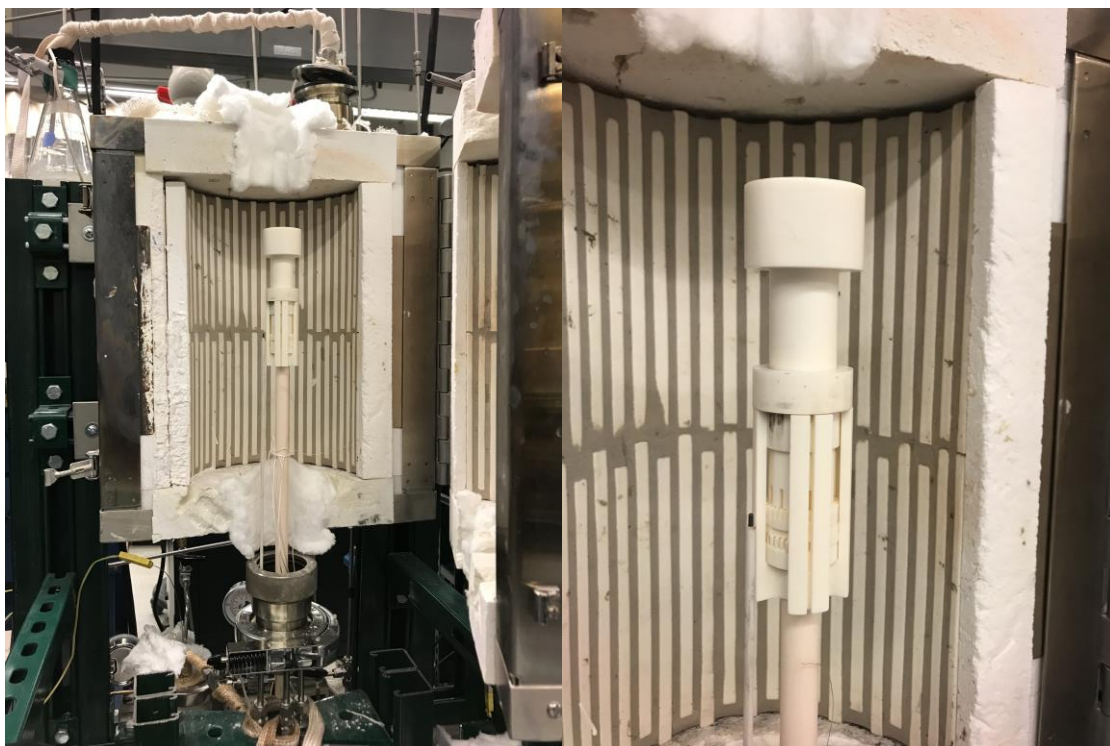


Figure 3.2: Degradation Test Stand, on the left side is the setup without the quartz reactor, on the right is the ceramic coupon assembly held by the alumina rod, and a stationary thermocouple

ceramic coupon assembly. The ceramic support rod is held fixed through one of the vacuum fittings. The quartz tube is sealed within a furnace (Applied Test Systems, INC.), which is powered through a temperature control system (Applied Test Systems, INC.) and a temperature control module (Barber-Colman 2404). Heat rope (Omega) is wrapped around the piping that may be carrying any steam, in order to prevent condensation. A variable autotransformer (Staco Energy Products Co.) is used along the heat ropes to deliver a constant electrical current for a constant temperature of $\sim 100^{\circ}\text{C}$.

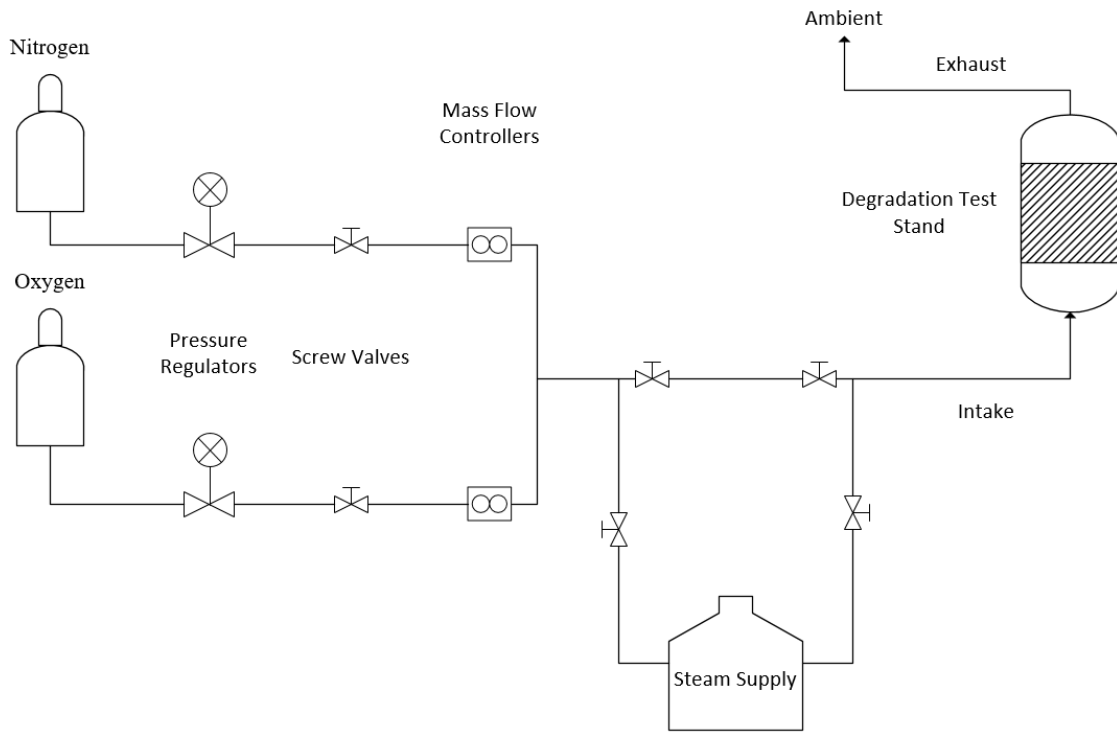


Figure 3.3: Degradation Test Stand physical diagram

A gas flow diagram of the degradation test stand is shown in Figure 3.3. The piping architecture comprises of $\frac{1}{4}$ inch Swagelok components. The test stand feeds gases from two gas cylinders, nitrogen and ultra-high purity oxygen (General Air). A mixture of these two gases produces synthetic air, specifically, 79% nitrogen and 21% oxygen. In order to achieve these

percent values, mass flow controllers (Alicat) are used with an accuracy of +/- 0.6%. Pressure regulators (Matheson) and valves are used for delivery of pure gas from either cylinder at a controlled pressure to prevent any damage to the mass flow controllers. Gas is either mixed at an intersection point, which is then diverted into a water supply to include steam, or the gas can be delivered dry to the experiment. Steam is added via an air stone where the distilled water temperature is controlled with a heating pad around an air tight cylinder through which the temperature is controlled by a temperature controller (Omega CN7800), set to reach a temperature of 41°C at Golden elevation (5,675ft) for a delivery of 10% steam.

3.2 YSZ|LSM Symmetric Cell Experimental Information

As a new type of test stand, the Degradation Test Stand, must be validated for reliability in accuracy and repeatability. This validation is executed using well-established in material performance literature, YSZ|LSM. The YSZ|LSM symmetric cell fabrication process and tools used are described in this section, followed by the experiment preparation.

3.2.1 Material Fabrication of YSZ|LSM Symmetric Cells

The electrolyte Ytria Stabilized Zirconia (YSZ) from Tosoh Corporation is used to form disk cells for validating repeatability and accuracy of the Degradation Test Stand. Specifically, 4g of this YSZ powder is placed into a CARVER 1 1/8in I.D. press die. The die is inserted on a CARVER INC auto series hydraulic press at a pressure of 8000 lb for 20 s. Each disk is settled on an alumina rail batt setter. The sintering procedure is executed from 25 to 1400°C/hr and then aged for 4 hr. After sintering, the electrolytes are wetted and hand grinded flat using LECO spectrum system 1000 with a grit size of P60 FEPA or 120 ANSI. The roughness of the surface ensures electrode adhesion [77-80].

The electrode ($\text{La}_{0.85}\text{Sr}_{0.15}\text{MnO}_{3-\delta}$) (LSM) chemical purity 99.9% from PRAXAIR Surface Technologies was mixed with ink vehicle from Fuelcellmaterials in a 1:1 ratio to form electrode LSM paste. Mixture was done within a lab agate mortar and pestle until the mixture is homogenous. The electrode paste is stored and refrigerated at $\sim 6^\circ\text{C}$. When in use, the paste is stirred with a toothpick to ensure homogeneity. On each sides of the YSZ electrolyte, a disk paper sticker is added with an inner diameter of 0.5 in and an outer diameter of 1.0 in, resulting in a total thickness per electrode of 0.10 mm before sintering. Electrode paste is applied to the inner circle of the sticker paper with a round touch-up brush for solvent-based paint and coating, which is 5/64 in diameter and 0 trade size (specifically Tanis 00330 Srilanka).

The cell is pronged on 3 ceramic cubes, which is then inserted into a Thermo Scientific HERAtherm oven drying furnace at 75°C until all of the electrode paste has dried up ~ 24 hr. Cells may receive an additional electrode paste application and drying in the furnace to ensure a uniform electrode surface. The sticker paper is carefully removed and the YSZ|LSM cells are inserted into a Lingberg/Blue furnace or a Deltech, Inc. furnace for the sintering procedure. The cells are sintered accordingly, 25 to 300°C at $120^\circ\text{C}/\text{hr}$, dwell at 300°C for 1 hr, 300 to 1200°C at $200^\circ\text{C}/\text{hr}$, dwell at 1200°C for 2 hr, and 1200 to 25°C at $120^\circ\text{C}/\text{hr}$.

3.2.2 Testing Setup

YSZ|LSM symmetric cells are prepared for testing by adding a thin layer of gold contact paste (Fuelcellmaterials) on the electrode with a Tanis 00330 Srilanka brush, as shown in step 4 in Figure 3.5 (pg. 31). Gold contact paste is used because of its various properties, as follows [81]:

- high electrical conductivity
- high melting point

- ductility to compensate for CTE of other cell components
- adequate stability and chemical compatibility with cell components
- sintering activity
- porosity level
- and mechanical bond.

Since the gold contact paste dries up quickly, a small dot (1/8 in dia) of gold contact paste mixed with Alfa Aesar alpha-Terpineol (quality 96%) is added at the center of the electrode; this ensures for motion-free in situ sintering with the gold mesh, which acts as a current collector. The UNIQUE Wire Weaving co. inc. gold mesh (80 mesh, 0.1 mm dia) is die pressed into 1in diameter circles. The gold mesh has a 0.1 mm diameter gold wire (Alfa Aesar) woven along the diameter of the mesh. Then gold contact paste is added along this intertwined connection and sintered using a heating gun at 800°C.

The prepared cell is inserted into the ceramic coupon assembly. The wiring between the cell/mesh and the reactor stand is completed with added gold contact paste at the connections in order to reduce contact resistance. After checking for any electrical open and closed circuits, the quartz tube is added and sealed through the vacuum fittings, followed with closing and locking of the furnace.

Testing operates at 800°C at a ramp rate of 180°C/hour and dwell for 5 hr. The gas environment was dry synthetic air (79% N₂ and 21% O₂) with a total volumetric flow rate of 100 SCCM.

3.3 FuelCell Energy Proprietary Contact Paste Study Experimental Information

Following successful validation of the accuracy and repeatability of the Degradation Test Stand, FuelCell Energy requested electrical conductivity characterization of their proprietary contact paste. In this section, a description of experiment fabrication and methods is explained.

3.3.1 Material Fabrication

Symmetric cells are used in order to focus on the performance of a single type of electrode. The electrolyte is BCZYYb4411 which is sandwiched between two BCFZY electrodes. The electrolyte is made by pressing and sintering in a Lingberg/Blue or Deltech,inc. furnace. The electrode paste is painted on either side of the electrolyte and sintered. The fabrication process of BCFZY|BCZYYb|BCFZY is stated in greater detail in section 3.4.

3.3.2 Testing Setup

Supplementary experiments were executed after the validation experiments, but before the characterization experiments of FuelCell Energy's contact paste. The cells for the supplementary experiments are inserted into the test stand without contact paste. The cells are exposed to air + 3% steam at a mass flow rate of 100 SCCM and at a fixed temperature of 800°C with a ramping rate of 60°C/hr. Otherwise the symmetric cells receive treatment as described in the next paragraph.

The experiments with FCE contact paste and Pt contact paste both used silver mesh to establish current collection for EIS measurements, as illustrated in Figure 3.4.

The experiment with Pt contact paste has an additional silver mesh, which was sintered onto electrode surfaces before the experimental setup, as shown in Figure 3.4(a). Contact paste was painted on each electrode and capped with a silver mesh. The cell is inserted and wired into the Degradation Test Stand. FuelCell Energy instructed that the contact paste be sintered in situ at

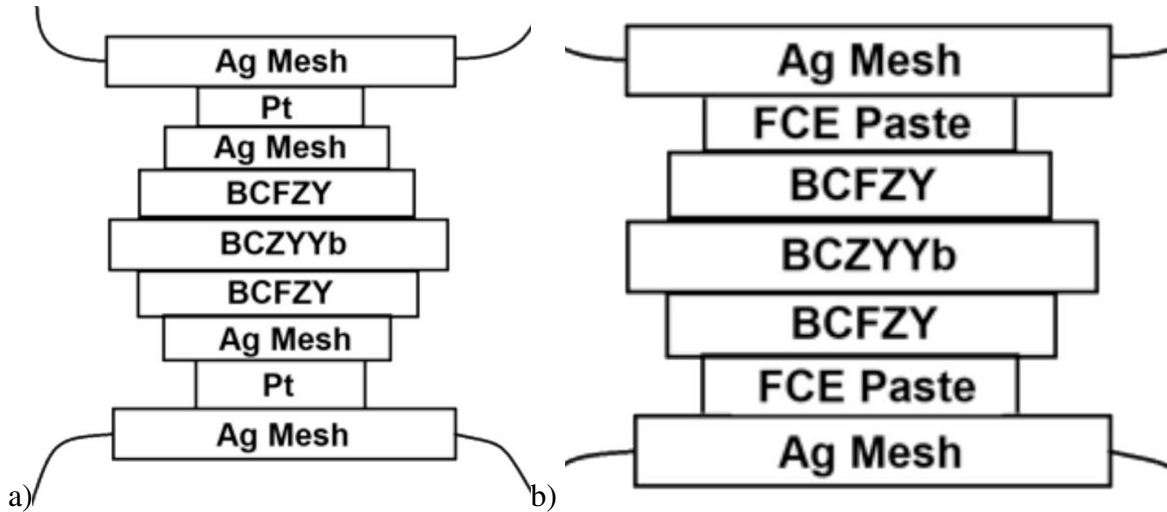


Figure 3.4: Symmetric cell layer structure for FCE proprietary contact paste experiments (not to scale), a) Pt contact paste, b) FCE contact paste

500°C for one hour and then 800°C for one hour at a ramping rate of 60°C/hr. The gas environment was air +3% steam at a mass flow rate of 100 SCCM. The water supply container is maintained at room temperature to provide 3% steam into the gas environment. The operating temperatures ranged from 40-650°C at intervals of 50°C at a ramping rate of 60°C/hr, where each interval temperature was held for 3 hr. EIS measurements were executed at every 50°C intervals from 400-650°C after 1 hr of electrochemical stability on the cell.

3.4 BCZYYb|BCFZY Symmetric Cell Experimental Information

Material fabrication and testing setup for BCZYYb|BCFZY cells for the following experiments are provided in this section:

- stability in humidity: 10% steam VS 50% steam
- electrolyte material stability: BCZYYb7111 VS BCZYYb4411
- stability in pure oxygen

Testing setup is different for each experiment due to different gas environments, while the same symmetric cell fabrication techniques and procedures are used.

3.4.1 Material Fabrication

Production of electrolyte powder (BCZYYb7111 & BCZYYb4411) is described by Duan et al. [8, 82]. The electrolyte powder is mixed with reagent alcohol, and ceramic, cylindrical pellets are added into the solution for mixing. The electrolyte solution is ball milled for 48 hours, and then opened and placed into the drying furnace to evaporate the reagent alcohol. The bottle is capped and inserted into the ball mill for 24 hr. Afterwards, the electrolyte homogenous mixture is then separated from the ceramic pellets with a USA standard test sieve NO. 40. The production of BCFZY electrode powder is described by Duan et al. [8, 83].

Production of BCZYYb|BCFZY symmetric cells is similar to that of YSZ|LSM cells. The electrolyte is formed by mixing 50 g of electrolyte powder with 5 g (10% of 50g) of binder in a lab agate mortar and pestle. The mixture must be homogenous. Afterwards, 5g of this mixture is placed into a CARVER 1 1/8 in I.D. press die. The die is inserted into a CARVER INC auto series hydraulic press at a pressure of 10000 lb for 1 min. With this amount of mixed powder, 10 cells are fabricated and are settled on an alumina rail batt setter. The cells are sintered accordingly, 25 to 450°C at 60°C/hr, dwell at 450°C for 2 hr, 450 to 1500°C at 180°C/hr, dwell at 1500°C for 5 hr, and 1500 to 25°C at 180°C/hr. After sintering is complete shown in step 1 in Figure 3.5, the electrolytes are wetted and hand ground flat using LECO spectrum system 1000 with a grit size of P60 FEPA or 120 ANSI, resulting in step 2 in Figure 3.5; the roughness of the surface ensures electrode adhesion and an increase of electrochemical reactive surface area [77-80].

Fabrication and sintering of electrodes on the electrolyte is executed. The electrode paste is stored and refrigerated at ~6°C; when in use, the paste is stirred with a toothpick to ensure

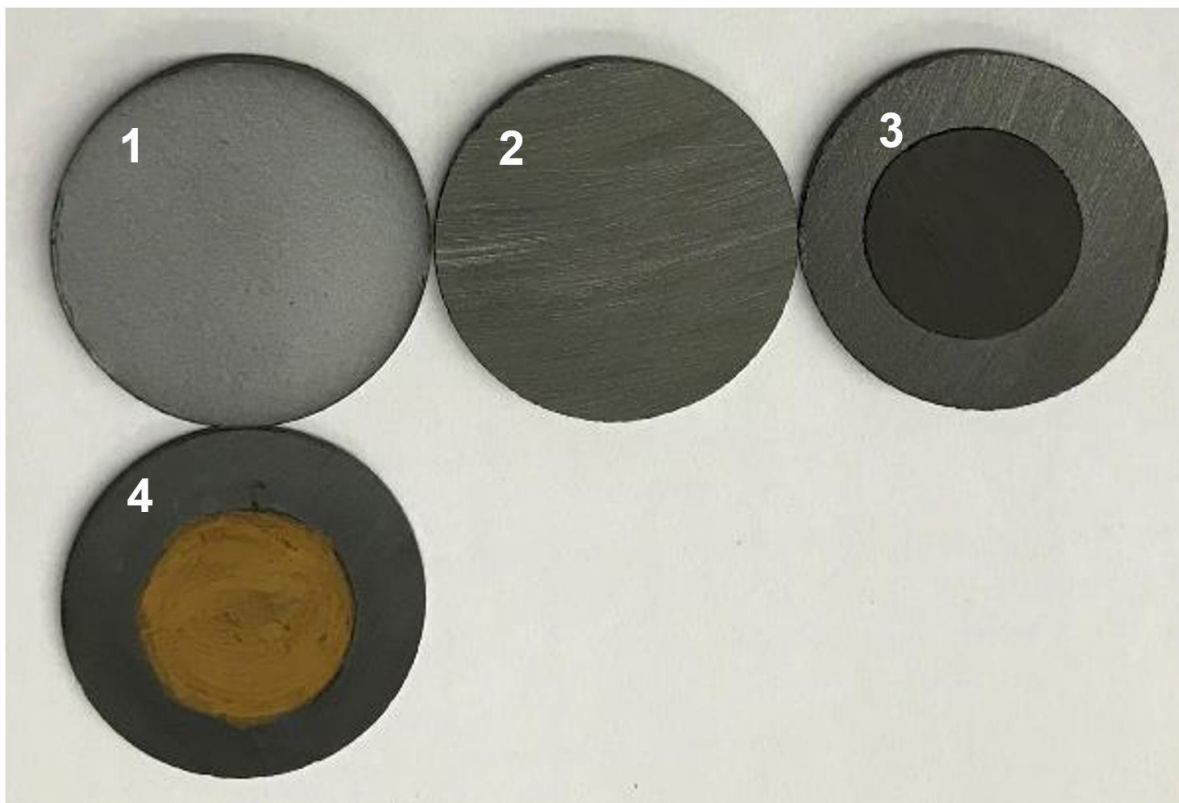


Figure 3.5: Cell fabrication process & experimental readiness

homogeneity. On each side of the electrolyte, a disk paper sticker is added with an inner diameter of 0.5 in and an outer diameter of 1.0 in, resulting in a total thickness per electrode of 0.10 mm before sintering. Electrode paste is applied to the inner circle of the sticker paper with a round touch-up brush for Solvent-based paint and coating, which is 5/64 in diameter and 0 trade size (Tanis 00330 Srilanka). The cell is pronged on 3 ceramic cubes, which is then inserted into a Thermo Scientific HERAtherm oven drying furnace at 75°C until all of the electrode paste is dried up. Cells may receive an additional electrode paste application and drying in the furnace to ensure a uniform surface. The sticker paper is carefully removed and the cell is inserted into a Lingberg/Blue furnace or a Deltech, Inc. furnace for the sintering procedure. The sintering procedure is as follows, 25 to 900°C at 60 °C/hr, dwell at 900°C for 5 hr, and 900 to 25°C at

60°C/hr. The final product is shown in step 3 in Figure 3.5, where the dark section is the electrode and the lighter section is the electrolyte.

3.4.2 Testing Setup

This section presents the experiments that investigate the stability of BCZYYb|BCFZY symmetric cells in various environments and with the integration of interconnect metals. The symmetric cell is prepared for testing by adding a thin layer of gold contact paste (Fuelcellmaterials) on the electrode with a Tanis 00330 Srilanka brush, as shown in step 4 in Figure 3.5. Gold contact paste is used due to its preferred properties and compatibility for degradation studies [81]. Since the gold contact paste dries up quickly, a small dot (1/8 in dia) of gold contact paste mixed with Alfa Aesar alpha-Terpineol (quality 96%) is added at the center of the electrode; this ensures motion-free in situ sintering with the gold mesh, which acts as a current collector. The UNIQUE Wire Weaving co. inc. gold mesh (80 mesh, 0.1 mm dia) is die pressed into 1 in diameter circles. The gold mesh has a 0.1mm diameter gold wire (Alfa Aesar) woven along the diameter of the mesh. Then gold contact paste is added along this intertwined connection and sintered using a heating gun at 800°C in order to reduce contact resistance.

The prepared cell is inserted into the ceramic coupon assembly, shown in Figure 3.1 (pg. 25). The wiring between the cell/mesh and the reactor stand is completed with added gold contact paste at the connections, in order to reduce contact resistance. After checking for any electrical open and closed circuits, the quartz tube is added and sealed through the vacuum fittings, followed with closing and locking of the furnace.

3.4.2.1 Stability in Humidity

The gas environment for this study was air + 10% steam and air + 50% steam. The total volumetric flow rate is 100 SCCM. The electrolyte used was BCZYYb7111 for both humidity

levels. Temperature operation for this set of experiments is at 550°C at a ramp rate of 60°C/hr; the experiment with air + 10% steam dwelled for 1000 hr, while the air + 50% steam experiment dwelled for 235 hr.

3.4.2.2 Electrolyte Material Stability

The material for the electrolytes are $\text{BaCe}_{0.7}\text{Zr}_{0.1}\text{Y}_{0.1}\text{Yb}_{0.1}\text{O}_{3-\delta}$ and $\text{BaCe}_{0.4}\text{Zr}_{0.4}\text{Y}_{0.1}\text{Yb}_{0.1}\text{O}_{3-\delta}$. For this set of studies the gas environment was air + 10% steam for electrolyte BCZYYb7111, while synthetic air (79% N_2 and 21% O_2) was used for electrolyte BCZYYb4411. The flow rate was kept at 100 SCCM. Temperature operation for this set of experiments is at 550°C at a ramp rate of 60°C/hr and dwell for 1000 hr for electrolyte BCZYYb7111 and dwell for 210 hr for electrolyte BCZYYb4411.

3.4.2.3 Stability in Oxygen

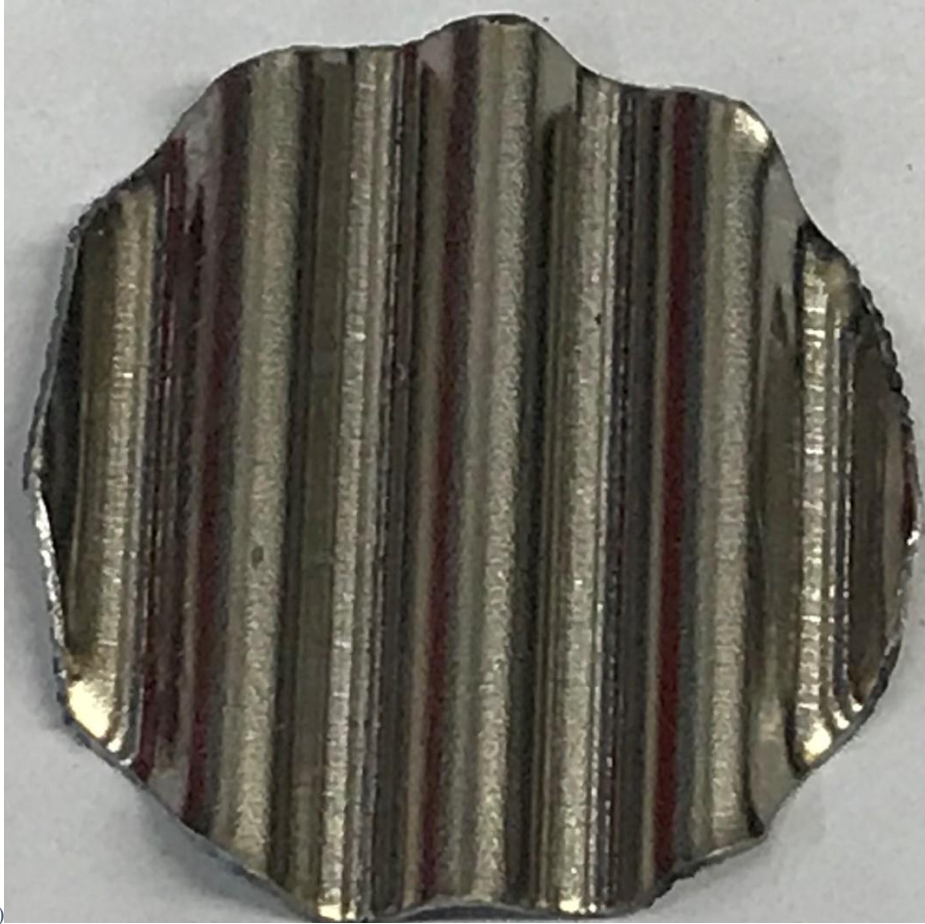
Pure oxygen with no steam was used for the operating gas environment for this study. The flow rate was kept at 100 SCCM and the electrolyte used was BCZYYb4411. The operating temperature was 550°C ramped at a rate of 60°C/hr and dwelled for 1000 hr.

3.5 Interconnect Experimental Information

In this section, Sandvik 441 (Ce/Co coated and uncoated) sheet metal is prepared for symmetric cell integration. Cell pretreatment is included for experiments that study pre-oxidation effects of interconnects on symmetric cells.

3.5.1 Material Preparation

Two types of interconnects were investigated: uncoated Sandvik 441 and Ce/Co coated Sandvik 441. Table 3.1 summarizes the composition of metal interconnects provided by Sandvik Materials Technology. The cerium inner coated layer is ~10 nm thick and the cobalt outer layer is 630 nm thick [12]. Interconnects are cut into rectangles (1in x 1.15in) using snippers. Each



a)



b)

Figure 3.6: Interconnect structure, (a) top view, (b) side view

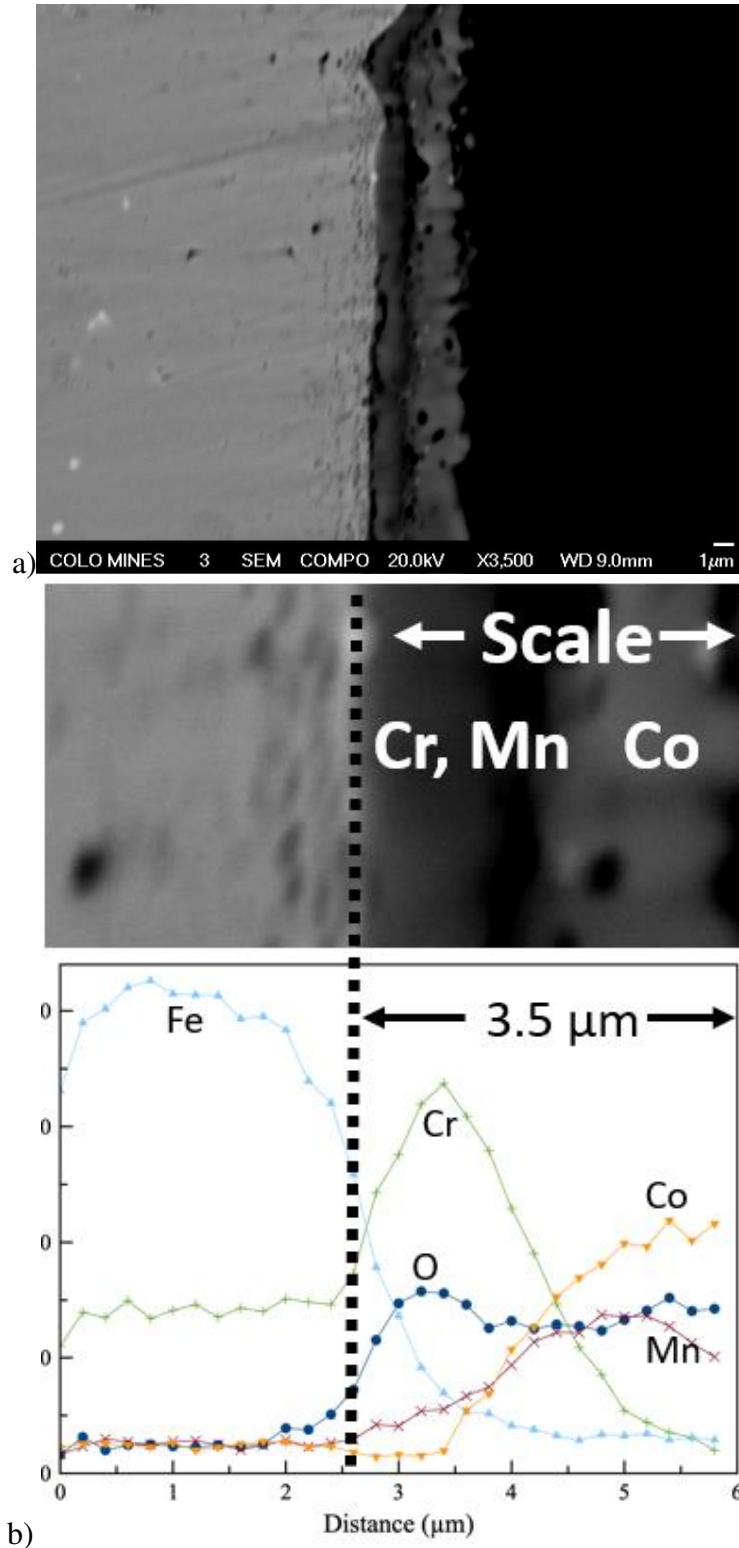


Figure 3.7: Pre-oxidized Ce/Co coated Sandvik 441 (unpublished image courtesy to Carolina Herradon Hernandez) a) interconnect X3,500 resolution, b) interconnect/scale interface composition

rectangular segment is warped using a die press as shown in Figure 3.6. Interconnects were warped in order to ensure adequate steam electrode exposure to the gas environment. For experiments that require treatment for pre-oxidation on interconnects, the cut and warped metal is loaded into a peroxidation stand on a sample holder, which is the support component and the waffle component from the ceramic test coupon assembly.

Table 3.1: Chemical composition of Sandvik 441, given in wt. % [12].

Fe	Cr	C	Mn	Si	S	P	Ni	Nb	Ti
Bal.	17.83	0.012	0.26	0.55	0.002	0.024	0.13	0.48	0.14

The prepared sample holder is inserted into a quartz reactor where the following conditions and procedure takes place: 280SCCM air flow rate of shop air + 3% steam at 900°C for a duration of 30hours [84]. The expected scale in Figure 3.7 correlates with literature for successful scaling of $(\text{Cr,Mn})_3\text{O}_4$ underneath a $(\text{Co,Mn})_3\text{O}_4$ layer [84]. These scales are desired in order to reduce volatile Cr vaporization and suppression of Cr_2O_3 growth. The layers have a total thickness of 3.5 μm .

3.5.2 Testing Setup

For interconnect integrated experiments, the interconnects are inserted on either side of the gold mesh; this allows isolated measurements from the cell and measurements that include the

Symmetric cell architecture With Interconnects

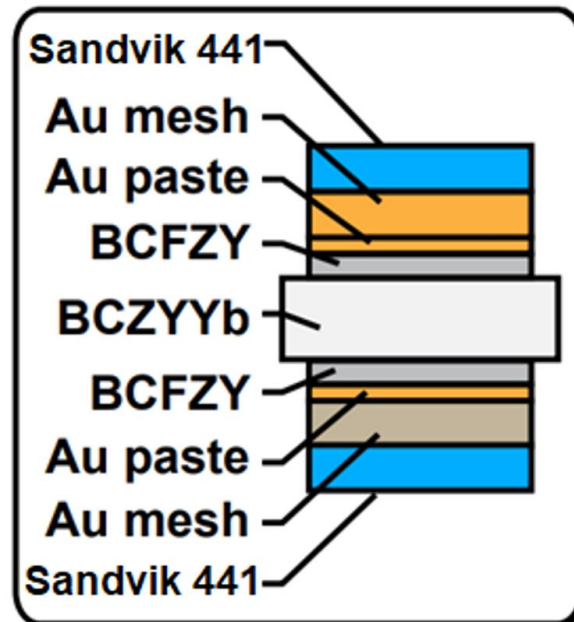


Figure 3.8: Cell with interconnect architecture (not to scale)

interconnects, as shown in Figure 3.8. Gold contact paste is added on one side of the interconnect in order to sinter 0.1mm gold wires with the heat gun to ensure a strong bond during assembly. Gold contact paste with alpha-Terpineol is added to the interconnects so that a sintered bond occurs with the gold mesh during in situ.

3.6 Testing Method

Four-point EIS measurements are taken from the symmetric cell for accurate impedance values from each cell component at a continuous rate. EIS analysis is favored due to the following features [85-87]:

- separate resistance values of bulk layers (electrolyte in this case)
- electrode processes
- interfaces (electrolyte|electrode)

A Gamry Instruments Reference 600+ is used to take accurate measurements (>99% of Ω/Hz accuracy) of the symmetric cell. The parameter for this study is a frequency range of 0.1Hz-0.1MHz at the default setting of 10mV RMS. A low voltage protects the electrode from delamination from the electrolyte [88]. Each EIS curve is analyzed using a circle tracing program built with RStudio, which is executed on the Nyquist plot produced by the Gamry Framework software. As depicted in Figure 3.9, DC resistance and polarization resistance values are extracted as intersection points in the real axis [86, 87, 89-91]. The small semicircle is the electrode to electrolyte charge transfer impedance, and the large semicircle is the electrode reactions such as adsorption and dissociation.

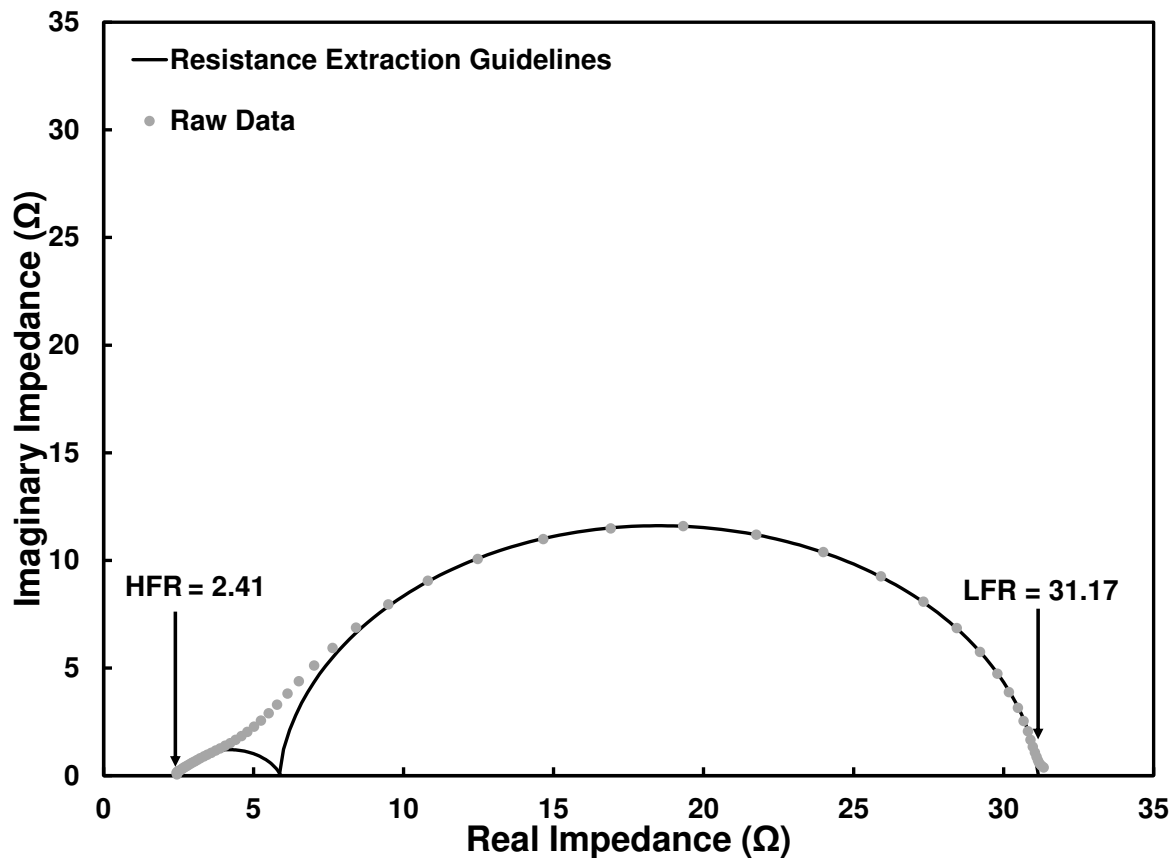


Figure 3.9: Extraction of fuel cell resistance values from Nyquist (EIS) plot

3.7 Method of Calculations

The following equations and relations were used to obtain ASR values, and resistivity and conductivity values [93]. A sample calculation is provided at the end of this section.

Resistance

$$R_{DC} = HFR [\Omega] \quad (3.1)$$

$$R_{polarization} = LFR - HFR [\Omega] \quad (3.2)$$

HFR: High frequency resistance

LFR: Low frequency resistance

Area specific resistance values

$$ASR_{DC} = R_{DC} * MAA [\Omega cm^2] \quad (3.3)$$

$$ASR_{polarization} = \frac{R_{polarization} * MAA}{2} [\Omega cm^2] \quad (3.4)$$

ASR_{DC}: DC area specific resistance

ASR_{polarization}: Polarization area specific resistance

R_{DC}: DC resistance

R_{polarization}: Polarization resistance

MAA: Mean active area

Resistivity and conductivity

$$resistivity = \frac{ASR_{DC}}{t} [\Omega cm] \quad (3.5)$$

$$conductivity = \frac{1}{resistivity} \left[\frac{S}{cm} \right] \quad (3.6)$$

t = Cell thickness

3.7.1 Sample Calculation

Using the values from Figure 3.9, the following calculation provides the ASR resistance values and electrical conductivity properties for a validation experiment using YSZ|LSM symmetric cell.

Resistance

$$R_{DC} = HFR = 2.41\Omega \quad (3.7)$$

$$R_{polarization} = LFR - HFR = 31.17\Omega - 2.41\Omega = 28.76\Omega \quad (3.8)$$

Area specific resistance values

$$ASR_{DC} = R_{DC} * MAA = 2.41\Omega * \frac{126.67mm^2}{100\frac{mm^2}{cm^2}} = 3.05\Omega cm^2 \quad (3.9)$$

$$ASR_{polarization} = \frac{R_{polarization} * MAA}{2} = \frac{28.76\Omega * 126.67mm^2}{2 * 100\frac{mm^2}{cm^2}} = 18.22\Omega cm^2 \quad (3.10)$$

Resistivity and conductivity

$$resistivity = \frac{ASR_{DC}}{t} = \frac{3.05\Omega cm^2}{1.95mm/10\frac{mm}{cm}} = 15.64\Omega cm \quad (3.11)$$

$$conductivity = \frac{1}{resistivity} = \frac{1}{15.64\Omega cm} = 0.063 \frac{S}{cm} \quad (3.12)$$

CHAPTER 4

RESULTS AND DISCUSSION

In this chapter, the following experimental results are discussed:

4.1 Validation of Degradation Test Stand

4.2 Performance characterization of FuelCell Energy's proprietary contact paste

4.3 Humidity stability: 10% steam VS 50% steam

4.4 Electrolyte material stability: BCZYYb7111 VS BCZYYb4411

4.5 Oxygen-rich gas environment stability

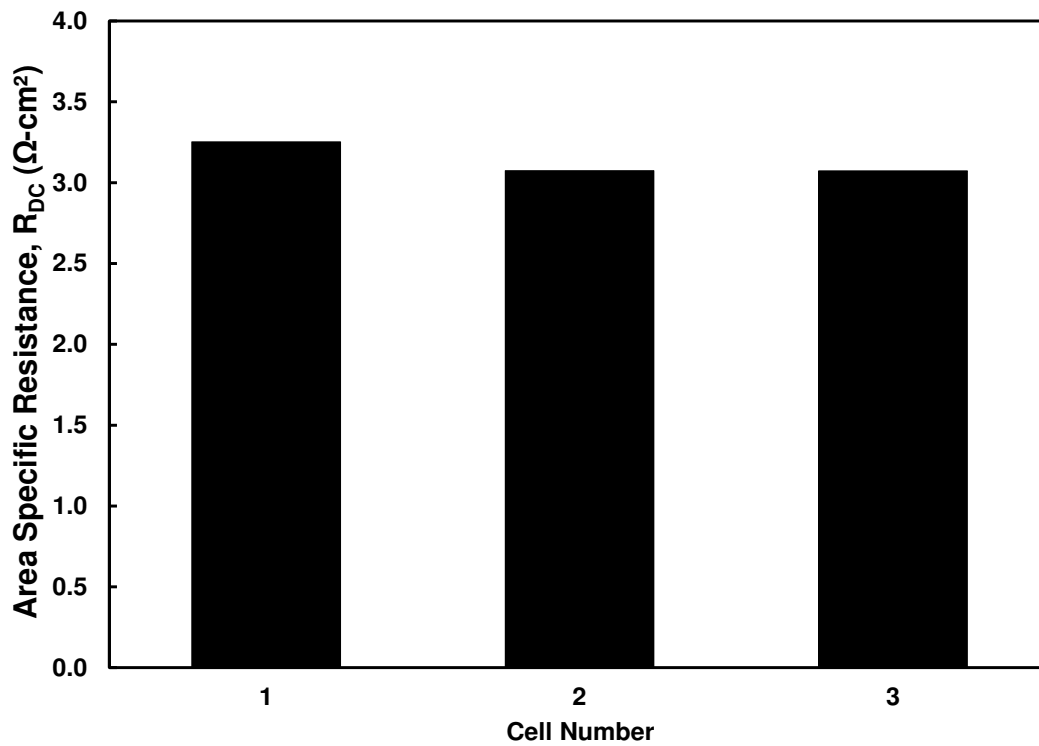
4.6 Interconnect degradation: uncoated untreated Sandvik 441 VS Ce/Co coated untreated Sandvik 441

4.7 Supplementary Results: NiOBCZYYb|BCZYYb7111 Anode Degradation

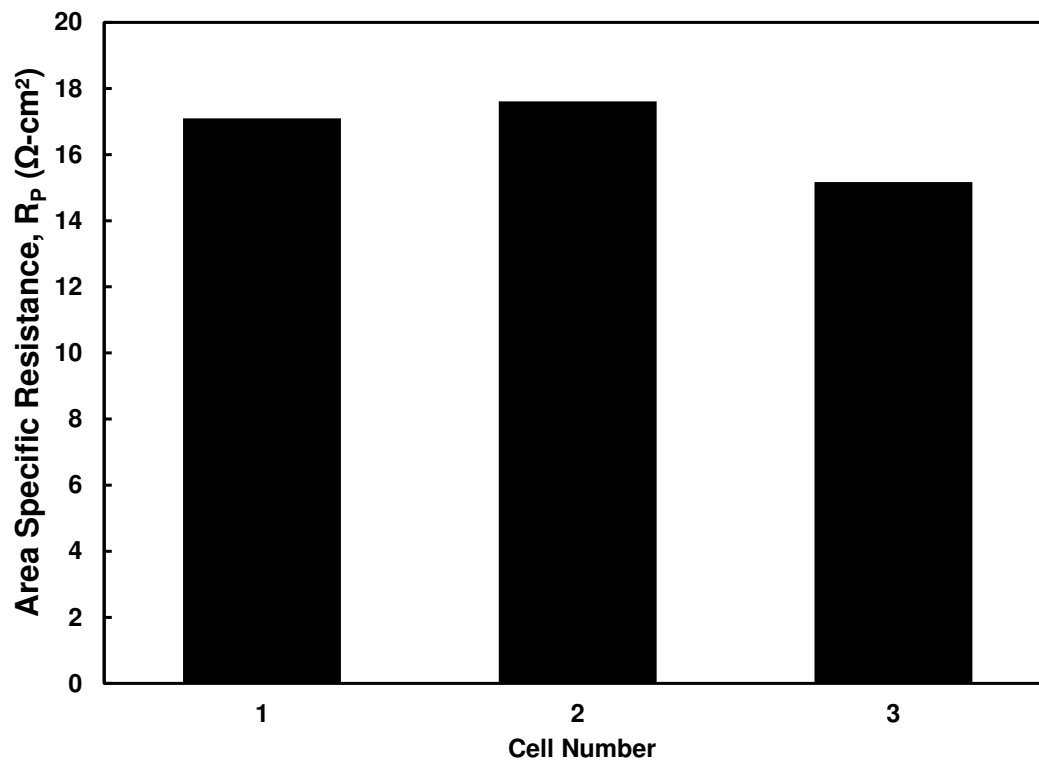
4.1 Validation of Degradation Test Stand with YSZ|LSM Symmetric Cells

Since the Degradation Test Stand is a new experimental apparatus, validation of accuracy and repeatability is necessary. YSZ|LSM symmetric cells are used with gold contact paste and gold mesh to measure polarization area specific resistance and DC area specific resistance through EIS. The operating conditions for these validation experiments are 100 SCCM of dry air at 800°C.

Repeatability of the Degradation Test Stand is confirmed through these YSZ|LSM verification tests, as depicted in Figure 4.1. DC ASR for each cell is 3.25 Ωcm^2 , 3.07 Ωcm^2 , and 3.07 Ωcm^2 , consecutively to Figure 4.1(a). Cell 2 and cell 3 have the same values, while cell 1 has a percent difference of 5.69%. Polarization ASR for each cell is 17.09 Ωcm^2 , 17.61 Ωcm^2 , and 15.17 Ωcm^2 , consecutively, as shown in Figure 4.1(b). The percent difference between cell 1 and cell 2 is 3.00%, the smallest difference, while the percent difference between cells 2 and 3 is



a)



b)

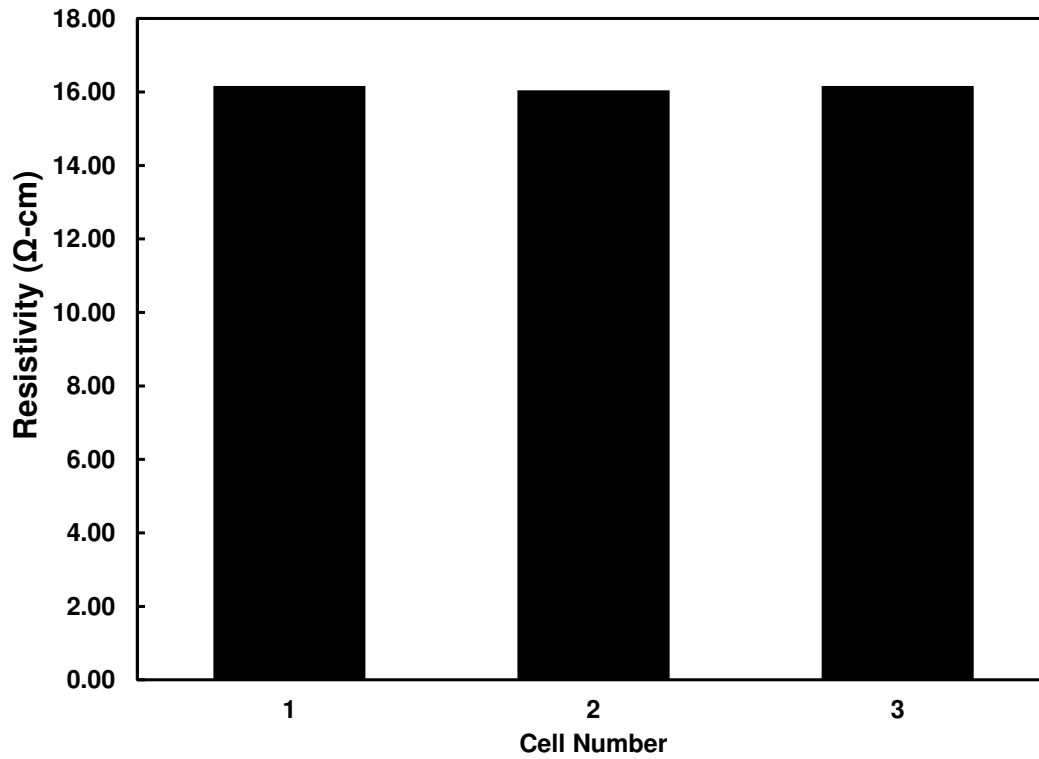
Figure 4.1: Repeatability validation of test stand through ASR, (a) DC ASR, (b) Polarization ASR

the largest difference of 14.89%. The percent difference of polarization ASR varies more than DC ASR measurements; the reason for this is unclear, but may be due to fabrication procedures that could change the porosity and surface roughness of the electrodes. Accuracy of DTS can be correlated through polarization ASR values, which fall with the range of 7.5-19.8 Ωcm^2 for coarse grained electrode LSM_{1.0} without YSZ and fine grained electrode LSM_{1.26} without YSZ, respectively, as demonstrated by Østergård et al. [93].

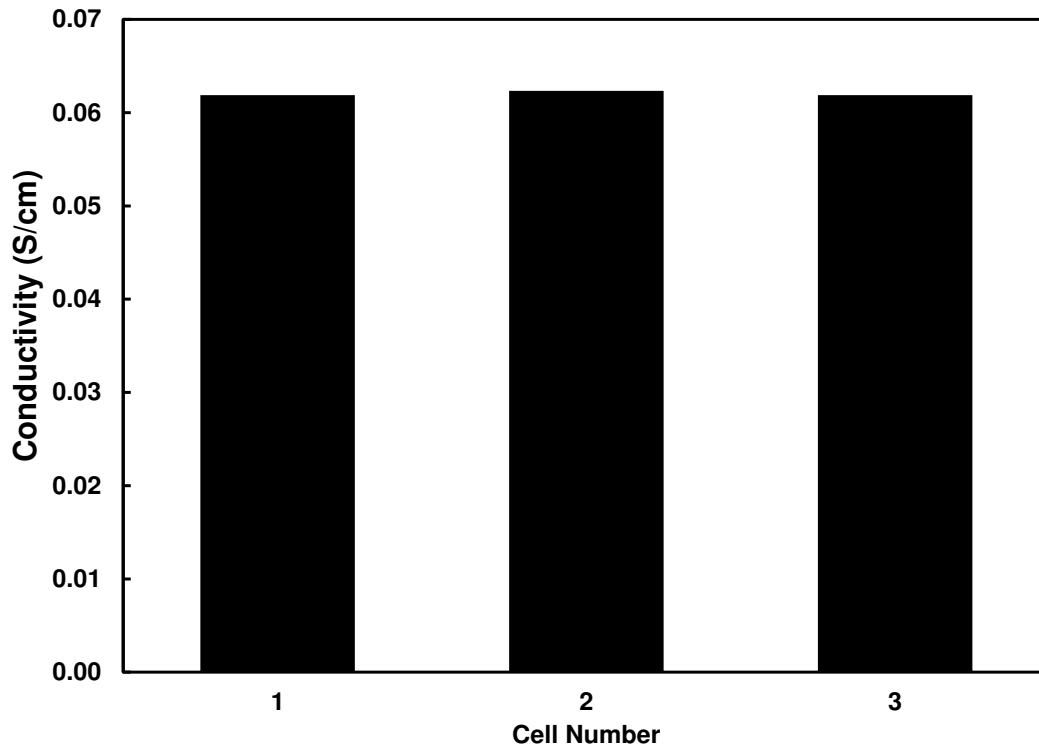
Table 4.1: Conductivity and resistivity values of YSZ, conductivity is in S/cm and resistivity is in (Ωcm)

Temperature °C	This work	Zhu et al. [94]	Kumar et al. [95]	Ahamer et al. [96]	Kwon et al. [97]
800	0.0619 (~16.16)	(25)	~0.067	0.052	0.056

Accuracy of measurements is shown through resistivity and conductivity. The resistivity of each cell is 16.16 Ωcm , 16.04 Ωcm , and 16.16 Ωcm , consecutively to Figure 4.2(a). Cell 1 and cell 3 have the same resistivity values, with cell 2 contributing to a percent difference of 0.74%. Similarly, conductivity values are 0.0619 S/cm, 0.0623 S/cm, 0.0619 S/cm, consecutively to Figure 4.2(b). Since the conductivity is the inverse of resistivity, the relationship in percent difference holds. Table 4.1 compares YSZ conductivity and resistivity values to literature results. Zhu et al. showed a 25 Ωcm resistivity of YSZ symmetric cell with porous Pt electrodes, and an embedded Pt wire in the electrolyte. Kumar et al. showed a ~0.067 S/cm conductivity of YSZ electrolyte without including electrodes, while covering both surfaces of the specimen with



a)



b)

Figure 4.2: Accuracy validation of test stand through electrical conductivity properties
 (a) Resistivity, (b) Conductivity

platinum foil and applying pressure by tightening a screw on the cell fixture. Additionally, the result from this study has a higher conductivity than 0.052 S/cm from Ahamer et al. and 0.056 S/cm from Kwon et al. in 2% steam + hydrogen.

Before the performance characterization of FuelCell Energy’s proprietary contact paste, supplementary experiments were executed. These supplementary experiments repeated the Degradation Test Stand validation study, and investigated the effect of the addition of contact paste.

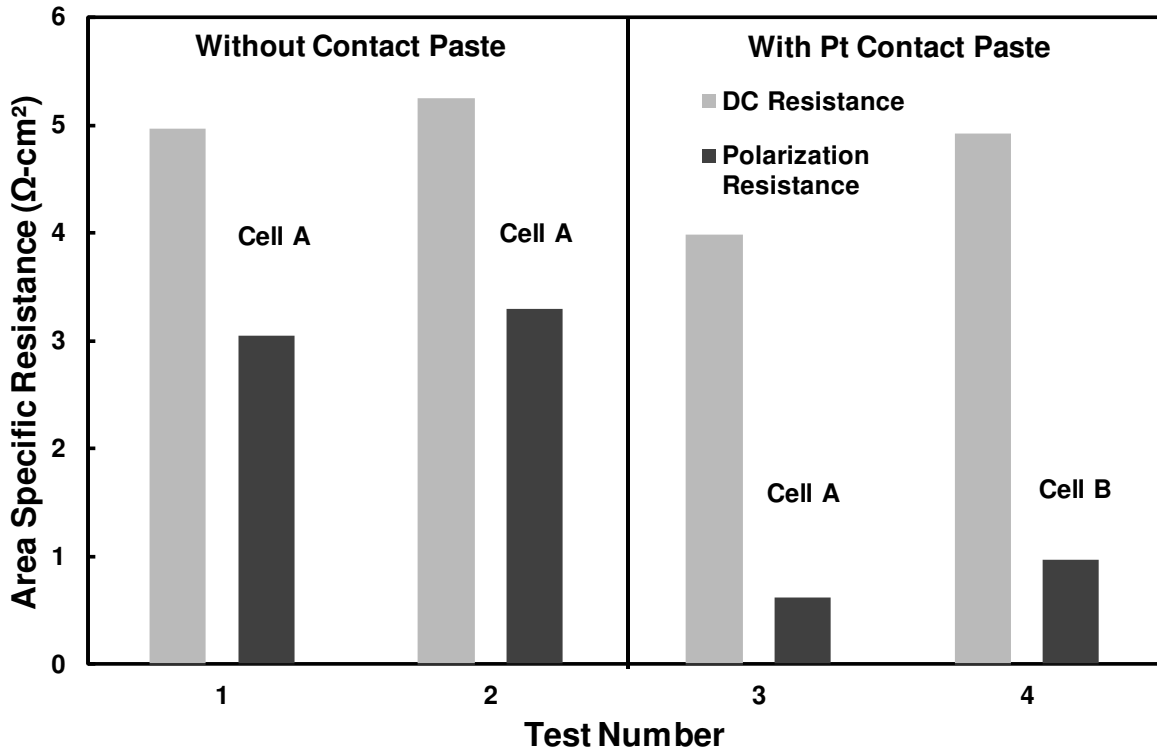


Figure 4.3: YSZ/LSM supplementary validation experiments and effects of contact paste

Two YSZ|LSM symmetric cells were used to confirm the effects of contact paste as a fuel cell component. The results in Figure 4.3 show that contact paste can improve electron flow in fuel cell technology to improve electrical conductive properties. Tests 1, 2, and 3 are the same cell (Cell A), while test 4 (Cell B) is a different cell. The experiment setup for a cell was

completely disassembled and reassembled for validation of repeatability. Test 1 and test 2 show repeatability of assembly setup process; the DC ASR percent difference is 5.68% and the polarization ASR percent difference is 7.87%. Similar to the previous results, the difference in experiments shows reasonable repeatability.

When contact paste is introduced to Cell A, in tests 2 and 3, the DC ASR and polarization ASR percent differences are 27.51% and 136.73%, respectively. Test 4 shows a similar resistance reduction when Pt contact paste is included. The percent difference between test 2 and test 4 are 6.48% and 109.13% in DC ASR and polarization ASR, respectively. The addition of contact paste significantly improves the electrical conductivity of the electrodes.

4.2 Performance Characterization of FuelCell Energy’s Proprietary Contact Paste at Intermediate Temperatures

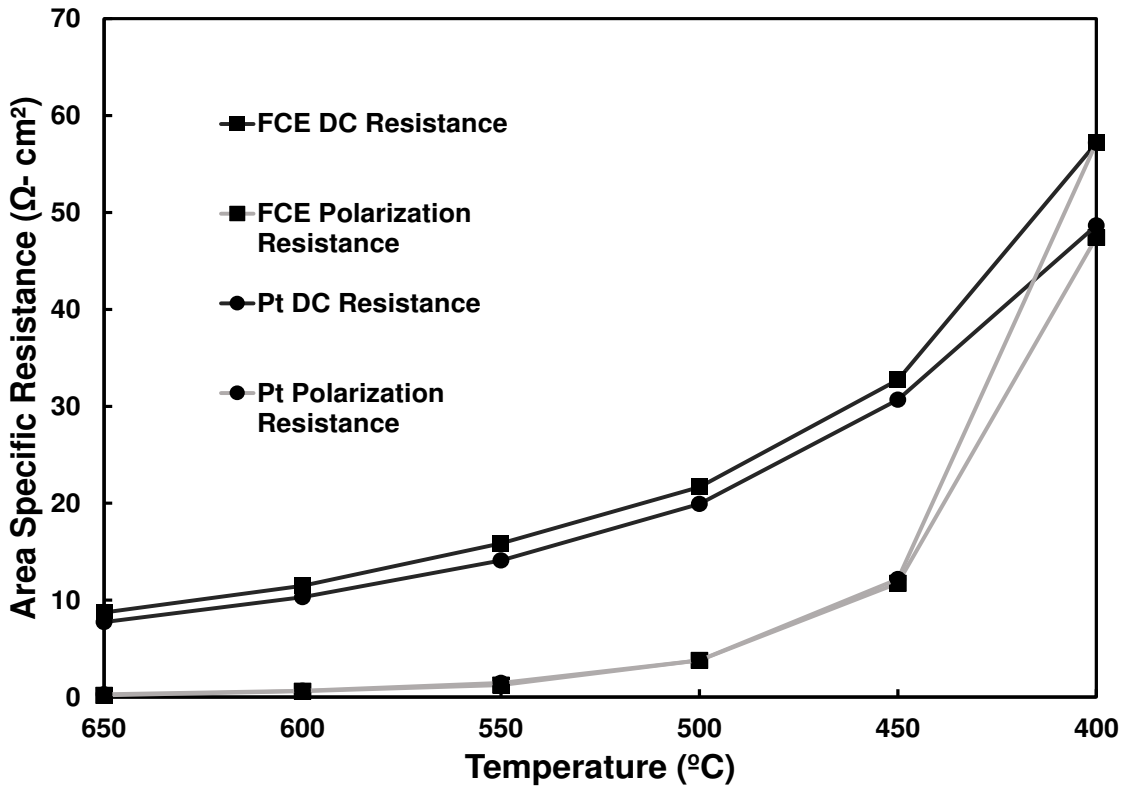


Figure 4.4: Area specific resistance characterization of FCE proprietary contact paste with Pt contact paste

Figure 4.4 shows the comparison of FuelCell Energy’s proprietary contact paste and Pt contact paste on BCZYYb7111|BCFZY symmetric cells in 3% steam + air. The resulting trend for decreasing temperature matches with expected increasing resistance for both experiments. The polarization ASR values for either contact paste are identical from 450-650°C. The DC ASR values are quite similar within this same temperature range. The largest difference within this temperature range is 6.43% in DC ASR. The reason for this slight difference in DC resistance may be caused by the difference in electrolyte thickness, which would be a manufacturing issue. The most noticeable contrast of measured resistance values is at 400°C with a percent difference of 18.65% and 16.13% for polarization ASR and DC ASR, respectively.

The total conductivity values of BCZYYb7111 with Pt contact paste or with FuelCell Energy’s proprietary contact paste are shown in Figure 4.5(a). The plots in Figure 4.5(b) are obtained from the Arrhenius equation,

$$k = Ae^{-\frac{E_A}{RT}} \quad (4.1)$$

k: Rate constant

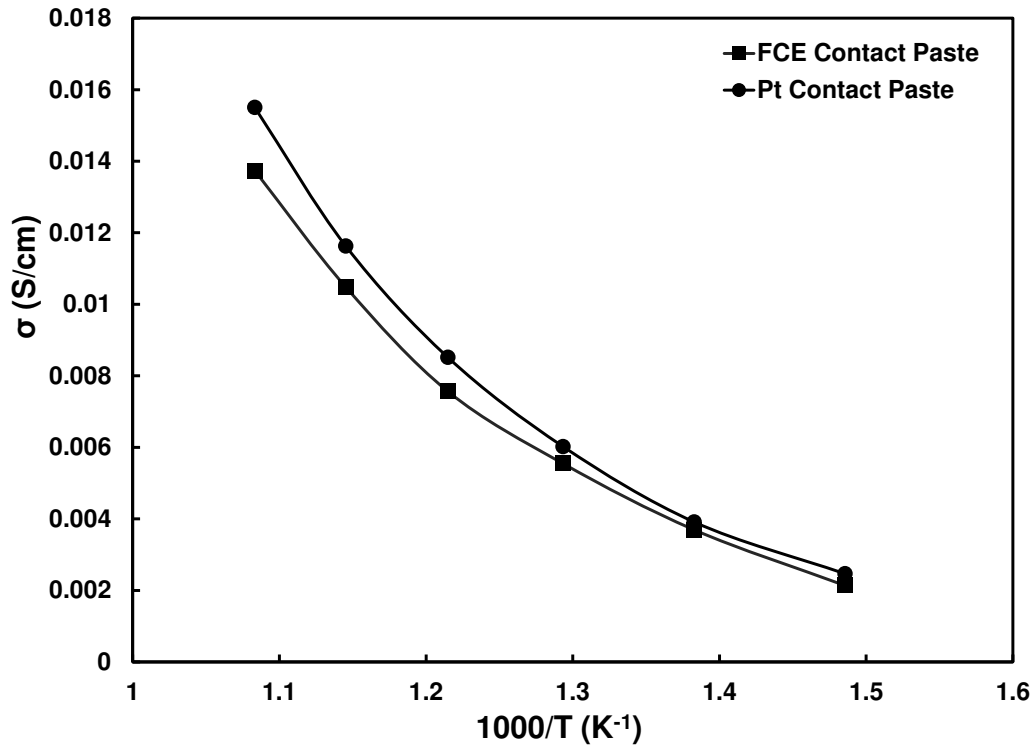
A: Frequency factor

E_A: Activation energy

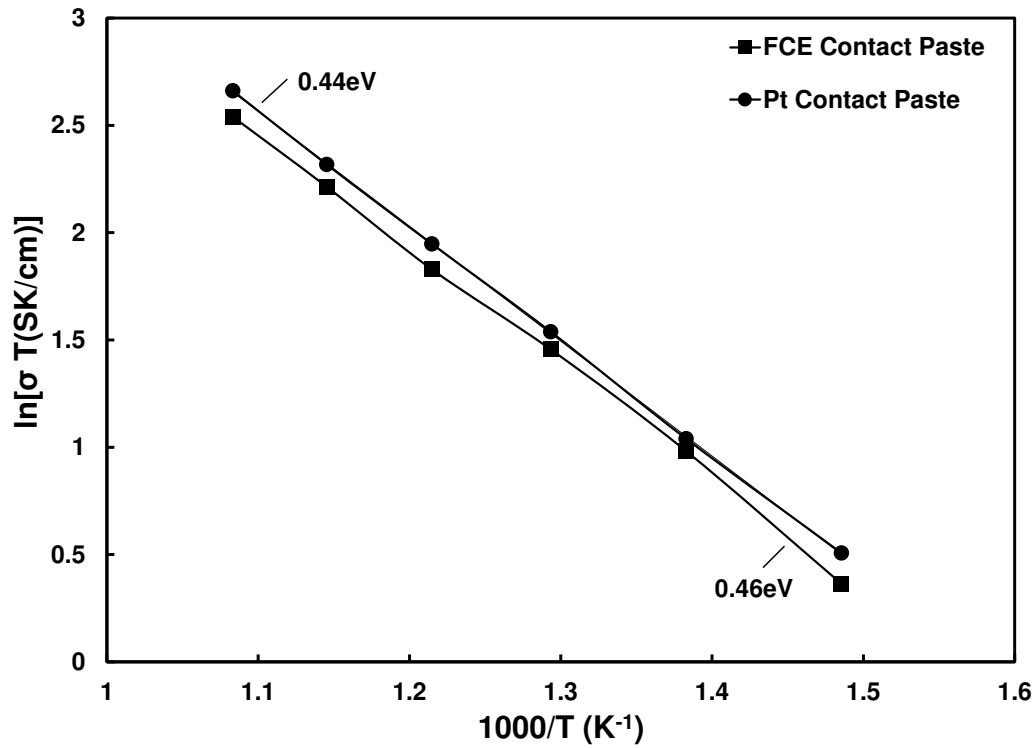
R: Gas constant

T: Temperature [K]

Table 4.2 summarizes Figure 4.5 and compares the values to literature results. The conductivity values of Pt contact paste and FCE contact paste have a maximum difference of 18 S/cm and a minimum difference of 3 S/cm. The conductivity of BCZYYb7111 for both contact pastes correlates with literature results. These comparisons further validate the reliability of the Degradation Test Stand. According to these results, FuelCell Energy’s proprietary contact paste



a)



b)

Figure 4.5: Characterization of FCE proprietary contact paste, (a) conductivity of BCZYYb7111, (b) Arrhenius plots of BCZYYb7111

demonstrates adequate electrical conductivity for use in intermediate temperatures. Furthermore, Figure 4.5(b) shows that the activation energy of BCZYYb7111 is 0.44eV and 0.46eV for Pt contact paste and FCE contact paste, respectively. Clark et al. showed that the low-energy slope for BCZYYb7111 was ~0.35eV in 3% steam + 5% H₂ (bal. Ar), and Zhang et al. showed a low-energy slope of 0.52eV in 5% steam + air and 0.47eV in 5% steam + 5% H₂ (bal. N₂) [98,99]. The results for the activation energy of BCZYYb7111 is within the range for a proton conductor: 0.4eV and upwards [100].

Table 4.2: Conductivity values of BCZYYb7111 with Pt contact paste or FCE contact paste compared to literature values, conductivity is in S/cm (ln(S/cm))

Temperature °C	Pt contact Paste	FCE contact Paste	Clark et al. [98]	Duan et al. [8]	Zhu et al. [101]
400	0.0024 (-6.00)	0.0021 (-6.14)	~0.002	-	-
450	0.0039 (-5.54)	0.0036 (-5.60)	~0.004	-	-
500	0.0060 (-5.11)	0.0055 (-5.19)	~0.008	~0.0045	-
550	0.0085 (-4.76)	0.0075 (-4.88)	~0.010	~0.0068	~0.009
600	0.0116 (-4.45)	0.0104 (-4.55)	~0.012	~0.0100	~0.011
650	0.0155 (-4.16)	0.0137 (-4.28)	~0.015	-	-

4.3 Humidity Stability with BCZYYb7111: 10% steam and 50% steam

For this investigation, BCZYYb7111|BCFZY was studied at different steam environments to determine if humidity depletes the performance of the steam electrode through corrosion. As shown in Figure 4.6, the polarization ASR at 50% steam + air increases at an alarming rate of $0.551 \Omega\text{cm}^2/\text{hr}$, compared to the polarization ASR at 10% steam + air which steadily increases by $3.048 \text{ m}\Omega\text{cm}^2/\text{hr}$. The DC ASR for either case is not as large as the polarization ASR: $7.251 \text{ m}\Omega\text{cm}^2/\text{hr}$ at 50% steam + air and $2.641 \text{ m}\Omega\text{cm}^2/\text{hr}$ at 10% steam + air. The experiment with air + 50% steam was stopped short due to rapid performance degradation.

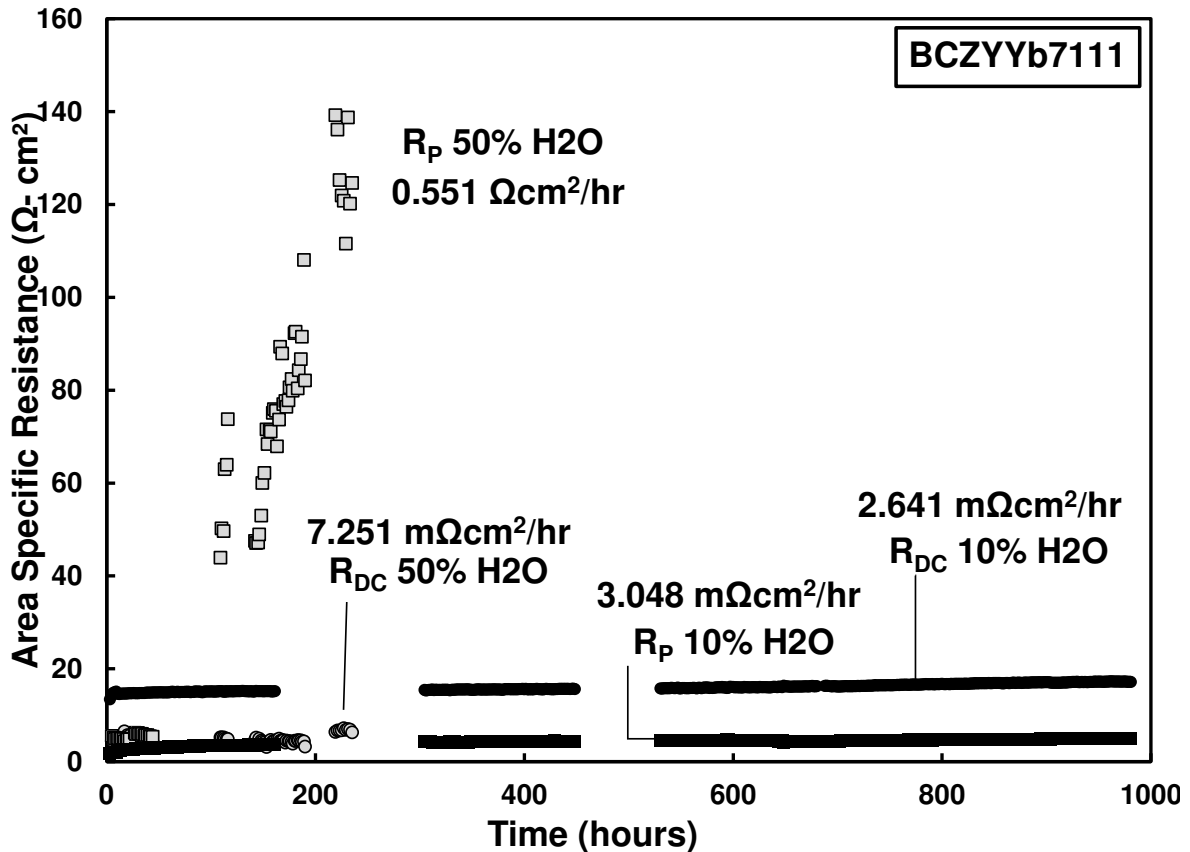


Figure 4.6: Degradation of BCZYYb7111/BCFZY in different steam content

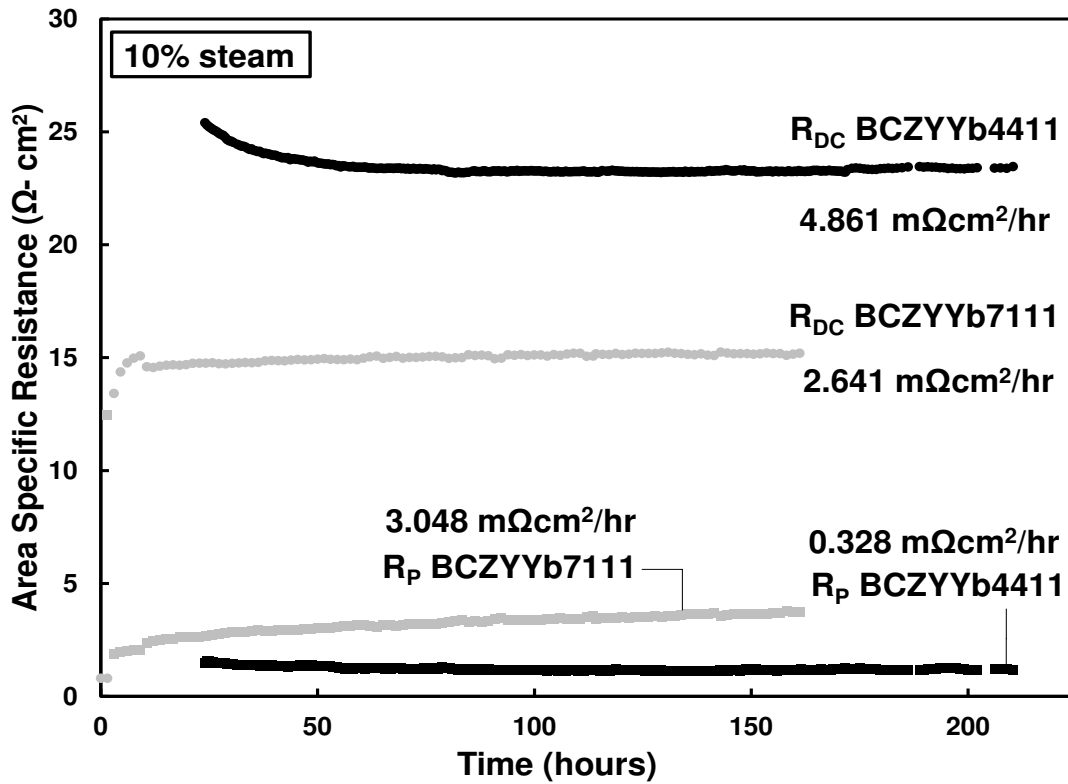
The BCFZY electrode has an average ASR value of $\sim 4 \Omega\text{cm}^2$ and $\sim 120 \Omega\text{cm}^2$ for 10% steam and 50% steam respectively. These values are higher than Ren et al. [102] which demonstrated $0.7 \Omega\text{cm}^2$ in 3% steam and air at 550°C . In similar conditions as Ren et al. the ASR value of BCFZY is $1.46 \Omega\text{cm}^2$ and $1.22 \Omega\text{cm}^2$ for Pt contact paste and FCE contact paste, respectively; therefore, these values are higher.

Ding showed a conductivity of $\sim 0.055 \text{ S/cm}$ for BCZYYb7111 in 50% steam + air at 650°C , compared to $\sim 0.02 \text{ S/cm}$ in this study in the same atmosphere at 550°C [103]. The conductivity of BCZYYb7111 increased from $\sim 0.008 \text{ S/cm}$ in 3% steam + air to $\sim 0.02 \text{ S/cm}$ 50% steam + air. This implies that the conductivity not only increases due to temperature, but is also proportional to the amount of steam. Additionally, the conductivity of BCZYYb7111 is $\sim 0.0087 \text{ S/cm}$ in 10% steam + air at 550°C which greater than the value in Table 4.2 for the same temperature in 3% steam + air.

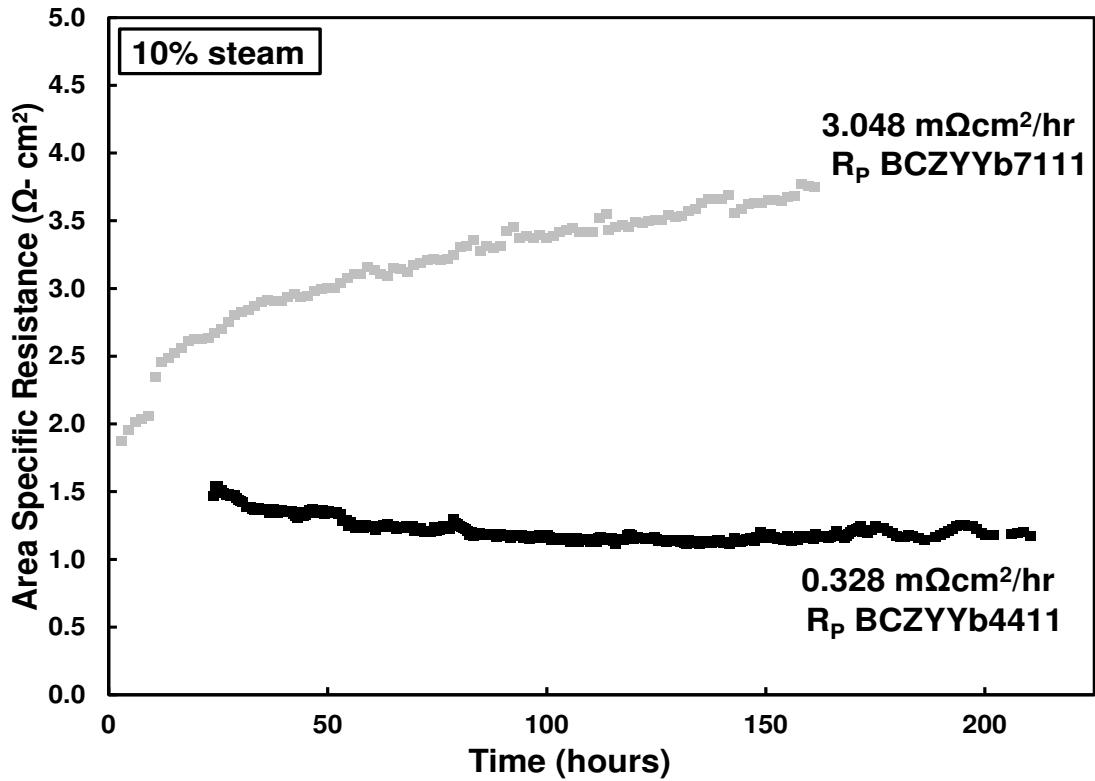
High steam content has a large effect on the polarization ASR, while the DC ASR maintains a steady lower degradation rate. At a low steam level, the degradation rate of both the DC and polarization ASR remain steady and less than $3.1 \text{ m}\Omega\text{cm}^2/\text{hr}$. High content of water in air drastically increases the polarization ASR compared to low steam content.

4.4 Electrolyte Stability: BCZYYb7111 and BCZYYb4411

In order to compare the stability of BCZYYb4411|BCFZY and BCZYYb7111|BCFZY, the gas environment was maintained at 10% steam + air. Figure 4.7(a) shows that the change of DC ASR is steady after 100 hours of operation. BCZYYb4411 changes by $4.861 \text{ m}\Omega\text{cm}^2/\text{hr}$, while BCZYYb7111 changes by $2.641 \text{ m}\Omega\text{cm}^2/\text{hr}$. The polarization ASR behavior is shown in



a)



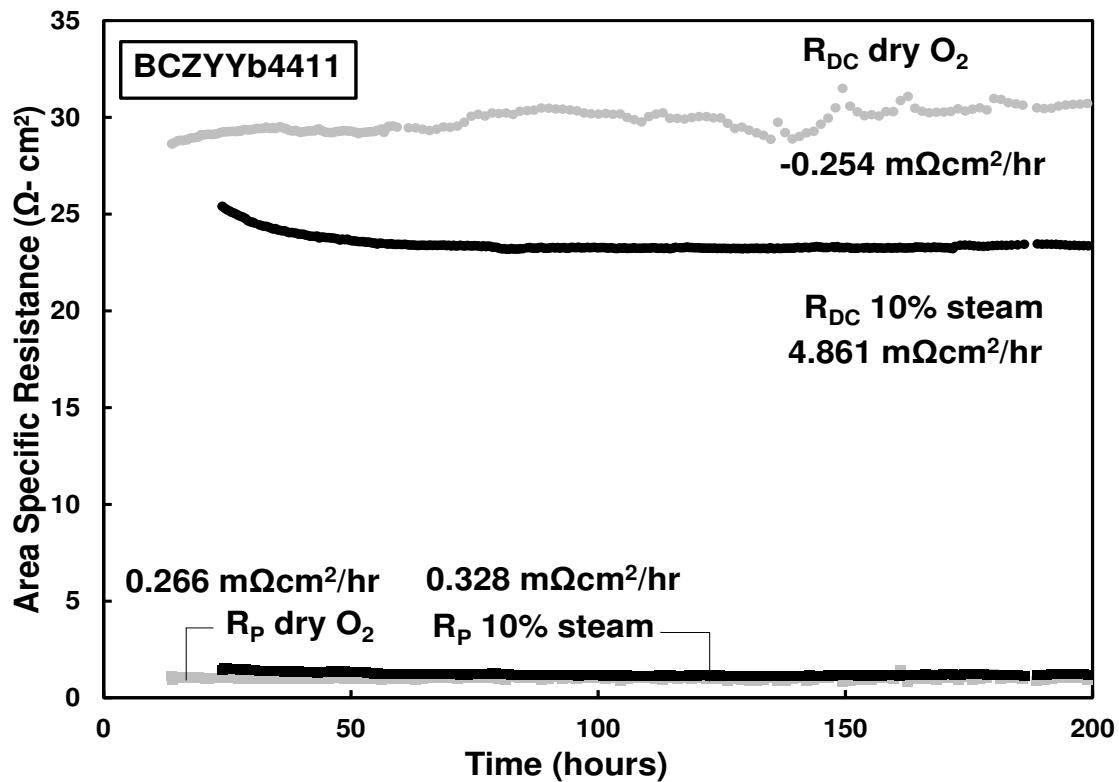
b)

Figure 4.7: Comparison of BCZYb7111 & BCZYb4411 in 10% steam & air, (a) DC & polarization ASR, (b) Polarization ASR

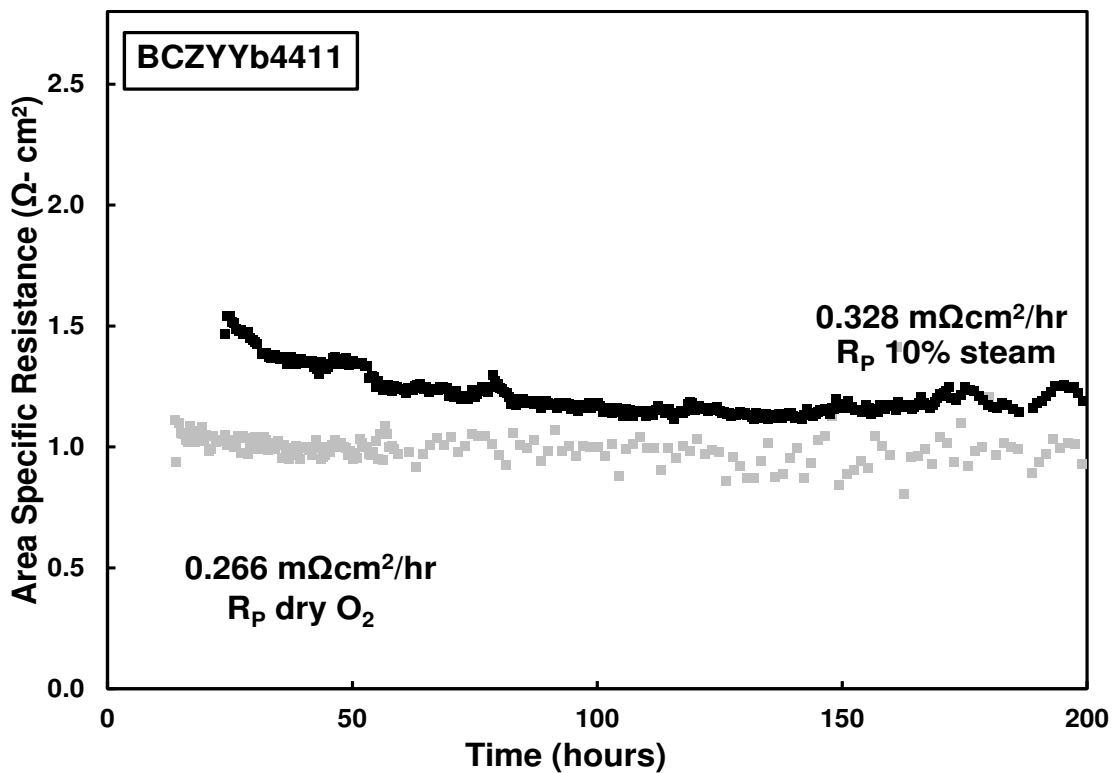
Figure 4.7(b); the change of BCZYYb4411 is $0.328 \text{ m}\Omega\text{cm}^2/\text{hr}$ and the change of BCZYYb7111 is $3.048 \text{ m}\Omega\text{cm}^2/\text{hr}$.

In addition, the conductivity of BCZYYb4411 at 550°C in this study in 10% steam + air is 0.0064 S/cm , compared to literature result of $\sim 0.025 \text{ S/cm}$ in humidified N_2 atmosphere ($p_{\text{H}_2\text{O}} = 0.031 \text{ atm}$) [104]. Ding demonstrated BCZYYb4411 conductivity of $\sim 0.007 \text{ S/cm}$ in 3% steam + air at 550°C and a conductivity of $\sim 0.015 \text{ S/cm}$ in 50% steam + air at 650°C [103]. The conductivity of BCZYYb4411 in this study is similar to that of Ding's result but different to Choi et al. It is important to note that the conductivity of BCZYYb4411 is less than BCZYYb7111 ($\sim 0.0087 \text{ S/cm}$) as seen in 10% steam + air at 550°C , and from Ding's results in 50% steam + air at 650°C . The high conductivity of BCZYYb7111 is due to the larger amount of Cerium, however this material has been shown to be unstable in CO_2 and H_2S environments [104, 105]. A similar correlation of material quantity can be seen through the study of $\text{BaCe}_{0.9-x}\text{Zr}_x\text{Y}_{0.1}\text{O}_{3-\delta}$ (BCZY), where the chemical stability against CO_2 increases with an increase in zirconium content ($x \geq 0.3$), although at the same time there is a decrease in protonic conductivity [106, 107]. Therefore, the results in this study agree with the lower conductivity but higher stability of BCZYYb4411 compared to BCZYYb7111.

The degradation rate of the DC ASR remains steady for both cases, however, the degradation rate of the BCZYYb4411 is $2.220 \text{ m}\Omega\text{cm}^2/\text{hr}$ larger than the BCZYYb7111. In contrast, the degradation rate of the polarization ASR for BCZYYb7111 is larger than that of BCZYYb4411. Electrolyte material BCZYYb4411 demonstrates better stability in electrode performance as opposed to BCZYYb7111. The stability of the electrolyte performance for BCZYYb4411 is less than BCZYYb7111; however, since the experiment of BCZYYb4411 was cut-short (210 hr), it is difficult to determine the long-term stability.



a)



b)

Figure 4.8: Electrolyte performance in dry O_2 and 10% steam & air, (a) DC & polarization ASR, (b) Polarization ASR

4.5 Oxygen-rich Environment Performance on BCZYYb4411

The importance of this study is to understand the degradation rate of the steam electrode in pure O₂ gas environment, since an operating fuel cell stack has shown less performance degradation in an oxygen-rich environment than in air. Figure 4.8(a) investigates the performance of the cell with electrolyte BCZYYb4411 in two gas environments: 10% steam + air and dry oxygen. The DC ASR change in dry oxygen is -0.254 mΩcm²/hr compared to 4.861 mΩcm²/hr in 10% steam + air. Figure 4.8(b) shows polarization ASR change of 0.266 mΩcm²/hr in dry oxygen, while at 10% steam + air, the change is 0.328 mΩcm²/hr.

The conductivity of BCZYYB4411 in dry O₂ for this study is ~0.0037 S/cm compared to the simulation results by Zhu et al. and measurement results by Somekawa et al. 0.003 S/cm in an oxygen and argon mixed environment [101,108]. This implies that conductivity of BCZYYb4411 is lower in a pure oxygen environment than in humidified air due to the absence of available protons.

The DC ASR performance of BCZYYb4411 in dry oxygen is better than 10% steam + air with a difference of 5.115 mΩcm²/hr. The polarization ASR in dry oxygen has a lower degradation rate than in 10% steam + air. The performance degradation of the electrodes and the electrolyte are slightly less affected in an oxygen-rich environment than in 10% steam + air. This result correlates with the performance degradation of a fuel cell stack in pure oxygen.

4.6 Degradation From Interconnects: Uncoated Untreated and Ce/Co Coated Untreated Interconnects

Metal interconnects are an essential component to proton-conducting ceramic devices for electrical conductivity; however, the available materials for these components have been designed for the use of high temperature oxide-ion conductors. It is imperative to investigate the

compatibility of these ferritic interconnects with proton-conducting materials. In this study, two types of interconnect materials are investigated in 10% steam + air at 550°C.

The performance of the cell with the addition of interconnects is shown in Figure 4.9; the cells in this investigation contain electrolyte BCZYYb7111. Both DC and polarization ASR for the cell with uncoated, untreated Sandvik 441 interconnects have a large increase in values of $0.801 \Omega\text{cm}^2/\text{hr}$ and $1.446 \Omega\text{cm}^2/\text{hr}$, respectively. DC and polarization ASR values of the cell with Ce/Co coated, untreated Sandvik 441 interconnects increases at $0.052 \Omega\text{cm}^2/\text{hr}$ and $0.027 \Omega\text{cm}^2/\text{hr}$, respectively.

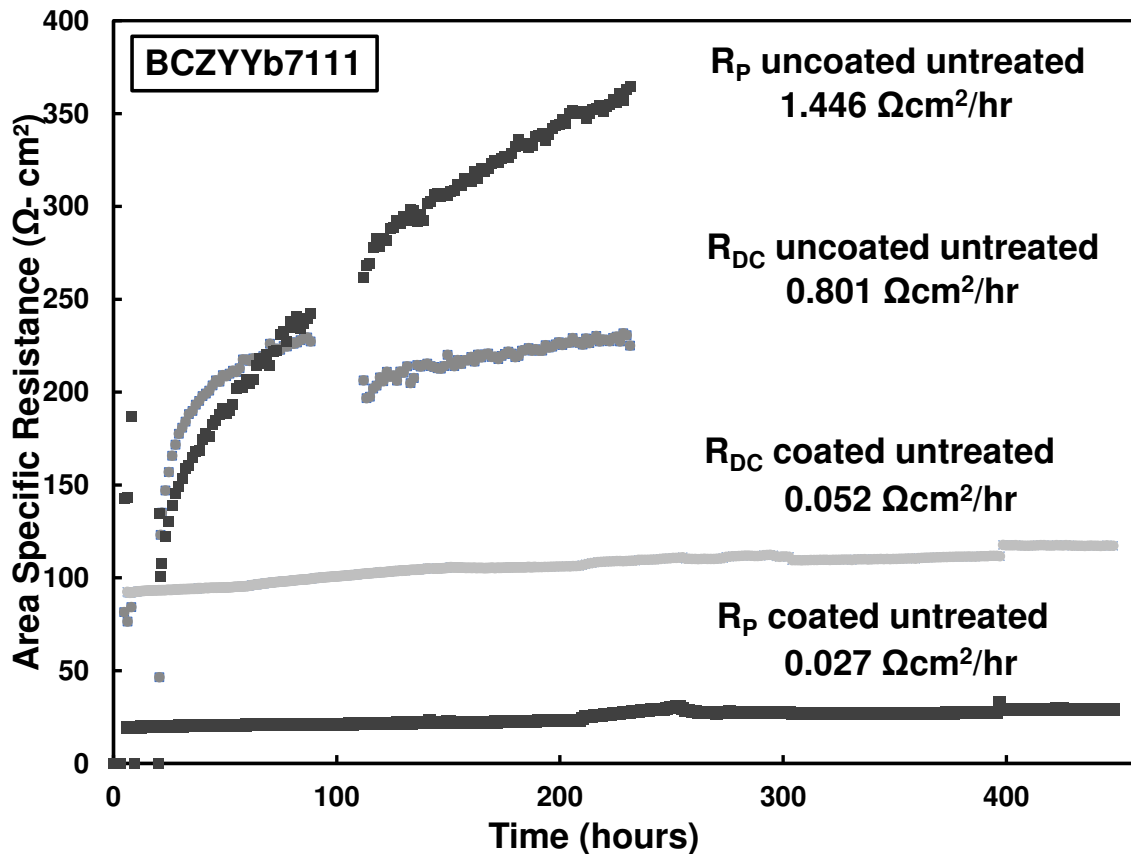


Figure 4.9: Performance comparison of Ce/Co coated and uncoated interconnect

Degradation rates for the cell with uncoated, untreated Sandvik 441 interconnects is comparably larger than that of the cell with Ce/Co coated, untreated interconnects by a DC degradation rate difference of $0.749 \Omega\text{cm}^2/\text{hr}$ and a polarization degradation rate difference of $1.419 \Omega\text{cm}^2/\text{hr}$. Although the cell with Ce/Co coated interconnects has a lower degradation rate

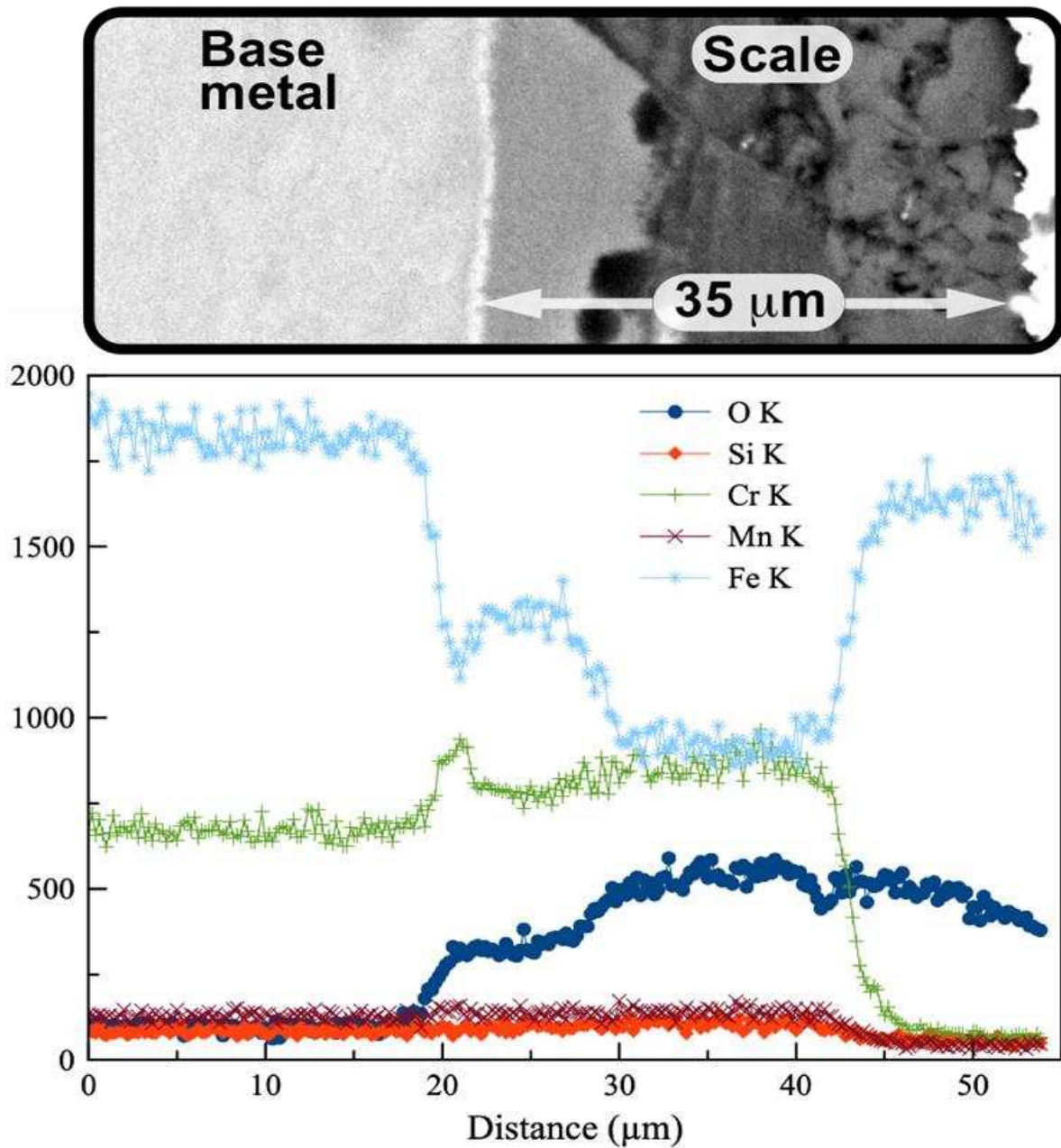


Figure 4.10: EDX analysis of interconnect cross section (unpublished image courtesy to Carolina Herradon Hernandez)

compared to the cell with uncoated interconnects, the values are larger by a magnitude of 10 compared to the other experiments without interconnects.

Grolig et al. demonstrated an increase of polarization ASR of $0.06 \text{ m}\Omega\text{cm}^2/\text{hr}$ in 3% steam + air at 850°C of Ce/Co coated Sandvik 441 [109]. Compared to Figure 4.9, the ASR rate is 450 times smaller, since an operation temperature above 800°C allows for the appropriate formation of protection layers as seen in Figure 3.7.

Hematite (Fe_2O_3) formation is found on the surface of the Sandvik 441 interconnect, adjacent to the surface of contact with the BCZYYb|BCFZY symmetric cell, shown in Figure 4.10. EDX analysis confirms with high contents of iron (Fe) on the scale formed on the exterior of the metal, with the introduction of oxygen (O), while, simultaneously a reduction of chromium (Cr) from that scale. Similarly, Falk-Windisch et al. observed the formation of an iron-rich $(\text{Co,Fe})_3\text{O}_4$ layer under a Co_3O_4 layer on Co coated Sandvik 441[1]. The formation of an iron-rich layer inhibits proper electric conductivity, thus resulting in a drastic increase of ASR values.

4.7 Supplementary Results: NiOBCZYYb|BCZYYb7111 Anode Degradation

The Degradation Test Stand is useful in determining long-term degradation rates. The following experiments in this subsection use electrolyte supported NiBCZYYb anode symmetric cells. The cells were fabricated “in-house” by PhD candidate Long Le. Gold contact paste was used to with gold mesh to ensure proper electrical conductivity using the same preparation methods described in section 3.4. The motivation behind the study of performance degradation of NiOBCZYYb in ammonia is that it is easier to store, transport, and it is more energy efficient and less expensive to produce as opposed to hydrogen.

4.7.1 NiBCZYYb|BCZYYb7111 Anode Symmetric Cell Degradation in Ammonia Environment

NiBCZYYb|BCZYYb7111 anode symmetric cell was investigated in $0.5\text{NH}_3 + 0.5\text{N}_2$ gas environment at 550°C for 1000 hr, as shown in Figure 4.11. The ASR values steadily increase over the first ~ 100 hr, and then the ASR values decrease. The polarization ASR decreases at a rate of $-0.058 \Omega\text{cm}^2$, while the DC ASR decreases at a rate of $-0.011 \Omega\text{cm}^2$. Both ASR values are high compared to values of BCFZY|BCZYYb. The reason for the reduction in resistance is most likely due to the sintering of Ni in the anode.

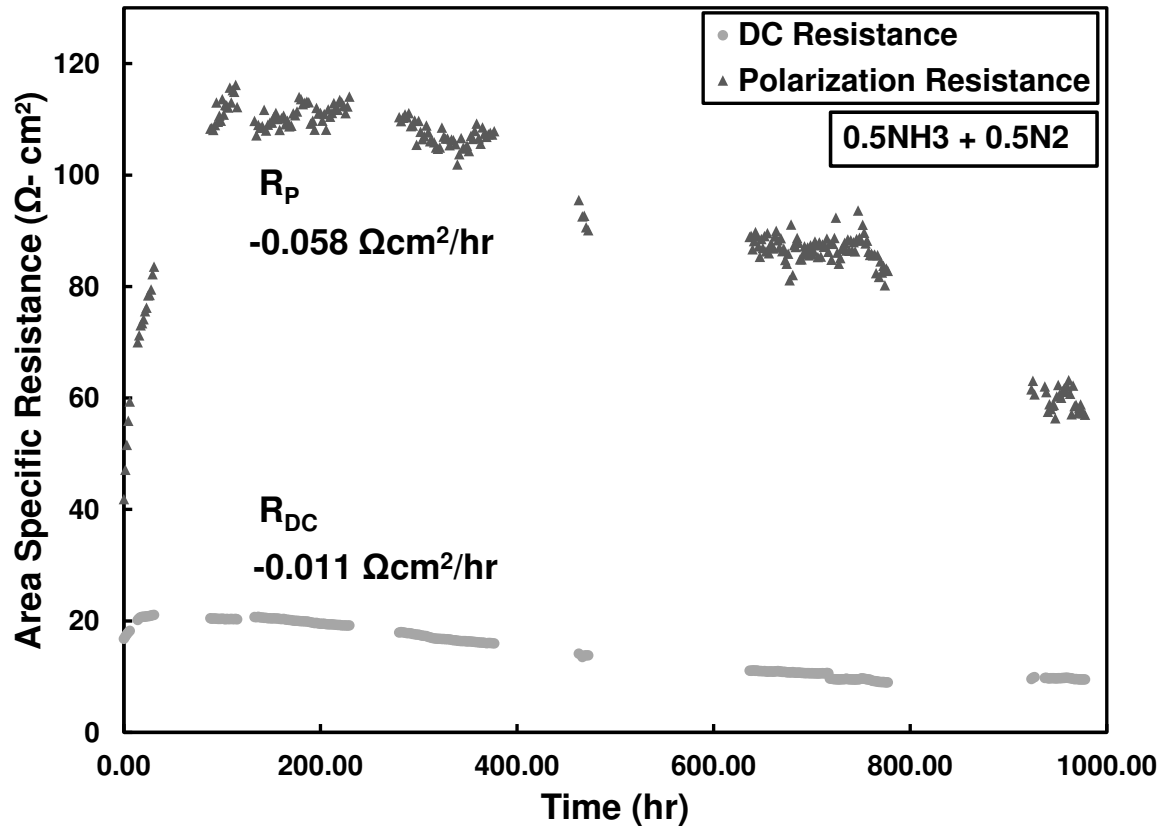


Figure 4.11: NiBCZYYb|BCZYYb7111 symmetric cell in $0.5\text{NH}_3 + 0.5\text{N}_2$ gas environment at 550°C over 1000 hr

4.7.2 NiBCZYYb|BCZYYb7111 Anode Symmetric Cell Degradation and Recovering from H₂ to NH₃ to H₂

NiBCZYYb|BCZYYb7111 symmetric cell performance was investigated in two different fuels, ammonia and hydrogen, at 550°C close to 2000 hr. The fuel type was evenly balanced with nitrogen, and the fuel exchange was done without interacting with the symmetric cell. As shown in Figure 4.12, NiBCZYYb in hydrogen has lower ASR values within ~400 hr compared to that of ammonia in Figure 4.11. The ASR slightly decreases, which may be due to the sintering of Ni. After 1000 hr, the fuel is changed to ammonia, resulting in a sudden increase in polarization ASR, which most likely is due to the reduction of protons. Within ~50 hr, the polarization ASR

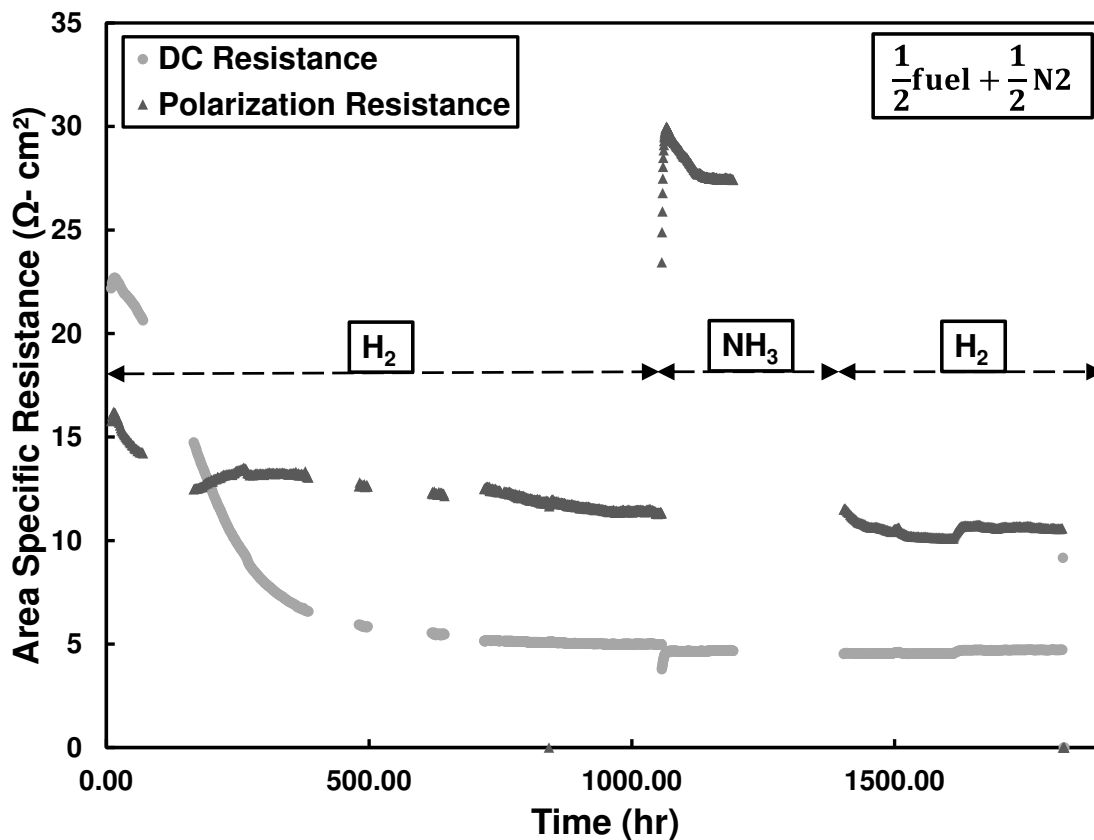


Figure 4.12: NiBCZYYb|BCZYYb7111 symmetric cell in alternating fuel type between ammonia and hydrogen

drops by $2.5 \text{ } \Omega\text{cm}^2$ where it seems to stabilize at $\sim 27.5 \text{ } \Omega\text{cm}^2$; regardless, the polarization ASR doesn't match that of hydrogen fuel. On the other hand, the DC ASR is relatively unchanged since the electric conductivity is independent of proton transport. After $\sim 200 \text{ hr}$, the fuel is switched back to hydrogen, where the ASR values seem to make a remarkable recovery; it's as if the fuel was never switched in the first place. This implies that running NiOBCZYYb in ammonia and or switching between NH_3 and H_2 has no noticeable degradation effects. However, a longer-term experiment is required to ensure this claim.

CHAPTER 5

CONCLUSIONS AND FUTURE WORK

This section is divided into conclusions drawn from each experiment on proton-conducting ceramic symmetric cells and validation of the test stand used. The future work section is included in this Chapter.

5.1 Validation of Degradation Test Stand with YSZ|LSM Symmetric Cells

According to the ASR values from the three cells, the DTS shows acceptable repeatability. As mentioned, all polarization ASR agree with the range shown by Østergård et al. [93]. The large percent difference for polarization ASR values (14.89%) could be due to the difficulty in repeatability when fabricating the electrodes on the electrolyte. The performance of the DC ASR values are within less than 6% difference, of which two cells showed the same resistance value. The resistivity and conductivity values are within less than 0.75% difference for all cells, and these values are similar to those found in literature. Through these verification tests, the repeatability and accuracy of the Degradation Test Stand for cell degradation performance in proton-conducting ceramics is acceptable. The Degradation Test Stand can produce reliable characterize and measure electrical conductive properties of components of electrochemical devices over long-term experimentation.

Supplementary experiments validated the DTS in repeatability and reliability to a level of acceptance. These experiments demonstrate the significance of contact paste for the reduction in ASR in the cell components.

5.2 Performance Characterization of FuelCell Energy's Proprietary Contact Paste at Intermediate Temperatures

FCE contact paste shows higher performance at 400°C for DC ASR and polarization ASR. The conductivity properties of FCE contact paste and Pt contact paste are similar. Through this characterization experiment, the Arrhenius plot of the conductivity of BCZYYb7111 showed comparable values to literature results. Both types of contact paste are acceptable for use in proton-conducting devices, as the activation energy for both types of contact paste on BCZYYb7111 showed agreeable values for proton-conducting ceramic materials.

5.3 Humidity Stability with BCZYYb7111: 10% Steam VS 50% Steam

High levels of humidity drastically affect the polarization ASR of BCZYYb|BCFZY symmetric cells, while the DC ASR of the cells are not as affected. This means that the BCFZY electrodes are sensitive to high humidity levels, while the electrolyte is not as affected. BCZYYb|BCFZY symmetric cells are stable at humidity levels of 10% and less; therefore, the following experiments have a gas environment of air + 10% steam, with the exception of pure oxygen.

5.4 Electrolyte Stability: BCZYYb7111 and BCZYYb4411

Electrolyte BCZYYb4411 shows slighter stability than BCZYYb7111 in 10% steam environment. The change in polarization ASR implies that the electrolyte|electrode interface is more stable with BCZYYb4411 than BCZYYb7111, since the electrodes for both experiments are the same. Electrolyte BCZYYb4411 may have a favorable effective compatibility with the BCFZY electrode. However, electrical conductivity is lower for BCZYYb4411, due to a reduction in cerium.

5.5 BCZYYb4411 Performance in Pure Oxygen

BCZYYb|BCFZY symmetric cells are slightly more stable in pure oxygen than in air + 10% steam. There is a reduction in electric conductivity in a pure oxygen operating gas environment. The conductivity of BCZYYb4411 is lower in a pure oxygen environment than in a humidified one, due to the lack of availability of transport of proton. The slower degradation of BCZYYb4411 in pure oxygen as opposed to humidified air agrees with fuel cell stack operation.

5.6 Degradation from Interconnects

Introduction of uncoated, untreated interconnects drastically degrades BCZYYb|BCFZY symmetric cells. At PCFC operating temperatures, interconnects form a hematite layer (Fe_2O_3) impeding proper electric conductivity, in contrast to the formation of electrically conductive $(\text{Cr},\text{Mn})_3\text{O}_4$ scale, that forms at SOFC operating temperatures. A Ce/Co coated interconnect can decrease the degradation rate at 550°C , but the performance degradation is still worth considering.

5.7 Future Work

With the rising interest in PCFCs, much research is required to understand this new technology for renewable and sustainable alternatives in energy production and storage. Each study in this thesis is extendable to fully investigate performance degradation of PCFCs:

- A complete study of incrementing steam levels: 0% steam, 3% steam and 25% steam
- A study of varied gas environments, since adsorption of gas can affect the chemical nature of material sites, corrosion, surface segregation and phase formation: steam & oxygen, hydrogen, and CO_2 [8]

- A thorough investigation of SOFC interconnect metals, new metals, and treatment of each metal: uncoated & treated Sandvik 441, Ce/Co coated & treated Sandvik 441, Crofer, Plansee, and new alloy metals
- A study of interconnects in this thesis was completed using BCZYYb7111; this investigation should be repeated on BCZYYb4411, since this electrolyte shows better stability
- Some experiments were prematurely stopped; in order to avoid extrapolation of measurements of degradation rates over 1000 hours, tests should be repeated for 1000 hours
- Investigation of other fuel cell components: execution of additional experiments on anode symmetric cells

REFERENCES CITED

- [1] Falk-Windisch, H., Claquesin, J., Sattari, M., Svensson, J.-E., & Froitzheim, J. (2017). Co- and Ce/Co-coated ferritic stainless steel as interconnect material for Intermediate Temperature Solid Oxide Fuel Cells. *Journal of Power Sources*, *343*, 1–10. doi: 10.1016/j.jpowsour.2017.01.045
- [2] Kidner, N. J., Ibanez, S., Seabaugh, M. M., & Swartz, S. (2017). Advances in Low Temperature Coatings for Solid Oxide Fuel Cell Components. *ECS Transactions*, *78*(1), 1897–1901. doi: 10.1149/07801.1897ecst
- [3] Bi, L., Boulfrad, S., & Traversa, E. (2014). Steam electrolysis by solid oxide electrolysis cells (SOECs) with proton-conducting oxides. *Chem. Soc. Rev.*, *43*(24), 8255–8270. doi: 10.1039/c4cs00194j
- [4] Wang, R., Würth, M., Pal, U. B., Gopalan, S., & Basu, S. N. (2017). Roles of humidity and cathodic current in chromium poisoning of Sr-doped LaMnO₃-based cathodes in solid oxide fuel cells. *Journal of Power Sources*, *360*, 87–97. doi: 10.1016/j.jpowsour.2017.06.005
- [5] Yang, Z., Guo, M., Wang, N., Ma, C., Wang, J., & Han, M. (2017). A short review of cathode poisoning and corrosion in solid oxide fuel cell. *International Journal of Hydrogen Energy*, *42*(39), 24948–24959. doi: 10.1016/j.ijhydene.2017.08.057
- [6] Xiong, C., Li, W., Ding, D., Pu, J., Chi, B., & Li, J. (2016). Chromium poisoning effect on strontium-doped samarium manganite for solid oxide fuel cell. *International Journal of Hydrogen Energy*, *41*(45), 20660–20669. doi: 10.1016/j.ijhydene.2016.07.061
- [7] Falk-Windisch, H., Claquesin, J., Svensson, J.-E., & Froitzheim, J. (2017). The Effect of Metallic Co-Coating Thickness on Ferritic Stainless Steels Intended for Use as Interconnect Material in Intermediate Temperature Solid Oxide Fuel Cells. *Oxidation of Metals*, *89*(1-2), 233–250. doi: 10.1007/s11085-017-9782-9
- [8] Duan, C., Kee, R., Zhu, H., Sullivan, N., Zhu, L., Bian, L., ... O'Hayre, R. (2019). Highly efficient reversible protonic ceramic electrochemical cells for power generation and fuel production. *Nature Energy*, *4*(3), 230–240. doi: 10.1038/s41560-019-0333-2
- [9] Pivovar, B., Rustagi, N., & Satyapal, S. (2018). Hydrogen at Scale (H₂@Scale): Key to a Clean, Economic, and Sustainable Energy System. *The Electrochemical Society Interface*, *27*(1), 47–52. doi: 10.1149/2.f04181if
- [10] Arshad, A., Ali, H. M., Habib, A., Bashir, M. A., Jabbar, M., & Yan, Y. (2019). Energy and exergy analysis of fuel cells: A review. *Thermal Science and Engineering Progress*, *9*, 308–321. doi: 10.1016/j.tsep.2018.12.008
- [11] Key, C., Eziashi, J., Froitzheim, J., Amendola, R., Smith, R., & Gannon, P. (2014). Methods to Quantify Reactive Chromium Vaporization from Solid Oxide Fuel Cell Interconnects. *Journal of The Electrochemical Society*, *161*(9), C373–C381. doi: 10.1149/2.0041409jes

- [12] Goebel, C., Berger, R., Lundberg, M. W., Westlinder, J., Svensson, J.-E., & Froitzheim, J. (2017). Long Term (4 Years) Performance of Co/Ce Coated 441 for SOFC Interconnect Applications. *ECS Transactions*, 78(1), 1675–1679. doi: 10.1149/07801.1675ecst
- [13] Iwahara, H., Esaka, T., Uchida, H., & Maeda, N. (1981). Proton conduction in sintered oxides and its application to steam electrolysis for hydrogen production. *Solid State Ionics*, 3-4, 359–363. doi: 10.1016/0167-2738(81)90113-2
- [14] Hossain, S., Abdalla, A. M., Jamain, S. N. B., Zaini, J. H., & Azad, A. K. (2017). A review on proton conducting electrolytes for clean energy and intermediate temperature-solid oxide fuel cells. *Renewable and Sustainable Energy Reviews*, 79, 750–764. doi: 10.1016/j.rser.2017.05.147
- [15] Lyu, Z., Li, H., & Han, M. (2019). Electrochemical properties and thermal neutral state of solid oxide fuel cells with direct internal reforming of methane. *International Journal of Hydrogen Energy*, 44(23), 12151–12162. doi: 10.1016/j.ijhydene.2019.03.048
- [16] Yang, Z., Yang, C., Xiong, B., Han, M., & Chen, F. (2011). BaCo_{0.7}Fe_{0.2}Nb_{0.1}O_{3-δ} as cathode material for intermediate temperature solid oxide fuel cells. *Journal of Power Sources*, 196(22), 9164–9168. doi: 10.1016/j.jpowsour.2011.06.096
- [17] Yang, Z.-B., Han, M.-F., Zhu, P., Zhao, F., & Chen, F. (2011). Ba_{1-x}Co_{0.9-y}Fe_yNb_{0.1}O_{3-δ} (x = 0–0.15, y = 0–0.9) as cathode materials for solid oxide fuel cells. *International Journal of Hydrogen Energy*, 36(15), 9162–9168. doi: 10.1016/j.ijhydene.2011.04.045
- [18] Yang, Z., Liu, Y., Zhu, T., Chen, Y., Han, M., & Jin, C. (2016). Mechanism analysis of CO₂ corrosion on Ba_{0.9}Co_{0.7}Fe_{0.2}Nb_{0.1}O_{3-δ} cathode. *International Journal of Hydrogen Energy*, 41(3), 1997–2001. doi: 10.1016/j.ijhydene.2015.11.095
- [19] Yang, Z., Yang, C., Jin, C., Han, M., & Chen, F. (2011). Ba_{0.9}Co_{0.7}Fe_{0.2}Nb_{0.1}O_{3-δ} as cathode material for intermediate temperature solid oxide fuel cells. *Electrochemistry Communications*, 13(8), 882–885. doi: 10.1016/j.elecom.2011.05.029
- [20] Chen, Z., Ran, R., Zhou, W., Shao, Z., & Liu, S. (2007). Assessment of Ba_{0.5}Sr_{0.5}Co_{1-y}Fe_yO_{3-δ} (y=0.0–1.0) for prospective application as cathode for IT-SOFCs or oxygen permeating membrane. *Electrochimica Acta*, 52(25), 7343–7351. doi: 10.1016/j.electacta.2007.06.010
- [21] Yan, A., Cheng, M., Dong, Y., Yang, W., Maragou, V., Song, S., & Tsiakaras, P. (2006). Investigation of a Ba_{0.5}Sr_{0.5}Co_{0.8}Fe_{0.2}O_{3-δ} based cathode IT-SOFC. *Applied Catalysis B: Environmental*, 66(1-2), 64–71. doi: 10.1016/j.apcatb.2006.02.021
- [22] Yi, J., Schroeder, M., & Martin, M. (2013). CO₂-Tolerant and Cobalt-Free SrFe_{0.8}Nb_{0.2}O_{3-δ} Perovskite Membrane for Oxygen Separation. *Chemistry of Materials*, 25(6), 815–817. doi: 10.1021/cm303666v

- [23] Zhang, Z., Chen, D., Dong, F., Xu, X., Hao, Y., & Shao, Z. (2016). Understanding the doping effect toward the design of CO₂-tolerant perovskite membranes with enhanced oxygen permeability. *Journal of Membrane Science*, 519, 11–21. doi: 10.1016/j.memsci.2016.07.043
- [24] Zhang, Z., Chen, D., Dong, F., & Shao, Z. (2015). Efficient and CO₂-tolerant oxygen transport membranes prepared from high-valence B-site substituted cobalt-free SrFeO_{3-δ}. *Journal of Membrane Science*, 495, 187–197. doi: 10.1016/j.memsci.2015.08.032
- [25] Xu, D., Dong, F., Chen, Y., Zhao, B., Liu, S., Tade, M. O., & Shao, Z. (2014). Cobalt-free niobium-doped barium ferrite as potential materials of dense ceramic membranes for oxygen separation. *Journal of Membrane Science*, 455, 75–82. doi: 10.1016/j.memsci.2013.12.030
- [26] Yang, Z., Liu, Y., Chen, Y., Wang, J., Han, Z., Zhu, Y., & Han, M. (2017). Effects of humidity on Ba_{0.9}Co_{0.7}Fe_{0.2}Nb_{0.1}O_{3-δ} cathode performance and durability of Solid Oxide Fuel Cells. *International Journal of Hydrogen Energy*, 42(10), 6997–7002. doi: 10.1016/j.ijhydene.2016.11.045
- [27] Lin, Y., Zhou, W., Sunarso, J., Ran, R., & Shao, Z. (2012). Characterization and evaluation of BaCo_{0.7}Fe_{0.2}Nb_{0.1}O_{3-δ} as a cathode for proton-conducting solid oxide fuel cells. *International Journal of Hydrogen Energy*, 37(1), 484–497. doi: 10.1016/j.ijhydene.2011.09.010
- [28] Jiang, S. P., & Chen, X. (2014). ChemInform Abstract: Chromium Deposition and Poisoning of Cathodes of Solid Oxide Fuel Cells - A Review. *ChemInform*, 45(14), 505–531. doi: 10.1002/chin.201414233
- [29] Aphale, A., Liang, C., Hu, B., & Singh, P. (2017). Cathode Degradation From Airborne Contaminants in Solid Oxide Fuel Cells. *Solid Oxide Fuel Cell Lifetime and Reliability*, 101–119. doi: 10.1016/b978-0-08-101102-7.00006-4
- [30] Jiang, S., Zhang, J., & Zheng, X. (2002). A comparative investigation of chromium deposition at air electrodes of solid oxide fuel cells. *Journal of the European Ceramic Society*, 22(3), 361–373. doi: 10.1016/s0955-2219(01)00280-1
- [31] Schrödl, N., Bucher, E., Egger, A., Kreiml, P., Teichert, C., Höschen, T., & Sitte, W. (2015). Long-term stability of the IT-SOFC cathode materials La_{0.6}Sr_{0.4}CoO_{3-δ} and La₂NiO_{4 δ} against combined chromium and silicon poisoning. *Solid State Ionics*, 276, 62–71. doi: 10.1016/j.ssi.2015.03.035
- [32] Viitanen, M. M., Welzenis, R. G., Brongersma, H. H., & Berkel, F. P. F. (2002). Silica poisoning of oxygen membranes. *Solid State Ionics*, 150(3-4), 223–228. doi: 10.1016/s0167-2738(02)00455-1
- [33] Zhao, L., Perry, N. H., Daio, T., Sasaki, K., & Bishop, S. R. (2015). Improving the Si Impurity Tolerance of Pr_{0.1}Ce_{0.9}O_{2-δ} SOFC Electrodes with Reactive Surface Additives. *Chemistry of Materials*, 27(8), 3065–3070. doi: 10.1021/acs.chemmater.5b00501

- [34] Backhaus-Ricoult, M. (2008). SOFC – A playground for solid state chemistry. *Solid State Sciences*, 10(6), 670–688. doi: 10.1016/j.solidstatedciences.2007.11.021
- [35] Bucher, E., Sitte, W., Klauser, F., & Bertel, E. (2012). Impact of humid atmospheres on oxygen exchange properties, surface-near elemental composition, and surface morphology of $\text{La}_{0.6}\text{Sr}_{0.4}\text{CoO}_{3-\delta}$. *Solid State Ionics*, 208, 43–51. doi: 10.1016/j.ssi.2011.12.005
- [36] Bucher, E., & Sitte, W. (2004). Defect Chemical Modeling of $(\text{La}, \text{Sr})(\text{Co}, \text{Fe})\text{O}_{3-\delta}$. *Journal of Electroceramics*, 13(1-3), 779–784. doi: 10.1007/s10832-004-5192-x
- [37] Bucher, E., & Sitte, W. (2011). Long-term stability of the oxygen exchange properties of $(\text{La}, \text{Sr})_{1-z}(\text{Co}, \text{Fe})\text{O}_{3-\delta}$ in dry and wet atmospheres. *Solid State Ionics*, 192(1), 480–482. doi: 10.1016/j.ssi.2010.01.006
- [38] Porrás-Vázquez, J. M., Smith, R., & Slater, P. R. (2014). Investigation into the effect of Si doping on the cell symmetry and performance of $\text{Sr}_{1-y}\text{Ca}_y\text{FeO}_{3-\delta}$ SOFC cathode materials. *Journal of Solid State Chemistry*, 213, 132–137. doi: 10.1016/j.jssc.2014.02.027
- [39] Porrás-Vázquez, J. M., & Slater, P. R. (2012). Synthesis and Characterization of Oxyanion-Doped Cobalt Containing Perovskites. *Fuel Cells*, 12(6), 1056–1063. doi: 10.1002/fuce.201200081
- [40] Kim, J., Sengodan, S., Kim, S., Kwon, O., Bu, Y., & Kim, G. (2019). Proton conducting oxides: A review of materials and applications for renewable energy conversion and storage. *Renewable and Sustainable Energy Reviews*, 109, 606–618. doi: 10.1016/j.rser.2019.04.042
- [41] Atkinson, A., Barnett, S., Gorte, R. J., Irvine, J. T. S., Mcevoy, A. J., Mogensen, M., ... Vohs, J. (2004). Advanced anodes for high-temperature fuel cells. *Nature Materials*, 3(1), 17–27. doi: 10.1038/nmat1040
- [42] Khan, M. S., Lee, S.-B., Song, R.-H., Lee, J.-W., Lim, T.-H., & Park, S.-J. (2016). Fundamental mechanisms involved in the degradation of nickel–yttria stabilized zirconia (Ni–YSZ) anode during solid oxide fuel cells operation: A review. *Ceramics International*, 42(1), 35–48. doi: 10.1016/j.ceramint.2015.09.006
- [43] Iwata, T. (1996). Characterization of Ni-YSZ Anode Degradation for Substrate-Type Solid Oxide Fuel Cells. *Journal of The Electrochemical Society*, 143(5), 1521–1525. doi: 10.1149/1.1836673
- [44] Simwonis, D. (2000). Nickel coarsening in annealed Ni/8YSZ anode substrates for solid oxide fuel cells. *Solid State Ionics*, 132(3-4), 241–251. doi: 10.1016/s0167-2738(00)00650-0
- [45] Hagen, A., Barfod, R., Hendriksen, P. V., Liu, Y.-L., & Ramousse, S. (2006). Degradation of Anode Supported SOFCs as a Function of Temperature and Current Load. *Journal of The Electrochemical Society*, 153(6), A1165–A1171. doi: 10.1149/1.2193400

- [46] Holzer, L., Iwanschitz, B., Hocker, T., Münch, B., Prestat, M., Wiedenmann, D., ... Graule, T. (2011). Microstructure degradation of cermet anodes for solid oxide fuel cells: Quantification of nickel grain growth in dry and in humid atmospheres. *Journal of Power Sources*, 196(3), 1279–1294. doi: 10.1016/j.jpowsour.2010.08.017
- [47] Jiao, Z., Takagi, N., Shikazono, N., & Kasagi, N. (2011). Study on local morphological changes of nickel in solid oxide fuel cell anode using porous Ni pellet electrode. *Journal of Power Sources*, 196(3), 1019–1029. doi: 10.1016/j.jpowsour.2010.08.047
- [48] Matsui, T., Kishida, R., Muroyama, H., & Eguchi, K. (2012). Comparative Study on Performance Stability of Ni–Oxide Cermet Anodes under Humidified Atmospheres in Solid Oxide Fuel Cells. *Journal of The Electrochemical Society*, 159(8), F456–F460. doi: 10.1149/2.053208jes
- [49] Li, T. S., & Wang, W. G. (2011). The Mechanism of H₂S Poisoning Ni/YSZ Electrode Studied by Impedance Spectroscopy. *Electrochemical and Solid-State Letters*, 14(3), B35–B37. doi: 10.1149/1.3526134
- [50] Matsuzaki, Y., & Yasuda, I. (2000). The poisoning effect of sulfur-containing impurity gas on a SOFC anode: Part I. Dependence on temperature, time, and impurity concentration. *Solid State Ionics*, 132(3-4), 261–269. doi: 10.1016/s0167-2738(00)00653-6
- [51] Gong, M., Liu, X., Trembly, J., & Johnson, C. (2007). Sulfur-tolerant anode materials for solid oxide fuel cell application. *Journal of Power Sources*, 168(2), 289–298. doi: 10.1016/j.jpowsour.2007.03.026
- [52] Dong, J., Cheng, Z., Zha, S., & Liu, M. (2006). Identification of nickel sulfides on Ni–YSZ cermet exposed to H₂ fuel containing H₂S using Raman spectroscopy. *Journal of Power Sources*, 156(2), 461–465. doi: 10.1016/j.jpowsour.2005.06.016
- [53] Kromp, A., Dierickx, S., Leonide André, Weber André, & Ivers-Tiffée Ellen. (2012). Electrochemical Analysis of Sulphur-Poisoning in Anode-Supported SOFCs under Reformate Operation, 41, 161–169. doi: 10.1149/1.3702423
- [54] Rasmussen, J. F., & Hagen, A. (2009). The effect of H₂S on the performance of Ni–YSZ anodes in solid oxide fuel cells. *Journal of Power Sources*, 191(2), 534–541. doi: 10.1016/j.jpowsour.2009.02.001
- [55] Peterson, D. R., & Winnick, J. (1998). Utilization of Hydrogen Sulfide in an Intermediate-Temperature Ceria-Based Solid Oxide Fuel Cell. *Journal of The Electrochemical Society*, 145(5), 1449–1454. doi: 10.1149/1.1838503
- [56] Sreedhar, I., Agarwal, B., Goyal, P., & Singh, S. A. (2019). Recent advances in material and performance aspects of solid oxide fuel cells. *Journal of Electroanalytical Chemistry*, 848. doi: 10.1016/j.jelechem.2019.113315

- [57] Cheng, Z., & Liu, M. (2007). Characterization of sulfur poisoning of Ni–YSZ anodes for solid oxide fuel cells using in situ Raman microspectroscopy. *Solid State Ionics*, 178(13-14), 925–935. doi: 10.1016/j.ssi.2007.04.004
- [58] Lanzini, A., Leone, P., Guerra, C., Smeacetto, F., Brandon, N., & Santarelli, M. (2013). Durability of anode supported Solid Oxides Fuel Cells (SOFC) under direct dry-reforming of methane. *Chemical Engineering Journal*, 220, 254–263. doi: 10.1016/j.cej.2013.01.003
- [59] Froitzheim, J., Ravash, H., Larsson, E., Johansson, L. G., & Svensson, J. E. (2010). Investigation of Chromium Volatilization from FeCr Interconnects by a Denuder Technique. *Journal of The Electrochemical Society*, 157(9), B1295–B1300. doi: 10.1149/1.3462987
- [60] Stanislawski, M., Froitzheim, J., Niewolak, L., Quadackers, W., Hilpert, K., Markus, T., & Singheiser, L. (2007). Reduction of chromium vaporization from SOFC interconnectors by highly effective coatings. *Journal of Power Sources*, 164(2), 578–589. doi: 10.1016/j.jpowsour.2006.08.013
- [61] Windisch, H. F., Froitzheim, J., & Svensson, J.-E. (2013). Influence of Chromium Evaporation and Oxidation on Interconnect Steels at 650-850 C. *ECS Transactions*, 57(1), 2225–2233. doi: 10.1149/05701.2225ecst
- [62] Froitzheim, J., Meier, G., Niewolak, L., Ennis, P., Hattendorf, H., Singheiser, L., & Quadackers, W. (2008). Development of high strength ferritic steel for interconnect application in SOFCs. *Journal of Power Sources*, 178(1), 163–173. doi: 10.1016/j.jpowsour.2007.12.028
- [63] Casteel, M., Lewis, D., Willson, P., & Alinger, M. (2012). Ionic Conductivity Method for measuring vaporized chromium species from solid oxide fuel cell interconnects. *International Journal of Hydrogen Energy*, 37(8), 6818–6829. doi: 10.1016/j.ijhydene.2012.01.016
- [64] Grolig, J., Froitzheim, J., & Svensson, J.-E. (2014). Coated stainless steel 441 as interconnect material for solid oxide fuel cells: Oxidation performance and chromium evaporation. *Journal of Power Sources*, 248, 1007–1013. doi: 10.1016/j.jpowsour.2013.08.089
- [65] Minh, N. Q. (1993). Ceramic Fuel Cells. *Journal of the American Ceramic Society*, 76(3), 563–588. doi: 10.1111/j.1151-2916.1993.tb03645.x
- [66] Suzuki, T., Hasan, Z., Funahashi, Y., Yamaguchi, T., Fujishiro, Y., & Awano, M. (2009). Impact of Anode Microstructure on Solid Oxide Fuel Cells. *Science*, 325(5942), 852–855. doi: 10.1126/science.1176404
- [67] Fabbri, E., Pergolesi, D., & Traversa, E. (2010). Materials challenges toward proton-conducting oxide fuel cells: a critical review. *Chemical Society Reviews*, 39(11), 4355–4369. doi: 10.1039/b902343g

- [68] Zuo, C., Zha, S., Liu, M., Hatano, M., & Uchiyama, M. (2006). Ba(Zr_{0.1}Ce_{0.7}Y_{0.2})O_{3-δ} as an Electrolyte for Low-Temperature Solid-Oxide Fuel Cells. *Advanced Materials*, 18(24), 3318–3320. doi: 10.1002/adma.200601366
- [69] Bi, L., Fabbri, E., Sun, Z., & Traversa, E. (2011). BaZr_{0.8}Y_{0.2}O_{3-δ}-NiO Composite Anodic Powders for Proton-Conducting SOFCs Prepared by a Combustion Method. *Journal of The Electrochemical Society*, 158(7), B797–B803. doi: 10.1149/1.3591040
- [70] Ni, M., Leung, M. K., & Leung, D. Y. (2008). Electrochemical modeling of hydrogen production by proton-conducting solid oxide steam electrolyzer. *International Journal of Hydrogen Energy*, 33(15), 4040–4047. doi: 10.1016/j.ijhydene.2008.05.065
- [71] Eguchi, K., Hatagishi, T., & Arai, H. (1996). Power generation and steam electrolysis characteristics of an electrochemical cell with a zirconia- or ceria-based electrolyte. *Solid State Ionics*, 86-88, 1245–1249. doi: 10.1016/0167-2738(96)00295-0
- [72] Matsui, T., Kishida, R., Kim, J.-Y., Muroyama, H., & Eguchi, K. (2010). Performance Deterioration of Ni–YSZ Anode Induced by Electrochemically Generated Steam in Solid Oxide Fuel Cells. *Journal of The Electrochemical Society*, 157(5), B776–B781. doi: 10.1149/1.3336830
- [73] Yang, X., & Irvine, J. T. S. (2008). (La_{0.75}Sr_{0.25})_{0.95}Mn_{0.5}Cr_{0.5}O₃ as the cathode of solid oxide electrolysis cells for high temperature hydrogen production from steam. *Journal of Materials Chemistry*, 18(20), 2349–2354. doi: 10.1039/b800163d
- [74] O'Brien, J. E., Stoots, C. M., Herring, J. S., Lessing, P. A., Hartvigsen, J. J., & Elangovan, S. (2005). Performance Measurements of Solid-Oxide Electrolysis Cells for Hydrogen Production. *Journal of Fuel Cell Science and Technology*, 2(3), 156–163. doi: 10.1115/1.1895946
- [75] Medvedev, D. (2019). Trends in research and development of protonic ceramic electrolysis cells. *International Journal of Hydrogen Energy*, 44(49), 26711–26740. doi: 10.1016/j.ijhydene.2019.08.130
- [76] Dailly, J., Ancelin, M., & Marrony, M. (2017). Long term testing of BCZY-based protonic ceramic fuel cell PCFC: Micro-generation profile and reversible production of hydrogen and electricity. *Solid State Ionics*, 306, 69–75. doi: 10.1016/j.ssi.2017.03.002
- [77] Dunyushkina, L. A., & Adler, S. B. (2005). Influence of Electrolyte Surface Planarization on the Performance of the Porous SOFC Cathodes. *Journal of The Electrochemical Society*, 152(10), A2040–A2045. doi: 10.1149/1.2032448
- [78] Hildenbrand, N., Boukamp, B. A., Nammensma, P., & Blank, D. H. A. (2011). Improved cathode/electrolyte interface of SOFC. *Solid State Ionics*, 192(1), 12–15. doi: 10.1016/j.ssi.2010.01.028
- [79] Talebi, T., Haji, M., & Raissi, B. (2010). Effect of sintering temperature on the microstructure, roughness and electrochemical impedance of electrophoretically deposited YSZ electrolyte for

SOFCs. *International Journal of Hydrogen Energy*, 35(17), 9420–9426. doi: 10.1016/j.ijhydene.2010.05.079

- [80] Thampi, K. R., McEvoy, A. J., & Herle, J. V. (1995). Electrocatalysis in Solid Oxide Fuel Cell Electrode Domains. *Journal of The Electrochemical Society*, 142(2), 506–513. doi: 10.1149/1.2044089
- [81] Zhu, J., & Ghezal-Ayagh, H. (2017). Cathode-side electrical contact and contact materials for solid oxide fuel cell stacking: A review. *International Journal of Hydrogen Energy*, 42(38), 24278–24300. doi: 10.1016/j.ijhydene.2017.08.005
- [82] Duan, C., Tong, J., Shang, M., Nikodemski, S., Sanders, M., Ricote, S., Almansoori, A., Ohayre, R. (2015). Readily processed protonic ceramic fuel cells with high performance at low temperatures. *Science*, 349(6254), 1321–1326. doi: 10.1126/science.aab3987
- [83] Duan, C., Hook, D., Chen, Y., Tong, J., & Ohayre, R. (2017). Zr and Y co-doped perovskite as a stable, high performance cathode for solid oxide fuel cells operating below 500 °C. *Energy & Environmental Science*, 10(1), 176–182. doi: 10.1039/c6ee01915c
- [84] Goebel, C., Alnegren, P., Faust, R. L., Svensson, J.-E., & Froitzheim, J. (2017). Influence of Pre-Oxidation on Dual Atmosphere Effect on AISI 441 Interconnects for Solid Oxide Fuel Cell Applications. *ECS Transactions*, 78(1), 1559–1563. doi: 10.1149/07801.1559ecst
- [85] Comminges, C., Fu, Q., Zahid, M., Steiner, N. Y., & Bucheli, O. (2012). Monitoring the degradation of a solid oxide fuel cell stack during 10,000h via electrochemical impedance spectroscopy. *Electrochimica Acta*, 59, 367–375. doi: 10.1016/j.electacta.2011.10.080
- [86] Barfod, R., Mogensen, M., Klemenso/Trine, Hagen, A., Liu, Y.-L., & Hendriksen, P. V. (2007). Detailed Characterization of Anode-Supported SOFCs by Impedance Spectroscopy. *Journal of The Electrochemical Society*, 154(4), B371–B378. doi: 10.1149/1.2433311
- [87] Huang, Q.-A., Hui, R., Wang, B., & Zhang, J. (2007). A review of AC impedance modeling and validation in SOFC diagnosis. *Electrochimica Acta*, 52(28), 8144–8164. doi: 10.1016/j.electacta.2007.05.071
- [88] Onishi, T., Han, D., Noda, Y., Hatada, N., Majima, M., & Uda, T. (2018). Evaluation of performance and durability of Ni-BZY cermet electrodes with BZY electrolyte. *Solid State Ionics*, 317, 127–135. doi: 10.1016/j.ssi.2018.01.015
- [89] Jasinski, P., Suzuki, T., Dogan, F., & Anderson, H. U. (2004). Impedance spectroscopy of single chamber SOFC. *Solid State Ionics*, 175(1-4), 35–38. doi: 10.1016/j.ssi.2004.09.041
- [90] Primdahl, S., & Mogensen, M. (1999). Gas Diffusion Impedance in Characterization of Solid Oxide Fuel Cell Anodes. *Journal of The Electrochemical Society*, 146(8), 2827–2833. doi: 10.1149/1.1392015

- [91] Wagner, N., Schnurnberger, W., Müller, B., & Lang, M. (1998). Electrochemical impedance spectra of solid-oxide fuel cells and polymer membrane fuel cells. *Electrochimica Acta*, 43(24), 3785–3793. doi: 10.1016/s0013-4686(98)00138-8
- [92] Ploner, A., Hagen, A., & Hauch, A. (2018). Classical statistical methodology for accelerated testing of Solid Oxide Fuel Cells. *Journal of Power Sources*, 395, 379–385. doi: 10.1016/j.jpowsour.2018.05.034
- [93] Østergård, M., Clausen, C., Bagger, C., & Mogensen, M. (1995). Manganite-zirconia composite cathodes for SOFC: Influence of structure and composition. *Electrochimica Acta*, 40(12), 1971–1981. doi: 10.1016/0013-4686(94)00332-u
- [94] Zhu, L., Zhang, L., & Virkar, A. V. (2015). Measurement of Ionic and Electronic Conductivities of Yttria-Stabilized Zirconia by an Embedded Electrode Method. *Journal of The Electrochemical Society*, 162(3), F298–F309. doi: 10.1149/2.0691503jes
- [95] Kumar, B., Chen, C., Varanasi, C., & Fellner, J. P. (2005). Electrical properties of heterogeneously doped yttria stabilized zirconia. *Journal of Power Sources*, 140(1), 12–20. doi: 10.1016/j.jpowsour.2004.08.016
- [96] Ahamer, C., Opitz, A. K., Rupp, G. M., & Fleig, J. (2017). Revisiting the Temperature Dependent Ionic Conductivity of Yttria Stabilized Zirconia (YSZ). *Journal of The Electrochemical Society*, 164(7). doi: 10.1149/2.0641707jes
- [97] Kwon, O., & Choi, G. (2006). Electrical conductivity of thick film YSZ. *Solid State Ionics*, 177(35-36), 3057–3062. doi: 10.1016/j.ssi.2006.07.039
- [98] Clark, D., Tong, J., Morrissey, A., Almansoori, A., Reimanis, I., & Ohayre, R. (2014). Anomalous low-temperature proton conductivity enhancement in a novel protonic nanocomposite. *Phys. Chem. Chem. Phys.*, 16(11), 5076–5080. doi: 10.1039/c4cp00468j
- [99] Zhang, Y., Xie, D., Chi, B., Pu, J., Li, J., & Yan, D. (2019). Basic properties of proton conductor BaZr_{0.1}Ce_{0.7}Y_{0.1}Yb_{0.1}O_{3-δ} (BZCYYb) material. *Asia-Pacific Journal of Chemical Engineering*, 14(4). doi: 10.1002/apj.2322
- [100] Norby, T., & Larring, Y. (1997). Concentration and transport of protons in oxides. *Current Opinion in Solid State and Materials Science*, 2(5), 593–599. doi: 10.1016/s1359-0286(97)80051-4
- [101] Zhu, H., Ricote, S., Duan, C., O'Hayre, R. P., & Kee, R. J. (2018). Defect Chemistry and Transport within Dense BaCe_{0.7}Zr_{0.1}Y_{0.1}Yb_{0.1}O_{3-δ} (BCZYYb) Proton-Conducting Membranes. *Journal of The Electrochemical Society*, 165(10). doi: 10.1149/2.1091810jes
- [102] Ren, R., Wang, Z., Xu, C., Sun, W., Qiao, J., Rooney, D. W., & Sun, K. (2019). Tuning the defects of the triple conducting oxide BaCo_{0.4}Fe_{0.4}Zr_{0.1}Y_{0.1}O_{3-δ} perovskite toward enhanced cathode activity of protonic ceramic fuel cells. *Journal of Materials Chemistry A*, 7(31), 18365–18372. doi: 10.1039/c9ta04335g

- [103] Ding, D. (2018). Quarterly Report on Node (FY2018_Q2): Advanced Electrode and Solid Electrolyte Materials for Elevated Temperature Water Electrolysis to Support UTRC HTE Project. doi: 10.2172/1478525
- [104] Choi, S., Kucharczyk, C. J., Liang, Y., Zhang, X., Takeuchi, I., Ji, H.-I., & Haile, S. M. (2018). Exceptional power density and stability at intermediate temperatures in protonic ceramic fuel cells. *Nature Energy*, 3(3), 202–210. doi: 10.1038/s41560-017-0085-9
- [105] Vahidmohammadi, A., & Cheng, Z. (2015). Fundamentals of Synthesis, Sintering Issues, and Chemical Stability of BaZr_{0.1}Ce_{0.7}Y_{0.1}Yb_{0.1}O_{3-δ} Proton Conducting Electrolyte for SOFCs. *Journal of The Electrochemical Society*, 162(8), F803–F811. doi: 10.1149/2.0021508jes
- [106] Katahira, K., Kohchi, Y., Shimura, T., & Iwahara, H. (2000). Protonic conduction in Zr-substituted BaCeO₃. *Solid State Ionics*, 138(1-2), 91–98. doi: 10.1016/s0167-2738(00)00777-3
- [107] Ricote, S., Bonanos, N., & Caboche, G. (2009). Water vapour solubility and conductivity study of the proton conductor BaCe_(0.9-x)Zr_xY_{0.1}O_(3-δ). *Solid State Ionics*, 180(14-16), 990–997. doi: 10.1016/j.ssi.2009.03.016
- [108] Somekawa, T., Matsuzaki, Y., Tachikawa, Y., Matsumoto, H., Taniguchi, S., & Sasaki, K. (2016). Physicochemical properties of proton-conductive Ba(Zr_{0.1}Ce_{0.7}Y_{0.1}Yb_{0.1})O_{3-δ} solid electrolyte in terms of electrochemical performance of solid oxide fuel cells. *International Journal of Hydrogen Energy*, 41(39), 17539–17547. doi: 10.1016/j.ijhydene.2016.07.265
- [109] Grolig, J. G., Froitzheim, J., & Svensson, J.-E. (2015). Coated stainless steel 441 as interconnect material for solid oxide fuel cells: Evolution of electrical properties. *Journal of Power Sources*, 284, 321–327. doi: 10.1016/j.jpowsour.2015.03.029

APPENDIX

SUPPLEMENTAL INFORMATION

A.1 RStudio Circle Tracing Program

```
# EISData_root_finder.R: This file parses Gamry EIS data files from a given directory
(input_dir)
#           to find the intercepts of various arcs on the EIS curve.
#           Plots with the computed arcs overlayed onto the EIS curve are output as png
files.
#           A csv file containing arc intercept information is generated.
#
# Author: Marcos Hernandez-Rodriguez
# Updated: 18 November 2019

#documentation on the circular package is available at https://cran.r-
project.org/web/packages/circular/circular.pdf
require(circular)

#set directories, relative to working directory of code
input_dir <- "/Data"
output_plots_dir <- "/Graphs/"
dir.create(paste(getwd(), output_plots_dir, sep=""), showWarnings = FALSE)
output_csv_dir <- paste(getwd(), "/Results/", sep="")
dir.create(output_csv_dir, showWarnings = FALSE)

#path to Gamry EIS .DTA files, relative to working directory of code
dir_address <- paste(getwd(),input_dir, sep="")
file_list <- list.files(dir_address)

#variables
curve_intercepts <- c("Type", "File Name", "Date", "Time", "Root 1 (DC)", "Root2",
"Difference_1", "h_1", "k_1", "radius_1",
                    "Type", "File Name", "Root 3", "Root 4(Polarization)", "Difference_2", "h_2",
"k_2", "radius_2",
                    "Type", "File Name", "Root 5", "Root 6", "Difference_3", "h_3", "k_3",
"radius_3")

#define subset of data rows from raw_data to be used in target_data
start_target_data <- 150
end_target_data <- 360
```

```

#indexes to subset target_data to calculate first arc
start_first_arc<- 9
end_first_arc<- 36

#indexes to subset target_data to calculate second arc
start_second_arc <- 56
end_second_arc <- 71

#indexes to subset target_data to calculate third arc
start_third_arc <- 1
end_third_arc <- 71

read_data <- function (start_target_data, end_target_data, raw_data) {
  #clear variables before processing new data file
  target_data <- NULL

  for(j in seq(from=start_target_data, to=end_target_data, by=3)){
    #extract impedance data from raw data
    z_real <- as.numeric(raw_data[j,"V1"])
    z_imag <- abs(as.numeric(raw_data[j,"V2"]))
    target_data <- rbind(target_data, data.frame(z_real,z_imag))
  }
  return(target_data)
}

for(i in seq(1:length(file_list))){
  file_name = paste("Data/", file_list[i], sep="" )
  raw_data <- read.delim(file = file_name, sep = "\t", header=FALSE, stringsAsFactors=FALSE,
encoding = "UTF-8")

  target_data <- read_data(start_target_data, end_target_data, raw_data)

  #get time and date of EIS test
  time <- raw_data[5,"V3"]
  date <- raw_data[4,"V3"]

  #remove outlying points
  target_data <- target_data[-c(83,85),]

  #use lsfit method of package CIRCULAR to fit circles to the dataset
  first_arc <- lsfit.circle(target_data[1:start_first_arc,1], target_data[1:start_first_arc,2], units =
"radians",
  template = "geographics",
  modulo = "pi", zero = 0,
  rotation = "clock")

```

```

second_arc <-lsfit.circle(target_data[end_first_arc:start_second_arc,1],
target_data[end_first_arc:start_second_arc,2], units = "radians",
      template = "geographics",
      modulo = "pi", zero = 0,
      rotation = "clock")
#arc needed to correctly plot data points
third_arc <-lsfit.circle(target_data[start_third_arc:end_third_arc,1],
target_data[start_third_arc:end_third_arc,2], units = "radians",
      template = "geographics",
      modulo = "pi", zero = 0,
      rotation = "clock")

#save plot with arcs to file in Graphs dir
pic_name = paste(getwd(), output_plots_dir, file_list[i], "_plot.png", sep="" )
png(file = pic_name, width = 860, height = 600, units = "px", bg = "white")

#statistics for first_arc
radius <- first_arc$coefficients[1]
h <- first_arc$coefficients[2]
k <- first_arc$coefficients[3]
root2 <- sqrt((radius^2)-(k^2)) + h
root1 <- h - sqrt((radius^2)-(k^2))
diff <- abs(root2 - root1)
first_arc_entry <- c("First_curve_intercepts", file_name, date, time, root1, root2, diff, h, k,
radius)

#statistics for second_arc
radius <- second_arc$coefficients[1]
h <- second_arc$coefficients[2]
k <- second_arc$coefficients[3]
root4 <- sqrt((radius^2)-(k^2)) + h
root3 <- h - sqrt((radius^2)-(k^2))
diff <- abs(root4-root3)
second_arc_entry <- c("Second_curve_intercepts", file_name, root3, root4, diff, h, k, radius)

#statistics for third_arc
radius <- cir3$coefficients[1]
h <- cir3$coefficients[2]
k <- cir3$coefficients[3]
root6 <- sqrt((radius^2)-(k^2)) + h
root5 <- h - sqrt((radius^2)-(k^2))
diff <- abs(root6-root5)
third_arc_entry <- c("Third_curve_intercepts", file_name, root5, root6, diff, h, k, radius)

#set bounds for x-axis

```

```

if(is.nan(root1) || is.nan(root2) || is.nan(root3) || is.nan(root4)){
  xbound<-as.integer(round(target_data[1,1] - 1))
  xhbound<-as.integer(round(target_data[nrow(target_data),1] + 1))
} else {
  xbound<-as.integer(round(root1)-1)
  xhbound<-as.integer(round(root6)+1)
}

#set bounds for y axis
range<-as.integer((0.50*(8 + xhbound - xbound)) / 1)

#plot circles
plot(first_arc, xaxt="n", yaxt="n", xlim=c(xbound, xhbound), ylim=c(-range, range))
par(new=TRUE)
plot(second_arc, xaxt="n", yaxt="n", xlim=c(xbound, xhbound), ylim=c(-range, range))
par(new=TRUE)
plot(third_arc, xaxt="n", yaxt="n", xlim=c(xbound, xhbound), ylim=c(-range, range))

axis(1, at=seq(xbound, xhbound , length=11), pos=0)
if(xbound == 0) axis(2, at=seq(-range,range, length=6), pos=0)
else axis(2, at=seq(-range,range, length=6))

#write circle roots and statistics to file
curve_intercepts <- rbind(curve_intercepts, c(first_arc_entry, second_arc_entry,
third_arc_entry))

dev.off()
}

write.csv(curve_intercepts, paste(output_csv_dir, "curve_intercepts.csv", sep=""))

```

A.2 CAD Drawings of Degradation Test Stand Ceramic Coupon Assembly

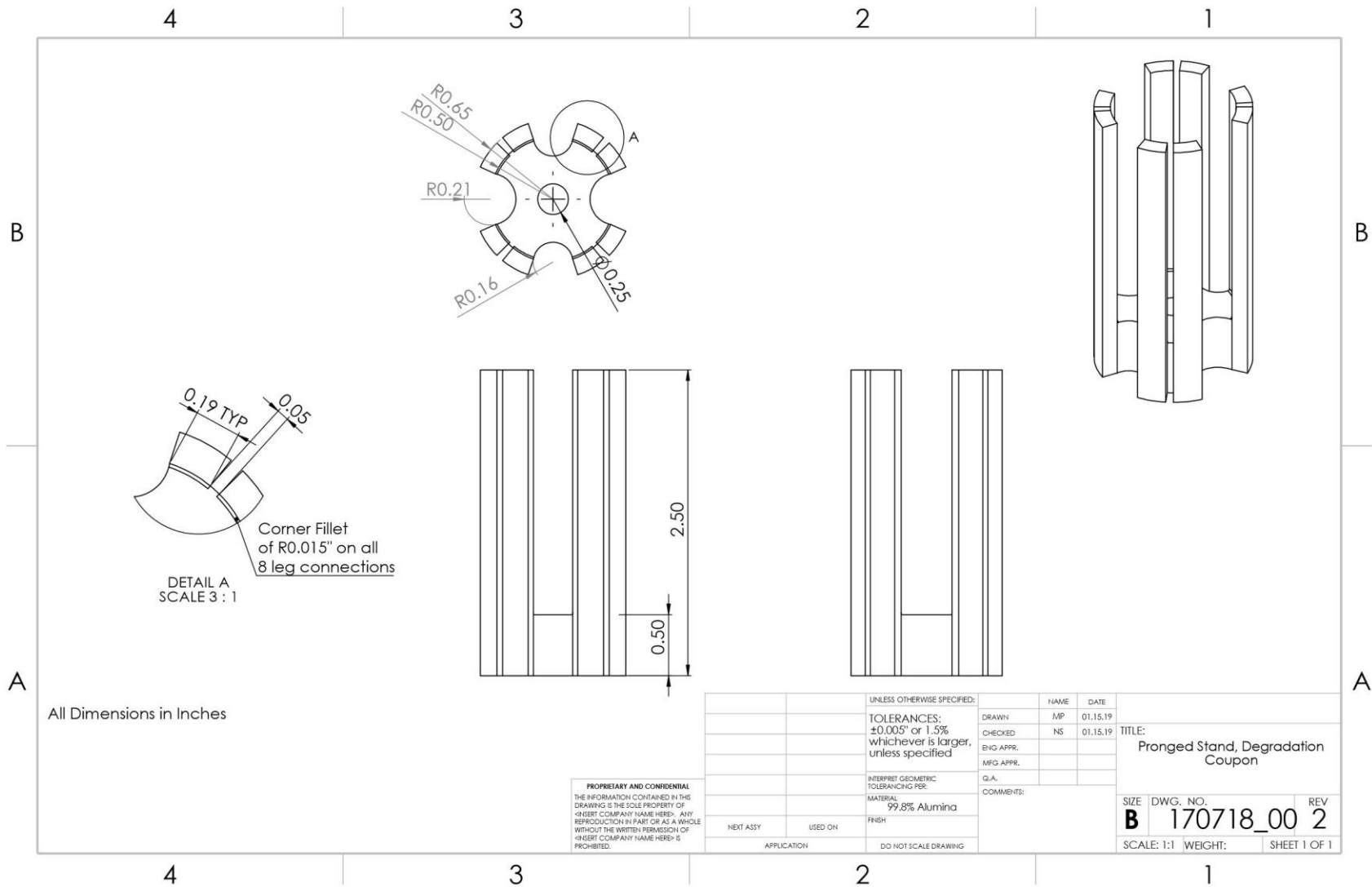


Figure A.1: CAD drawing of DTS support component

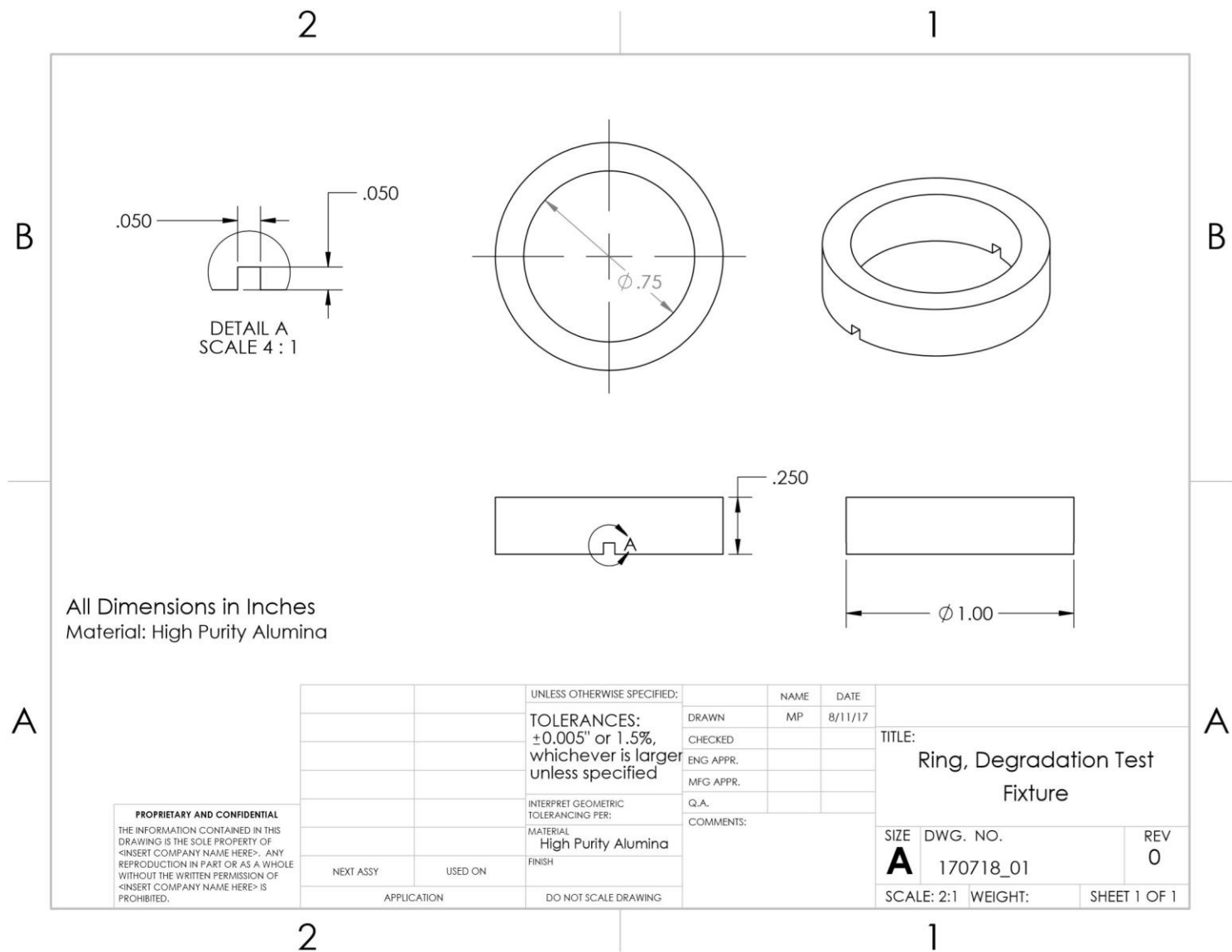


Figure A.2: CAD drawing of DTS isolation ring component

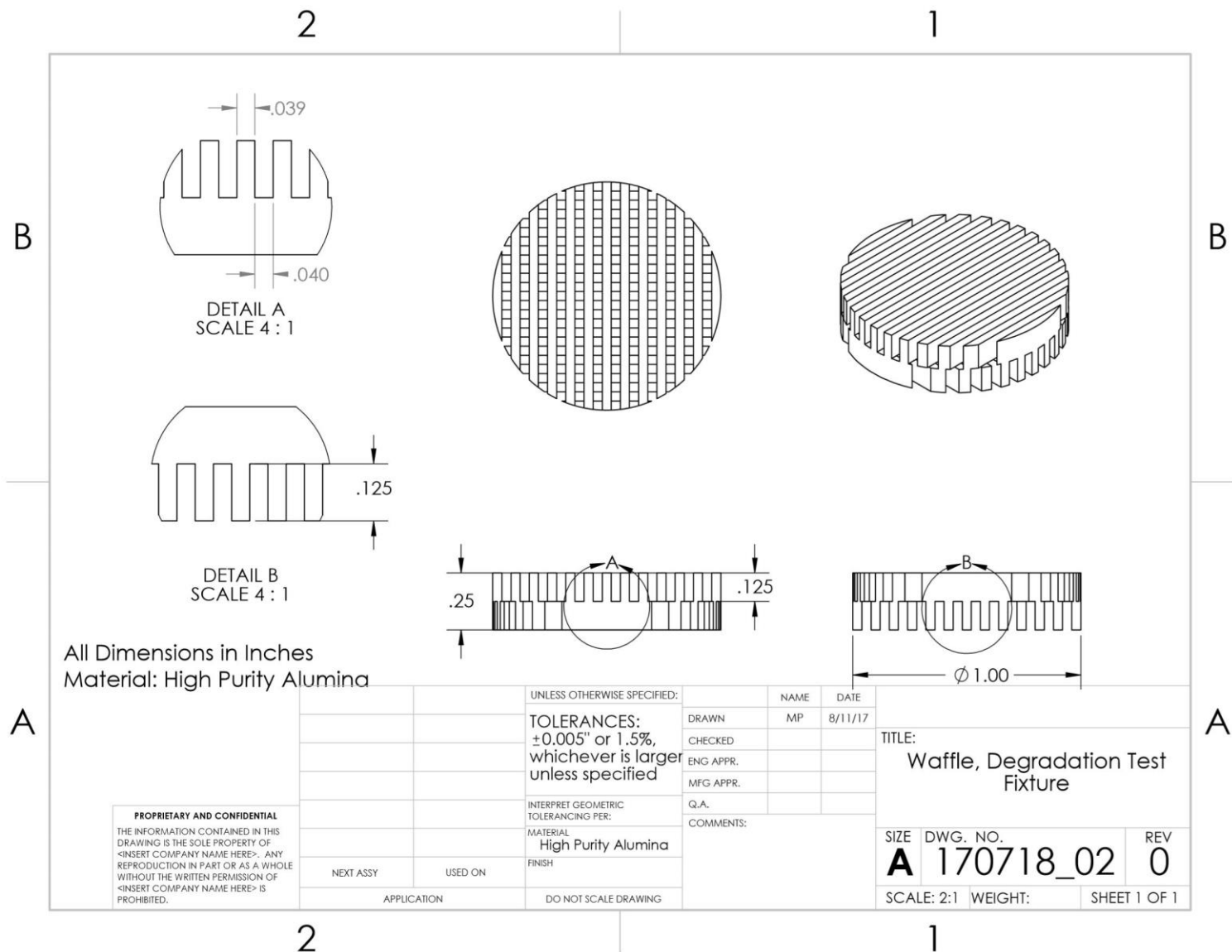


Figure A.3: CAD drawing of DTS waffle component

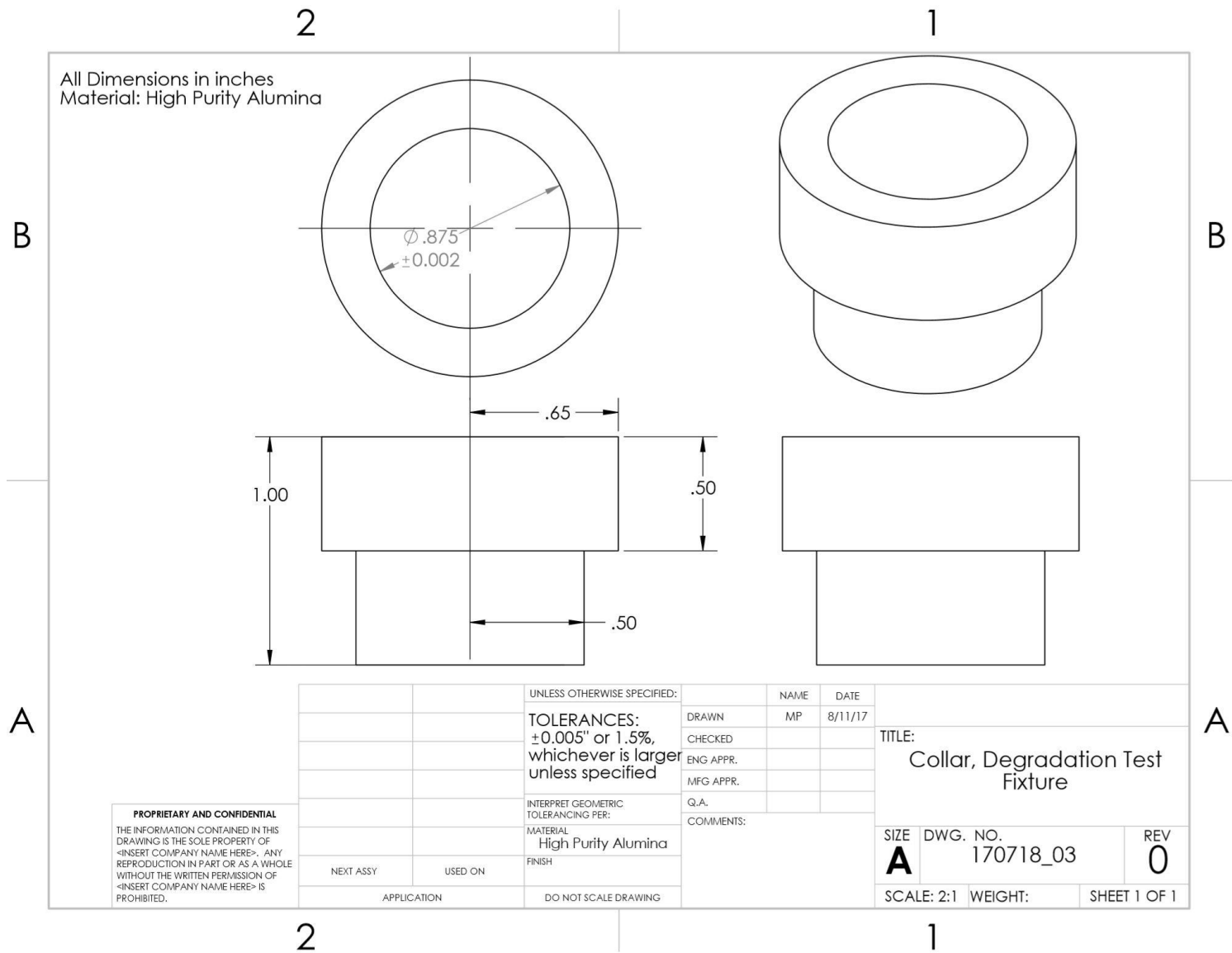


Figure A.4: CAD drawing of DTS collar component

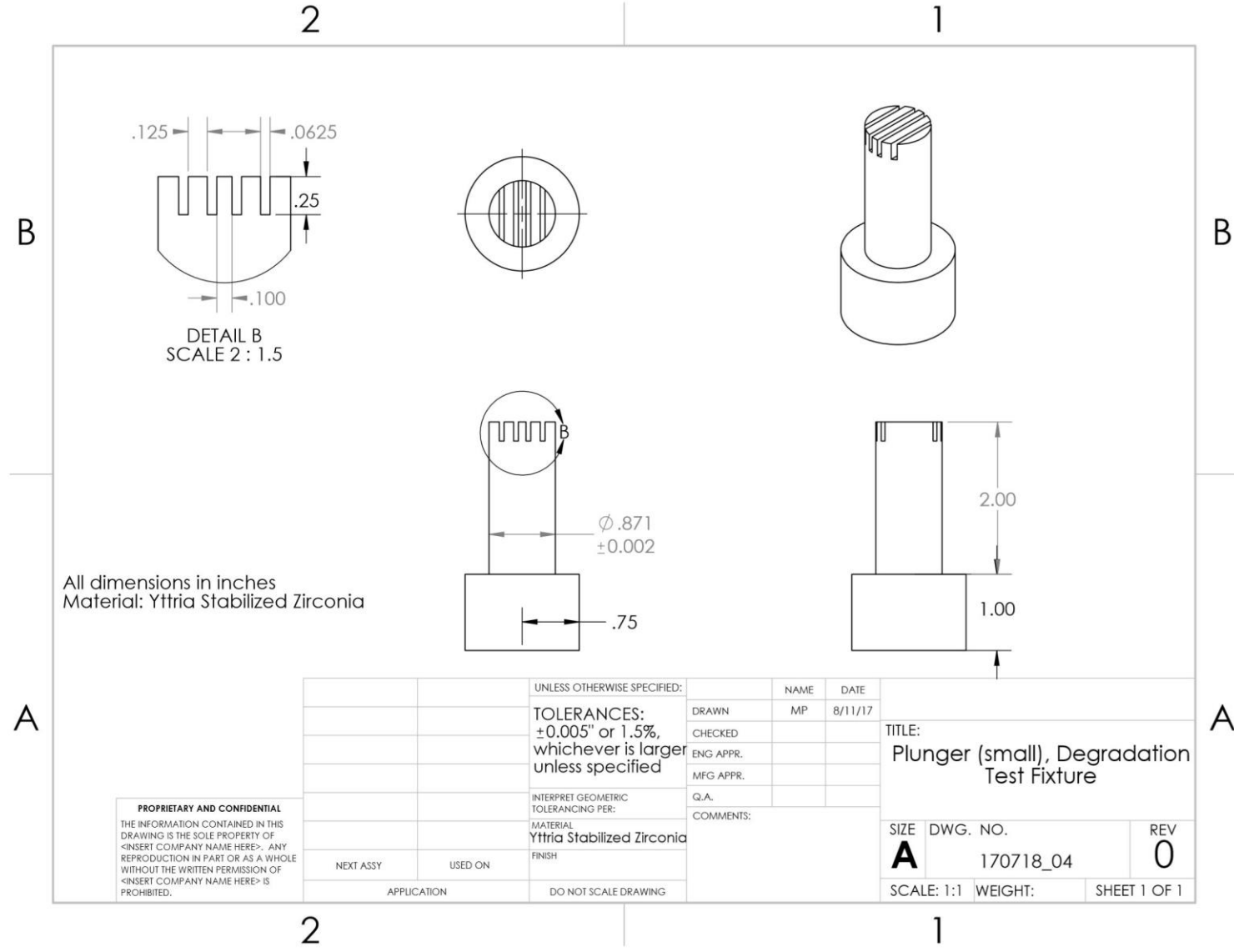


Figure A.5: CAD drawing of DTS small plunger component

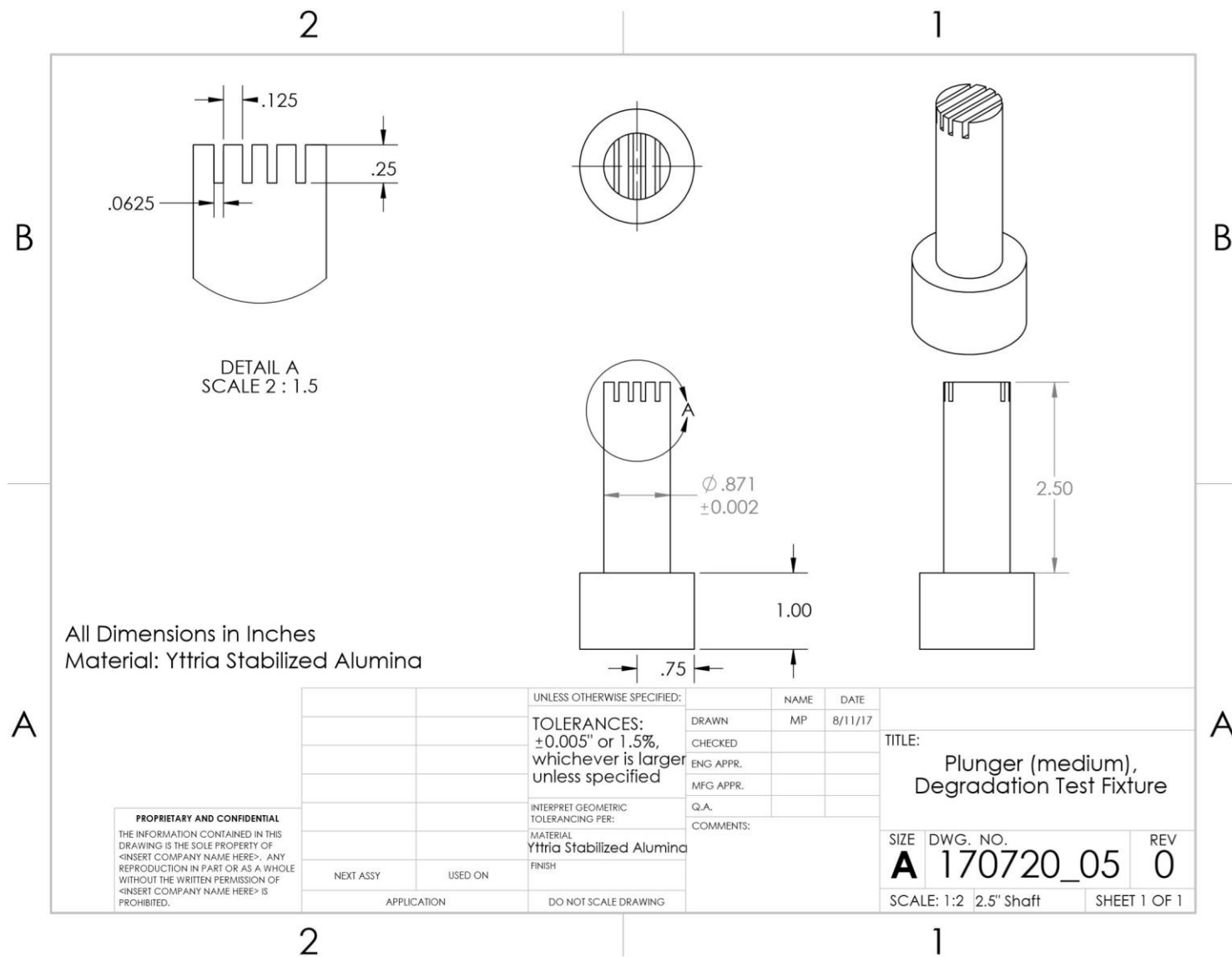


Figure A.6: CAD drawing of DTS medium plunger component

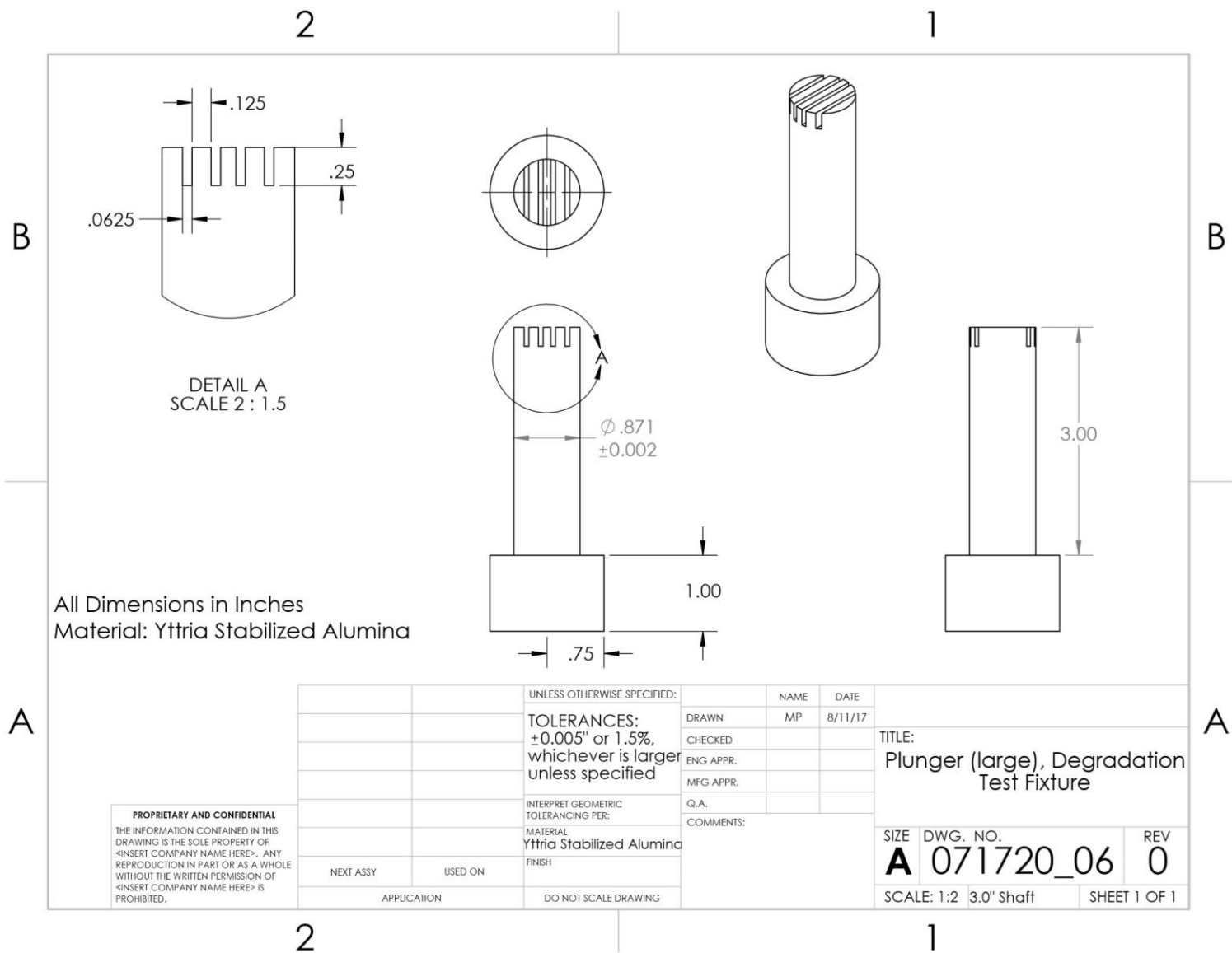


Figure A.7: CAD drawing of DTS large plunger component